Femtosecond vibrational dynamics in hydrogen-bonded systems

Femtosecond vibrational dynamics in hydrogen-bonded systems

Academisch Proefschrift

ter verkrijging van de graad van doctor aan de Universiteit van Amsterdam
op gezag van de Rector Magnificus prof. dr. J. J. M. Franse
ten overstaan van een door het college voor promoties ingestelde commissie
in het openbaar te verdedigen in de Aula der Universiteit
op dinsdag 1 juni 1999, te 9:30 uur

door

Sander Woutersen

geboren te Den Haag

Promotiecommissie

promotor:	prof. dr. A. Lagendijk
co-promotor:	dr. H. J. Bakker
overige leden:	prof. dr. J. I. Dijkhuis
	prof. dr. D. Frenkel
	prof. dr. A. W. Kleyn
	prof. dr. C. A. de Lange
	prof. dr. S. Völker

Faculteit der Wiskunde, Informatica, Natuurkunde en Sterrenkunde

The work described in this thesis was performed at the FOM-Institute for Atomic and Molecular Physics, Kruislaan 407, 1098 SJ Amsterdam, The Netherlands. It is part of the research program of the *Stichting voor Fundamenteel onderzoek der Materie* (FOM, Foundation for Fundamental Research on Matter) and was made possible by financial support from the *Nederlandse Organisatie voor Wetenschappelijk Onderzoek* (NWO, Dutch Organisation for Scientific Research).

ISBN 90-9012749-6

Cover: Measurements of the OH-stretch absorption band of hydrogen-bonded ethanol at three different temperatures, published in 1936 by J. Errera and P. Mollet (see Ref. [1]).

Contents

This thesis is based on the following papers:

S. Woutersen, M. Bonn, M. J. P. Brugmans, U. Emmerichs, and H. J. Bakker, "Generation of incoherent mid-infrared photon echoes," Opt. Lett. **21,** 1579–1581 (1996).

U. Emmerichs, S. Woutersen, and H. J. Bakker, "Generation of intense femtosecond optical pulses around 3 μm with kHz rep-rate," J. Opt. Soc. Am. B **14,** 1480–1483 (1997).

S. Woutersen, U. Emmerichs, and H. J. Bakker, "A femtosecond mid-infrared pump-probe study of hydrogen-bonding in ethanol," J. Chem. Phys. **107,** 1483–1490 (1997).

S. Woutersen, U. Emmerichs, and H. J. Bakker, "Femtosecond mid-infrared pump-probe spectroscopy of liquid water: evidence for a two-component structure," Science **278,** 658–660 (1997).

S. Woutersen, U. Emmerichs, H.-K. Nienhuys, and H. J. Bakker, "Anomalous temperature dependence of vibrational lifetimes in water and ice," Phys. Rev. Lett. **81,** 1106–1109 (1998).

S. Woutersen, U. Emmerichs, and H. J. Bakker, "Femtosecond mid-infrared pump-probe spectroscopy of water and ice," In *Ultrafast Phenomena XI*, T. Elsaesser, J. G. Fujimoto, D. A. Wiersma, and W. Zinth, eds., pp. 562–564 (Springer, Berlin, 1998).

S. Woutersen, U. Emmerichs, and H. J. Bakker, "Femtosecond mid-infrared spectroscopy of hydrogen-bonded liquids," Laser Chem. **19,** 83–90 (1999).

S. Woutersen, M. Bonn, U. Emmerichs, and H. J. Bakker, "Incoherent mid-infrared photon echoes with parametrically downconverted light," Laser Chem. **19,** 123–126 (1999).

S. Woutersen and H. J. Bakker, "The hydrogen bond in liquid water as a Brownian oscillator," submitted.

S. Woutersen and H. J. Bakker, "Vibrational Förster transfer in liquid water," in preparation.

Other publications:

S. Woutersen, J. B. Milan, W. J. Buma, and C. A. de Lange, "Resonance-enhanced multiphoton-ionization photo-electron spectroscopy of even-parity Rydberg states of atomic sulphur," Phys. Rev. A **54,** 5126–5132 (1996).

S. Woutersen, J. B. Milan, W. J. Buma, and C. A. de Lange, "Resonance-enhanced multiphoton-ionization photo-electron spectroscopy of even-parity autoionizing Rydberg states of atomic sulphur," J. Chem. Phys. **106,** 6831–6838 (1997).

M. Bonn, S. Woutersen, and H. J. Bakker, "Coherent picosecond vibron polaritons as probes of vibrational lifetimes," Opt. Commun. **147,** 138–142 (1998).

H.-K. Nienhuys, S. Woutersen, R. A. van Santen, and H. J. Bakker, "Mechanism for vibrational relaxation in water investigated by femtosecond infrared spectroscopy," accepted for publication in J. Chem. Phys.

1 Introduction

1.1 The hydrogen bond

The history of the hydrogen bond commences in 1920, when Latimer and Rodebush, who were at that time studying the structure and properties of water with G. N. Lewis, remarked that

> A free pair of electrons on one water molecule might be able to exert sufficient force on a hydrogen held by a pair of electrons on another water molecule to bind the two molecules together. Structurally this may be represented as
>
> 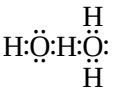
>
> Such combinations need not be limited to the formation of double or triple molecules. Indeed the liquid may be made up of large aggregates of molecules, continually breaking up and reforming under the influence of thermal agitation [2].

The authors used the hypothesis of the hydrogen bond to explain the high proton conductivity and dielectric constant of liquid water. Simultaneously with the development of the quantum-mechanical theory of chemical bonding in the years thereafter, an increasing amount of research was devoted to the nature of the hydrogen bond. An entire chapter of Linus Pauling's *The Nature of the Chemical Bond*, which appeared in 1939, was devoted to it. In the introduction of this chapter, Pauling wrote

> I believe that [...] it will be found that the significance of the hydrogen bond for physiology is greater than any other single structural feature [3].

This prediction came true when it was found that the double-helix structure of DNA and the secondary structure of proteins are both determined by hydrogen bonding. Since then, an ever increasing number of studies has been concerned with the structural and dynamical properties of the hydrogen bond.

Hydrogen bonding plays an important role in determining the physical and chemical properties of many substances. The most obvious example is water, which in the absence of hydrogen bonding would be a gas at room temperature. The abnormally high viscosity, surface tension, and heat of vaporization of water are also caused by hydrogen bonding. The effect of hydrogen bonds on crystal structure is best illustrated in ice I*h*, which has a very open structure that optimizes the hydrogen-bond interaction between the water molecules.

The hydrogen bond is an attractive interaction between a proton donor X−H and a proton acceptor Y, in the same or a different molecule: $X-H\cdots Y$, where X and Y are

electronegative atoms such as oxygen, nitrogen or fluorine. The hydrogen bond has covalent character, as has been confirmed recently by means of inelastic X-ray diffraction experiments [4]. This covalent character accounts for the cooperative nature of the hydrogen bond: formation of a hydrogen bond X−H···Y increases both the polarity of the X−H bond and the basicity of Y, which can result in a significant increase in strength of additional hydrogen bonds [5]. Hydrogen bonds are directional [6], and have bond energies in the range from 3 to 30 kJ/mol. This means that they are much weaker than ordinary covalent bonds, which typically have bond energies on the order of 500 kJ/mol. Because of this small bond energy and the small activation energy involved in its formation and rupture, hydrogen bonds are especially important in chemical and physical processes taking place at room temperature.

1.2 The XH-stretch mode as a probe of hydrogen-bond structure and dynamics

Formation of the hydrogen bond X−H···Y causes a redshift of the fundamental frequency of the XH-stretch (ν_{XH}) vibration. This redshift increases approximately linearly with decreasing hydrogen-bond distance $R_{\mathrm{X-H\cdots Y}}$. The relation between hydrogen-bond distance and ν_{XH} frequency was unambiguously demonstrated when the $R_{\mathrm{X-H\cdots Y}}$ distances of a large number of hydrogen-bonded substances (determined by X-ray diffraction) were compared with their ν_{XH} frequencies [7]. For moderately strong O−H···O hydrogen bonds, such as occur in water and ethanol, the redshift of ν_{OH} is typically 200–300 cm^{-1}. Simultaneously with the redshift of the XH-stretch frequency, an increase of both the linewidth and the absorption cross section of the $v_{\mathrm{XH}} = 0 \rightarrow 1$ transition occurs. The strong correlation of the hydrogen-bond strength and the ν_{XH} frequency has made infrared spectroscopy by far the most important tool to study hydrogen bonding.

Both the redshift and the increase of the linewidth of the ν_{XH} transition are due to anharmonic coupling between the $\nu_{\mathrm{XH\cdots Y}}$ hydrogen-bond mode and the ν_{XH} mode. The Hamiltonian of the system consisting of the coupled $\nu_{\mathrm{XH\cdots Y}}$ and ν_{XH} oscillators is very often assumed to have the form [8–12]

$$H = p^2/2m + m\omega^2 q^2/2 + P^2/2M + M\Omega^2 Q^2/2 + Kq^2 Q, \tag{1.1}$$

where q, p, m, ω and Q, P, M, Ω refer to the normal coordinate, conjugate momentum, reduced mass, and frequency of the ν_{XH} and $\nu_{\mathrm{XH\cdots Y}}$ mode, respectively, and K is an anharmonic coupling constant. This Hamiltonian can also be written as [12]

$$H = p^2/2m + m\omega_{\mathrm{eff}}^2(Q) q^2/2 + P^2/2M + M\Omega^2 Q^2/2 \tag{1.2}$$

where $\omega_{\mathrm{eff}}(Q)$ is the effective ν_{XH} frequency, given by

$$\omega_{\mathrm{eff}}(Q) = \omega\sqrt{1 + 2KQ/m\omega^2} \approx \omega + \text{const.} \times Q. \tag{1.3}$$

Therefore, the Hamiltonian (1.1) reproduces the approximately linear relationship between the redshift of the ν_{XH} frequency and the hydrogen-bond distance $R_{\mathrm{X-H\cdots Y}}$. Since the frequency Ω of the $\nu_{\mathrm{XH\cdots Y}}$ mode is much smaller than the frequency ω of the ν_{XH} mode, we

can use an adiabatic approximation, and calculate potential energy functions for the slow $\nu_{XH\cdots Y}$ mode in the $v_{XH} = 0$ and $v_{XH} = 1$ states. The minima of the (harmonic) potential energy functions for the hydrogen-bond mode obtained in this way are displaced with respect to each other (see Fig. 1.1). In a fully quantum-mechanical model, the adiabatic potentials can be used to calculate the hydrogen-bond wave functions $\psi(Q)$ in the $v_{XH} = 0$ and $v_{XH} = 1$ potentials. The probability of a transition between $v_{XH} = 0$ and $v_{XH} = 1$

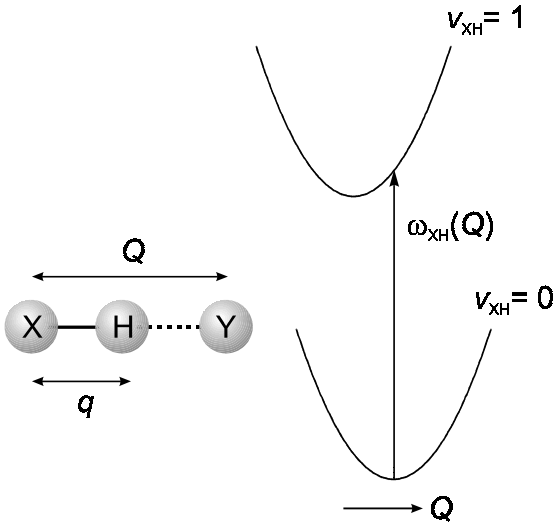

FIGURE 1.1. Adiabatic potential energy functions for the hydrogen bond, calculated using the Hamiltonian (1.1).

states depends on the overlap of the hydrogen-bond wave functions in the $v_{XH} = 0$ and $v_{XH} = 1$ potentials (Franck-Condon factor). The displacement of the $v_{XH} = 0$ and $v_{XH} = 1$ potentials with respect to each other gives rise to $v_{XH} = 0 \rightarrow 1$ transitions in which the $v_{XH\cdots Y}$ quantum number changes. In the ν_{XH} spectrum, these transitions appear as sum and difference frequency bands at $\nu_{XH} \pm n\nu_{XH\cdots Y}$ (Franck-Condon progression). From the overlap of the hydrogen-bond wave functions in the $v_{XH} = 0$ and $v_{XH} = 1$ potentials the relative intensities in the Frank-Condon progression can be calculated [10]. Maréchal and Witkowski were the first to do this, and found good agreement between calculated and experimental OH-stretch absorption bands of several hydrogen-bonded complexes in the gas phase [8, 10].

In the condensed phase, the hydrogen-bond mode strongly interacts with other low-frequency degrees of freedom ('bath modes'). This leads to the well-known broad and smooth ν_{XH} spectra of hydrogen-bonded molecules in liquids and solids. The theory outlined above, which applies to isolated hydrogen-bonded complexes, must then be refined to include the interaction of the $\nu_{XH\cdots Y}$ oscillator with the bath. This approach to the study of ν_{XH} bands of hydrogen-bonded systems in the condensed phase has been developed mainly by Robertson and Yarwood [9, 11]. The Hamiltonian (1.1) is still used, but the $\nu_{XH\cdots Y}$ mode is modeled as a classical harmonic oscillator driven by a random force which represents the interaction with the bath modes. As a consequence, the $\nu_{XH\cdots Y}$ coordinate $Q(t)$ obeys a Langevin equation, and the Hamiltonian (1.1) governing the ν_{XH} motion becomes a stochastic operator. The ν_{XH} frequency is determined by the time dependence of

$Q(t)$ via Eq. (1.3). Essentially, this means that the fluctuations of the ν_{XH} frequency of a hydrogen-bonded molecule directly mirror the dynamics of the hydrogen-bond motion.

The relationship between $Q(t)$ and the ν_{XH} frequency motivates the use of infrared spectroscopy on the XH-stretch mode to study hydrogen-bond dynamics in the condensed phase. Until recently, such infrared studies have only been done with linear spectroscopy [13, 14]. Unfortunately, the broad ν_{XH} bands that typically occur in the linear absorption spectra of hydrogen-bonded systems in the condensed phase only reflect the distribution of ν_{XH} frequencies (hydrogen-bond lengths), and provide no information concerning the dynamics of the hydrogen bond. Such information can be obtained by means of nonlinear spectroscopy on the ν_{XH} mode, which makes it possible to study the dynamics of a subensemble of the molecules with a specific ν_{XH} frequency. With the advent of laser setups that produce ultrashort pulses with high intensities in the mid-infrared wavelength region, nonlinear spectroscopy on molecular vibrations became possible, and a large number of nonlinear optical studies on hydrogen-bonded vibrations has since been reported, most of which involved pump-probe experiments. In these experiments, a subensemble of the hydrogen-bonded molecules with a certain ν_{XH} frequency is selectively excited by an intense resonant pump pulse, and its evolution is studied by a delayed probing pulse (see the next Section). Initially, mid-infrared pulses with durations in the picosecond range were used to perform vibrational pump-probe experiments. In this way, the ν_{XH} modes of several hydrogen-bonded systems were investigated, in particular the ν_{OH}, ν_{NH}, and ν_{CH} modes of hydrogen-bonded complexes dissolved in CCl_4 [15–21], the ν_{OH} mode of dilute HDO:D_2O solutions [22, 23] and of a hydrogen-bonded polymer [24, 25], and the ν_{OH} mode of hydrogen-bonded surface hydroxyls [26, 27]. In the past few years, the development of amplified Titanium:sapphire laser systems has made it possible to generate intense mid-infrared pulses in the femtosecond range [28, 29]. Femtosecond vibrational studies on hydrogen-bonded systems reported to date include spectrally resolved pump-probe experiments on the ν_{OH} mode of HDO:D_2O [30, 31], visible-pump/infrared-probe experiments on the $\nu_{C=O}$ mode of hydrogen-bonded complexes in solution [32], and the experiments reported in this thesis.

1.3 Vibrational pump-probe spectroscopy

1.3.1 General considerations

In a vibrational pump-probe experiment, an intense pump pulse prepares a nonstationary state in which a fraction of the molecules is in an excited state of a molecular vibration, usually the first excited ($v = 1$) state. This nonstationary state is interrogated after a delay time τ by a probing pulse. The population of the $v = 1$ state of the molecular vibration by the pump pulse gives rise to decreased absorption at the $v = 0 \rightarrow 1$ frequency and stimulated emission at the $v = 1 \rightarrow 0$ frequency (bleaching), and to an increased absorption at the $v = 1 \rightarrow 2$ frequency (excited-state absorption). The OH-stretch vibrations studied in this thesis are anharmonic, and the $v = 0 \rightarrow 1$ and $v = 1 \rightarrow 2$ frequencies separated by proximately 250 cm^{-1}. Hence, whether the bleaching or the excited-state absorption is observed depends on the probe frequency. In general, two types of pump-probe experiments

are performed: (1) delay scans, in which the pump and probe have fixed frequencies, and the absorption change of the probe pulse is measured as a function of the relative delay between pump and probe; (2) transient spectra, in which the delay and pump frequency have a fixed value, and the absorption change of the probe pulse is monitored as a function of the frequency of the probe pulse.

1.3.2 Quantitative description of pump-probe spectroscopy

The pump-probe signal is defined as the difference between the transmission of the probe pulse with and without excitation of the sample by the pump pulse. We therefore want to calculate the difference between the time-integrated intensities of the probe pulse at the end of the sample with and without the presence of the pump pulse. The intensity in absence of the probe pulse is given by the Lambert-Beer law. To calculate the intensity in the presence of the pump pulse, we have to consider the propagation of the probe pulse in the nonlinearly polarized medium. The pump and probe fields have the form

$$E_j(\mathbf{r},t) = \tilde{E}_j(z,t)e^{i(k_j z-\omega_j t)} + \text{c.c.}, \tag{1.4}$$

with $j = 1$ for the pump and $j = 2$ for the probe field. In this equation, $\tilde{E}_j(z,t)$ are the pulse envelope functions, and ω_j the center frequencies of the pump and probe pulses. In the slowly varying envelope approximation, the wave equation for the probe reads [33]:

$$\left(\frac{\partial}{\partial z}+\frac{1}{v}\frac{\partial}{\partial t}\right)\tilde{E}_2(z,t) = -\frac{\alpha_0(\omega_2)}{2}\tilde{E}_2(z,t)+\frac{2\pi i\omega_2}{nc}\tilde{P}^{(3)}(z,t), \tag{1.5}$$

where $\tilde{P}^{(3)}(z,t)$ is the envelope function of the third-order polarization and $\alpha_0(\omega_2)$ is the linear absorption coefficient at the probe frequency. In this thesis, we will study broad OH-stretch absorption bands, and we can safely assume that $\alpha_0(\omega)$ is constant over the power spectra of the pump and probe pulses. If we work in a moving frame and use the retarded time coordinate $\eta = t - z/v$ this equation becomes [34]

$$\frac{\partial}{\partial z}\tilde{E}_2(z,\eta) = -\frac{\alpha_0(\omega_2)}{2}\tilde{E}_2(z,\eta)+\frac{2\pi i\omega_2}{nc}\tilde{P}^{(3)}(z,\eta). \tag{1.6}$$

The third-order polarization is a function of the pump and probe fields, which means that the evolution of the probe pulse is governed by a system of coupled equations for the probe field and the third-order polarization. When the third-order polarization has a relatively small effect on the probe intensity, we can use a perturbative approach: we calculate the third-order polarization using the unperturbed linear wave-equations

$$\frac{\partial}{\partial z}\tilde{E}_j^{(1)}(z,\eta) = -\frac{\alpha_0(\omega_j)}{2}\tilde{E}_j^{(1)}(z,\eta), \tag{1.7}$$

which have the solutions:

$$\tilde{E}_j^{(1)}(z,\eta) = \tilde{E}_j(0,\eta)e^{-\alpha_0(\omega_j)z/2}. \tag{1.8}$$

With an explicit expression for the third-order polarization in terms of $\tilde{E}_j^{(1)}(z,\eta)$ we can calculate the probe intensity in the presence of the pump pulse:

$$\tilde{E}_2(z,\eta) = \tilde{E}_2^{(1)}(z,\eta) + \frac{2\pi i\omega_2}{nc} e^{-\alpha_0(\omega_2)z/2} \int_0^z dz'\, \tilde{P}^{(3)}(z',\eta) e^{\alpha_0(\omega_2)z'/2}. \tag{1.9}$$

The pump-probe signal is defined as the difference between the time-integrated probe intensities at the end of the sample in the presence and absence of the pump pulse, and is given by

$$\begin{aligned} S &= \int_{-\infty}^{\infty} dt \left\{ |\tilde{E}_2(L,t)|^2 - |\tilde{E}_2^{(1)}(L,t)|^2 \right\} \\ &= \frac{4\pi\omega_2}{nc} \mathrm{Im} \int_{-\infty}^{\infty} d\eta\, \tilde{E}_2^{(1)*}(L,\eta) e^{-\alpha_0(\omega_2)L/2} \int_0^L dz \tilde{P}^{(3)}(z,\eta) e^{\alpha_0(\omega_2)z/2}, \end{aligned} \tag{1.10}$$

where L is the thickness of the sample. In this equation, we have neglected the higher-order term quadratic in the third-order polarization. Eq. (1.10) is a general expression for the transmission decrease of the probe in the presence of the pump pulse, and holds for arbitrary optical thickness $\alpha_0 L$ of the sample. For optically thin samples ($\alpha_0 L \ll 1$), $P^{(3)}$ and $E_2^{(1)}$ are independent of z, and Eq. (1.10) reduces to the well-known expression [33, 35]

$$S = \frac{4\pi\omega_2 L}{nc} \mathrm{Im} \int_{-\infty}^{\infty} dt\, \tilde{E}_2^{(1)*}(t) \tilde{P}^{(3)}(t). \tag{1.11}$$

In pump-probe experiments, only contributions to the third-order polarization which contain the pump field twice and the probe field once contribute to the signal. Hence, the third-order polarization at position z is an integration of the form [35]

$$\tilde{P}^{(3)}(z,\eta) = \int d\eta_1 \int d\eta_2 \int d\eta_3 \tilde{E}_1^{(1)*}(z,\eta_1) \tilde{E}_1^{(1)}(z,\eta_2) \tilde{E}_2^{(1)}(z,\eta_3) F(\eta,\eta_1,\eta_2,\eta_3), \tag{1.12}$$

where F is a function representing the nonlinear optical response of the medium. After substitution of Eq. (1.8) into this equation, the integration over z in Eq. (1.10) can be carried out, and we obtain

$$S = \frac{4\pi\omega_2}{nc} \frac{e^{-\alpha(\omega_2)L}(1-e^{-\alpha(\omega_1)L})}{\alpha(\omega_1)} \mathrm{Im} \int_{-\infty}^{\infty} dt\, \tilde{E}_2^{(1)*}(0,t) \tilde{P}^{(3)}(0,t), \tag{1.13}$$

which is identical to Eq. (1.11) apart from a proportionality constant. Thus, for broad absorption bands, the optical thickness of the sample has no influence on the delay dependence of the pump-probe signal. In the remainder of this thesis, Eq. (1.13) (without the prefactor) will be used to calculate vibrational pump-probe signals.

1.4 Outline of this thesis

This thesis is concerned with the dynamics of the OH-stretch (ν_{OH}) mode in strongly hydrogen-bonded systems, which will be studied by means of vibrational pump-probe

spectroscopy. First, a description of the experimental setup is given in Chapter 2. The study of hydrogen-bond dynamics begins in Chapter 3, with hydrogen-bonded ethanol clusters in solution. Since an ethanol molecule can only participate in two hydrogen bonds, these clusters are linear aggregates of hydrogen-bonded ethanol molecules, and constitute a relatively simple model system to investigate hydrogen-bond dynamics in the condensed phase.

Chapter 4 is the first of five chapters on the dynamics of the much more complicated system of liquid water. Since the dynamics of the ν_{OH} mode in liquid H_2O is complicated by the strong coupling between the OH-oscillators, previous studies have very often concentrated on the ν_{OH} mode of dilute solutions of HDO in D_2O, where the coupling between the ν_{OH} vibrations is negligible. In Chapters 4 to 7 we will extensively study the dynamics of the ν_{OH} mode in dilute HDO:D_2O. First, we will concentrate on the fast spectral relaxation that takes place in the first picosecond after excitation of the ν_{OH} mode (Chapter 4). Then the orientational relaxation of the O−H groups is discussed, which will be found to be intricately connected with the spectral relaxation (Chapter 5). After the first picosecond, the ν_{OH} dynamics are determined mainly by the population relaxation out of the $\nu_{OH} = 1$ state, which is discussed in Chapter 6. The interesting and dramatic effects that coherent coupling can have on the observations made using pump-probe spectroscopy are described quantitatively in Chapter 7. The results observed in a pump-probe study on the ν_{OH} mode of HDO:D_2O by Laenen *et al.* are explained in terms of these effects. This Chapter concludes the investigation of the ν_{OH} mode of the model system HDO:D_2O. In Chapter 8 we present the first pump-probe study on the ν_{OH} mode in liquid H_2O, that is, in 'real' water.

The last Chapter of this thesis is a photon-echo study of the ν_{OH} mode in a hydrogen-bonded system. Here, the emphasis will not be on the ν_{OH} dynamics, but rather on the use of mid-infrared incoherent photon echoes to study the homogeneous dephasing of a molecular vibration.

2 Experimental setup for time-resolved vibrational spectroscopy

2.1 Introduction

Nonlinear spectroscopy of vibrational transitions requires ultrashort pulses that are tunable in the mid-infrared region of the electromagnetic spectrum. The pulses have to be intense, since molecular vibrational transitions are hard to saturate due to their small absorption cross sections. Since the dynamics of vibrational transitions often takes place on subpicosecond time scales, the pulse lengths should preferably be in the femtosecond region.

Continuously tunable pulses in the mid-infrared can be generated by different lasers and techniques, such as free-electron lasers [36], color-center lasers, difference-frequency mixing [37, 38], and optical parametric generation and amplification. Parametric generation and amplification is a favorable choice because it can deliver short, widely tunable pulses of high intensity.

Optical parametric amplification (OPA) is a nonlinear interaction in which two light waves of frequencies ω_1 and ω_2 are amplified in a medium which is irradiated with an intense pump wave of frequency $\omega_3 = \omega_1 + \omega_2$. The higher of the two frequencies ω_1, ω_2 is referred to as the signal, the lower as the idler. For the parametric amplification to occur efficiently, the phase-matching condition $\mathbf{k}_3 = \mathbf{k}_1 + \mathbf{k}_2$ must be satisfied. This is generally achieved by using birefringent nonlinear crystals. By changing the angle of the optical axis of the crystal with respect to the polarization of one or two of the three interacting fields, a particular set of frequencies ω_1, ω_2 is selected for which both the conditions of phase matching ($n_3\omega_3 = n_1\omega_1 + n_2\omega_2$) and energy conservation ($\omega_3 = \omega_1 + \omega_2$) are fulfilled.

From a classical point of view, parametric amplification can occur only if the pump and at least one of the two other fields (signal or idler) is present at the entrance of the nonlinear medium. However, at sufficient pump energies, signal and idler are generated even if the initial numbers of photons at ω_1 and ω_2 is zero. This phenomenon is referred to as optical parametric superfluorescence [39] or optical parametric generation (OPG). It can only be understood from a quantum-mechanical point of view, and can be regarded as parametric amplification of the zero-point fluctuations of the electromagnetic field. The fact that parametric generation is essentially parametric amplification which starts from quantum noise will be exploited in Chapter 9.

The method of parametric generation and subsequent parametric amplification to generate picosecond idler pulses in the mid-infrared has been used extensively in the past. Initially, the parametric processes were carried out in $LiNbO_3$ crystals pumped with the fundamental output of a Nd:glass laser [40]. Later, Nd:YAG lasers became popular as

pump lasers because of their higher pulse energy and repetition rate, and for a number of years Nd:YAG-pumped mid-infrared OPG-OPA systems have been used as light sources in time-resolved investigations on the picosecond time scale [41, 42].

With the advent of amplified femtosecond Titanium-sapphire (Ti:sapphire) laser systems, parametric generation and amplification have been extended to the femtosecond time scale. The β-BaB_2O_4 (BBO) crystal is a good choice for parametric generation with femtosecond pulses, because it has a high damage threshold [43] and supports a large bandwidth. BBO crystals are therefore often used in commercial OPG-OPA systems. If these devices are pumped with the fundamental Ti:sapphire wavelength (∼800 nm), signal and idler cover a wavelength region of 1–2.6 μm. Longer wavelengths cannot be generated because of the onset of infrared absorption in BBO at approximately 2.6 μm [43]. The tuning range can be extended to 10 μm by difference-frequency mixing of the signal and idler in a different crystal, but the resulting intensities are rather low.

The generation of femtosecond pulses with sufficient energy in the 3 μm wavelength region requires a nonlinear crystal that is transparent in this region. A suitable candidate is $KTiOPO_4$ (KTP), which is transparent and phase-matchable up to a wavelength of 4.5 μm. Since it has a low damage threshold [43], it cannot be used for parametric generation. This suggests the use of BBO to generate a (weak) signal pulse at the appropriate wavelength, which can serve as a seed in subsequent parametric amplification in KTP to generate the required idler at ∼3 μm. The mid-infrared pulses used in the experiments presented in this thesis were generated in this way. With our setup, idler wavelengths up to 3.4 μm are easily obtained. Wavelengths longer than 3.4 μm are difficult to generate, since only very small amounts of the required signal seed can be generated due to the absorption of the corresponding idler in BBO.

Recently, an alternative method, consisting of continuum generation in glass combined with parametric amplification in BBO (pumped by the second harmonic of the Ti:sapphire laser) has been used to generate the seed. Subsequent parametric amplification in KTP (pumped by the fundamental of the Ti:sapphire) results in mid-infrared idler pulses that have energies of the same order of magnitude as those generated with our setup, and a somewhat better time-bandwidth product [29].

2.2 Laser system

The commercial Ti:sapphire system we use to pump the parametric down-conversion process is depicted in Fig. 2.1(a). A tunable mode-locked Titanium:sapphire oscillator (Spectra Physics Tsunami) is used to generate pulses of 65 fs FWHM at a repetition rate of 82 MHz, with a center wavelength of 800 nm. The oscillator is pumped with a Spectra Physics Beamlock 2060 continuous-wave Ar^+-laser running at an output power between 6 and 7 W. The oscillator output is used to seed a Quantronix 4800 regenerative Ti:sapphire amplifier, which is pumped with a Quantronix Series 100 intra-cavity frequency-doubled Q-switched Nd:YLF laser with an output of 9 mJ in ∼300 ns at a repetition rate of 1 kHz. The seed pulses are first stretched to a length of several hundreds of picoseconds using a single-grating stretcher-compressor. They are coupled into and out of the regenerative amplifier at a frequency of 1 kHz using a Pockel's cell. A photodiode monitoring the output

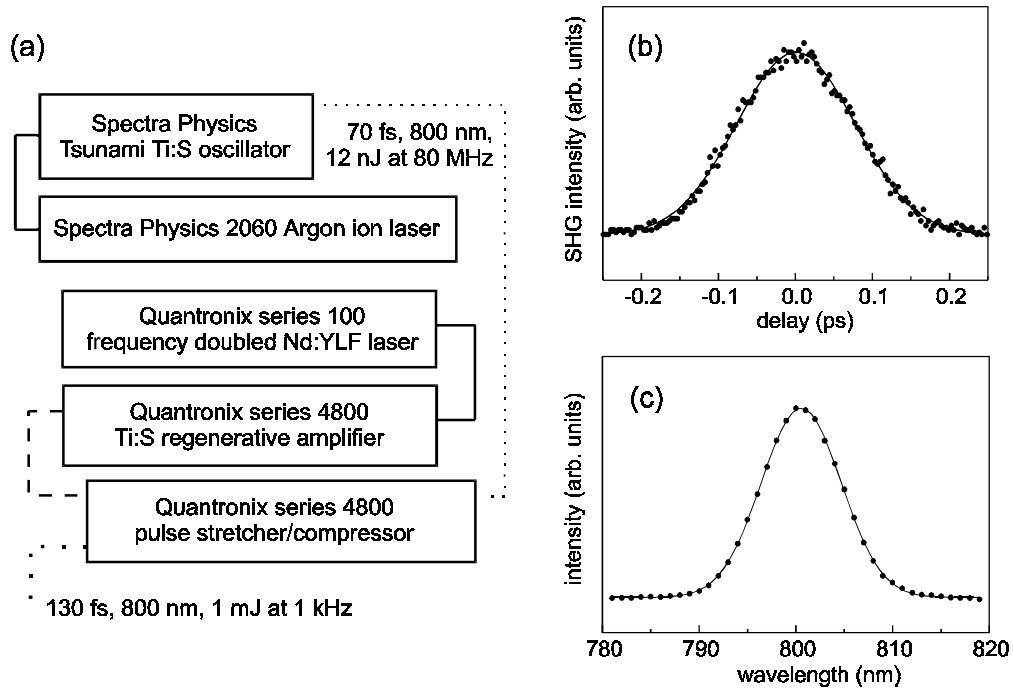

FIGURE 2.1. (a) The amplified Ti:sapphire laser system. (b) Autocorrelation trace of the compressed amplifier output, recorded in a 100 μm thick BBO crystal. The solid curve is a Gaussian with a FWHM of 181 fs. (c) Power spectrum of the pulses, recorded with a scanning monochromator. The solid curve is a Gaussian with a FWHM of 9.7 nm.

pulses of the Ti:sapphire oscillator is used together with a frequency divider to trigger the Pockel's cell and the Q-switch of the Nd:YLF laser, ensuring that they are synchronized with the seed pulses. After recompression of the regenerative amplifier output, transform-limited pulses of 1 mJ and 130 fs duration at a repetition rate of 1 kHz are obtained. A typical power spectrum and autocorrelation trace of the amplified pulses are shown in Fig. 2.1(b) and (c).

2.3 The optical parametric amplifier TOPAS

The commercial Traveling-wave Optical Parametric Amplifier of Superfluorescence "TOPAS" (Light Conversion) can generate signal and idler pulses that are continuously tunable from 1 to 2.6 μm. It is based on the two-stage parametric amplification of parametric superfluorescence. Both the generation and amplification take place in the same 5 mm β-Barium Borate (BBO) crystal (optical axis cut at 28°). The frequency of signal and idler is determined by the phase-matching angle of the crystal. BBO is a negative uniaxial crystal: the extraordinary refractive index n_e (for light polarized along the optical axis) is smaller than the ordinary refractive index n_o (for light polarized perpendicular to the optical axis). The polarization of the signal is perpendicular to the optical axis, whereas the pump and idler polarizations have a component along the optical axis, and hence experience a refractive index $n(\theta) = (\cos^2\theta/n_o^2 + \sin^2\theta/n_e^2)^{-1/2}$ determined by the angle θ between the optical axis and the polarization. The phase-matching condition is

therefore $n_3(\theta)\omega_3 = n_1(\theta)\omega_1 + n_2\omega_2$, which is referred to as type II phase matching [44]. Using the Sellmeier equations for the dispersion the refractive indices n_o and n_e [44], we can solve the phase-matching condition for θ to obtain the so-called tuning curve, which is shown in Fig. 2.2.

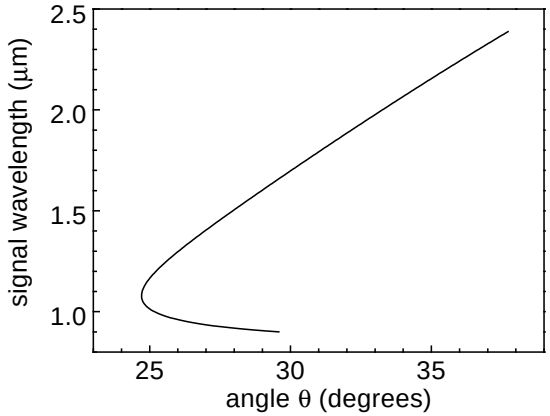

FIGURE 2.2. Calculated signal wavelength as a function of the angle θ for a pump wavelength of 800 nm. Note that θ is the angle between the optical axis and the polarization inside the crystal.

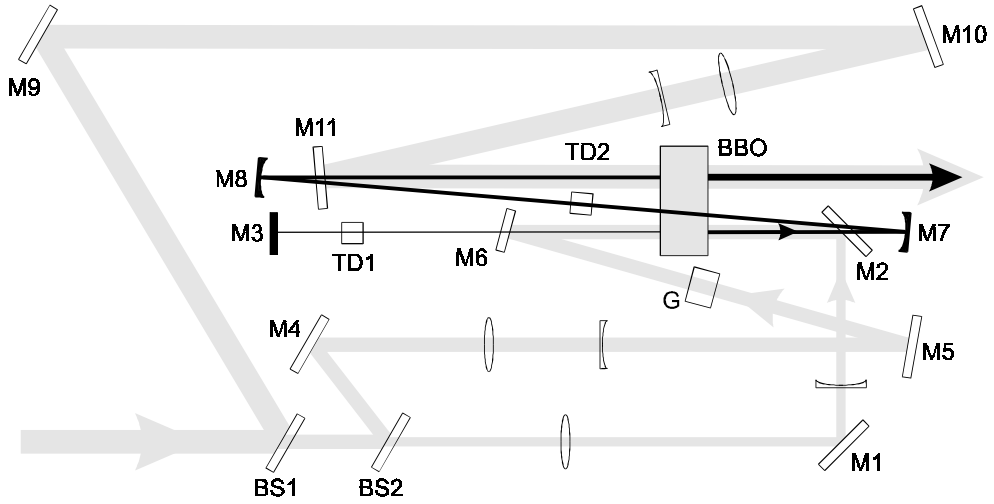

FIGURE 2.3. The traveling-wave optical parametric amplifier TOPAS. The 800 nm pump beam is shown in grey, the signal+idler beam in black. All mirrors are 800 nm high-reflective dielectric mirrors, except M3, M7 and M8 which are metallic mirrors. BBO: β-Barium Borate crystal; TD1 and TD2: birefringent plates to generate delay between signal and idler; G: glass plate; BS1 and BS2: beamsplitters.

The TOPAS is depicted schematically in Fig. 2.3. The 800 nm pump beam is split into three parts by the beamsplitters BS1 and BS2. The first part passes through a telescope and is directed to the BBO crystal by the mirrors M1 and M2. There, parametric generation takes place, resulting in a broadband seed pulse. The seed is reflected by M3 and the signal is parametrically amplified by the second part of the pump beam, which is directed to the BBO by mirrors M4–6. It passes through a glass plate G which compensates the

parallel displacement of the seed when the phase-matching angle of the BBO is changed. Since the amplification takes place in the far field of the seed, it provides a wavelength selection mechanism. The preamplified signal beam is slightly increased in diameter and again directed to the BBO crystal by mirrors M7 and M8. There it is strongly amplified by the third and most intense part of the pump beam, directed to the crystal by mirrors M9–11. The birefringent plates TD1 and TD2 serve to generate a time delay between the signal and idler, which are perpendicularly polarized. This time delay between signal and idler ensures that the pump pulse has temporal overlap only with signal.

Very high conversion efficiencies can be reached with the TOPAS, and with some effort, signal+idler energies of 300 μJ can be obtained. At idler wavelengths longer than 2.5 μm the BBO crystal starts to absorb, resulting in a much lower conversion efficiency. Thus the TOPAS cannot be used directly to generate the mid-IR pulses needed for experiments on OH-stretch bands, which are located in the 3 μm wavelength region.

2.4 Generation of intense ultrashort pulses in the 3000–3600 cm^{-1} frequency region

2.4.1 One-color setup

The signal wavelength of approximately 1.1 μm which corresponds to an idler in the 3 μm wavelength region can still be generated in BBO, although with a low conversion efficiency, since both signal and idler are needed in the parametric amplification process, and the idler photons are immediately absorbed after being generated. In order to produce pulses with sufficient intensity in the 3 μm wavelength region, we use a 5 mm thick KTP-crystal [45] cut at $\theta = 40°, \phi = 0°$ to amplify the weak signal output of the TOPAS at approximately 1.1 μ with the residual pump available at the output (see Fig. 2.4). KTP is a biaxial crystal [44], which means that it has three different refractive indices n_X, n_Y, n_Z. However, since two of these are nearly equal, it can in practice be regarded as a (positive) uniaxial crystal, with n_Z as the extraordinary refractive index. The signal output of the TOPAS is polarized perpendicular to the 800 nm pump and idler beams. The KTP is positioned with the Y-axis along pump (and idler) polarization, and phase matching is achieved by varying the angle between the crystal's Z-axis and the signal polarization.

At signal wavelengths around 1 μm the signal output of the TOPAS has a very broad power spectrum, both because of the absorption of the idler in BBO which reduces the length over which signal and idler interact, and because the tuning curve of the BBO is very steep in that wavelength region (see Fig. 2.2). As a consequence, the signal which serves as a seed for the parametric amplification in KTP has a very broad spectrum, and

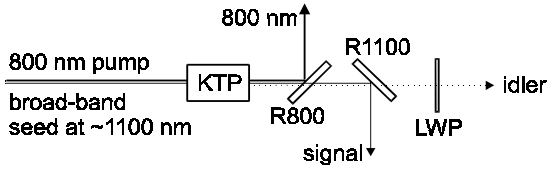

FIGURE 2.4. Setup for the generation of tunable mid-infrared pulses. LWP: long-wave pass filter; R800: 800 nm reflective mirror on CaF_2; R1100: 1060 nm reflective mirror on CaF_2.

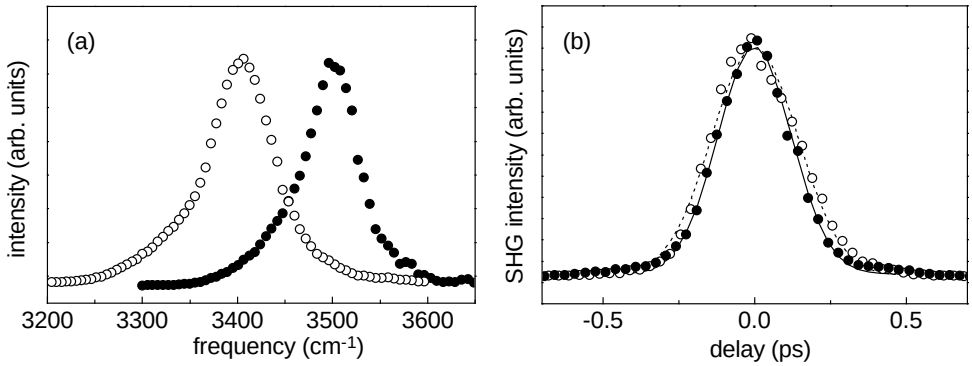

FIGURE 2.5. Power spectra and autocorrelation traces of the idler pulses generated with the one-color setup shown in Fig. 2.4. The open and solid points in the left and right panels match. (a) Power spectra recorded with a scanning monochromator and a PbSe detector. (b) Autocorrelation traces of the idler pulses, recorded in a 3 mm thick $LiIO_3$ crystal. The solid curve is a Gaussian fit to the solid points, with a FWHM of 0.287 ps, the dotted curve a Gaussian fit to the open points, with a FWHM of 0.335 ps.

the center wavelength of the resulting idler is determined mainly by the phase-matching angle of the KTP crystal.

We use a dielectric mirror to separate signal and idler, and a long-wave pass filter to block the remaining signal. In this way idler pulses of $\sim$200 fs and 30 μJ are generated in the 2.6-3.4 μm wavelength region. Typical power spectra, recorded using a scanning monochromator and a PbSe detector, and non-collinear autocorrelation traces, obtained using a 3 mm $LiIO_3$ crystal, are shown in Fig. 2.5. The idler pulses are not transform limited ($\Delta\nu\Delta\tau\sim0.6$) due to group velocity dispersion in the KTP crystal [28].

2.4.2 TWO-COLOR SETUP

In order to perform experiments in which the pump and probe pulses have different center frequencies, we use the setup shown in Fig. 2.6. In this setup, we exploit the fact that the frequency of the idler generated in the KTP crystals is determined mainly by the phase-matching angle of the KTP. Thus we can use the same signal output of the TOPAS to generate two different idler frequencies. To do this, the broadband seed pulse is split into two parts. The first part is combined with the 800 nm pump pulse in a KTP crystal to generate the intense pump pulse. The residual 800 nm pulse is used again with the second part of the seed to generate the weaker probe pulse in a second KTP crystal. Since depletion effects in the first KTP crystal deteriorate the beam profile of the pump pulse, only weak pulses can be obtained in the second crystal (energy typically less than 1 μJ). However, since the second pulse only serves as a probe, this poses no problems. The center frequencies of pump and probe are independently tunable by adjusting the phase-matching angle of the KTP crystals. Typical characteristics of the two-color setup are shown in Fig. 2.7.

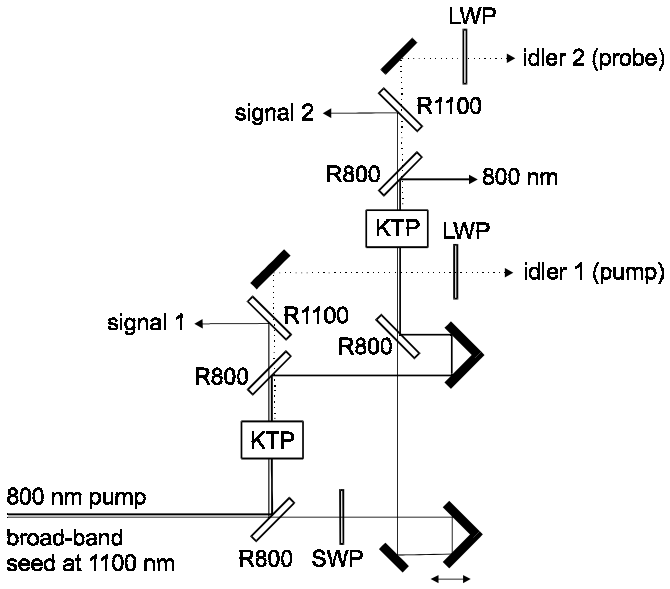

FIGURE 2.6. Two-color setup for the generation of indepently tunable mid-infared pump and probe pulses: SWP: short-wave pass-filter, cutoff at 2 μm; LWP: long-wave pass filter; R800: 800 nm reflective mirror on CaF_2; R1100: 1060 nm reflective mirror on CaF_2.

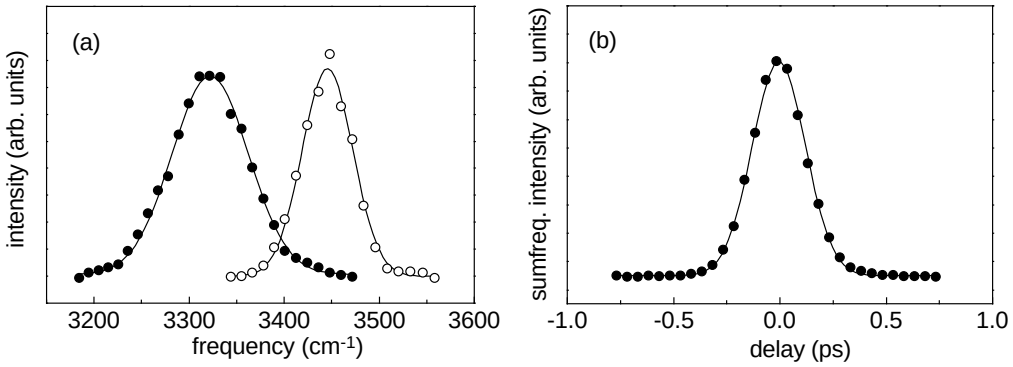

FIGURE 2.7. Characteristics of the idler pulses generated with the two-color setup shown in Fig. 2.6. (a) Power spectra of pump (solid points) and probe (open points) recorded with a scanning monochromator and a PbSe detector. The solid curves are Gaussian fits, with FWHM of 95 cm^{-1} and 63 $cm^{-1}$for pump and probe, respectively.(b) Cross-correlation trace, recorded by means of sum-frequency generation in a 5 mm thick $LiIO_3$ crystal. The solid curve is a Gaussian fit with a FWHM of 0.295 ps.

2.5 Pump-probe experiments

The pump-probe experiments are done with a standard pump-probe setup, a typical example of which is shown in Fig. 2.8. In the one-color pump-probe experiments, the infrared pulses are split into an intense pump pulse that excites a significant fraction of the molecules and a weak delayed probe pulse that monitors the induced transmission change. In the two-color exepriments the probe pulse is generated independently (see previous section). The pump and probe pulses are focused in the sample by a CaF_2 lens (focal length 100 mm), and the two beams enter the sample making an angle of less than 5°.

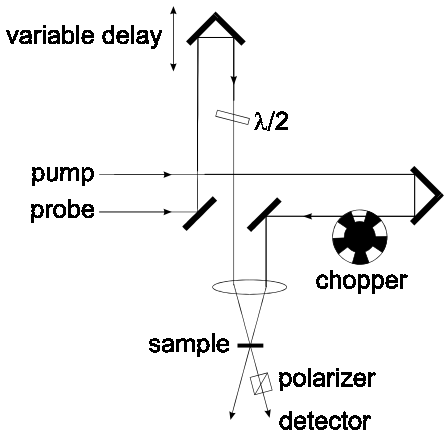

FIGURE 2.8. Pump-probe setup. The detector after the sample measures the transmission of the probe pulse in the presence (T) and absence (T_0) of the pump pulse. Part of the probe beam is split off before the sample, and measured by a second detector (not shown) for reference. The polarization of the probe pulse is rotated with respect to that of the pump pulse using a zero-order $\lambda/2$ plate.

The transmitted probe energy is measured with a PbSe detector placed after the sample. A part of the probe beam is split off (either by picking up the weak reflection from the $\lambda/2$ plate or by a CaF_2 plate) before the sample, and measured by a second PbSe detector for reference. The pump beam is chopped synchronously at 500 Hz, causing every other pump pulse to be blocked. The transmitted and reference signal are used to determine T, the transmission of the probe pulse in the presence of the pump pulse, and T_0, the transmission of the probe pulse in absence of the pump pulse. In a pump-probe scan the value of the normalized pump-induced absorption change $\ln(T/T_0)$ is determined as a function of the delay τ between pump and probe pulses.

The polarization of the probe pulse can be rotated with respect to that of the pump by means of zero-order $\lambda/2$-plate. In most experiments the probe polarization is set at the magic angle ($\arctan\sqrt{2} \approx 54.7°$) with respect to the pump. This ensures that the observed dynamics are not influenced by orientational effects [46]. The physical explanation for the value of the magic angle is as follows. The pump pulse is linearly polarized, and molecules with transition dipole moments along the pump polarization are preferentially excited. As a consequence, initially a larger value of $\ln(T/T_0)$ is measured if the polarization of the probe is parallel to that of the pump than when it is perpendicular. The orientational relaxation causes the parallel signal to decrease and the perpendicular signal to increase, and for a particular angle of the probe polarization these two effects should cancel. Since the transition dipole moment can escape to two dimensions other than the one of the pump polarization, but only one of these is probed with perpendicular probe polarization, the weight of the perpendicular contribution to the signal should be twice as large as that of the parallel contribution. Since the weights are given by the squares of the projections of the probe polarization on the parallel and perpendicular axes, the angle between the pump and probe polarizations should be $\arctan\sqrt{2}$. The reader might care to know that in an m-dimensional universe, the magic angle is $\arctan\sqrt{m-1}$ (for a dipole transition).

To study the orientational dynamics, the probe polarization is set at 45° with respect

to the pump pulse, and the parallel and perpendicular probe components are monitored separately by means of a polarizer placed behind the sample (Fig. 2.8). In the first orientationally resolved experiments (presented in Chapters 3 and 5), a large number of scans was recorded, in which the absorption change of either the parallel ($\ln(T_{||}/T_0)$) or the perpendicular ($\ln(T_{\perp}/T_0)$) component was monitored. The rotational anisotropy

$$R = \frac{\ln(T_{||}/T_0) - \ln(T_{\perp}/T_0)}{\ln(T_{||}/T_0) + 2\ln(T_{\perp}/T_0)} \tag{2.1}$$

was calculated afterwards from the 'parallel' and 'perpendicular' scans. In later experiments, a beam-splitter and two polarizers were used to monitor the parallel and perpendicular components simultaneously. In this way, the rotational anisotropy can be measured directly (on a single-shot basis). Identical results were obtained with the indirect and the direct method, except for the much better signal-to-noise ratio in the latter.

3 A femtosecond mid-infrared pump-probe study of hydrogen-bonding in ethanol

3.1 Introduction

The hydrogen bonds of alcohols in apolar solution have been the subject of numerous infrared spectroscopic studies [1, 15, 16, 47–53]. The strong influence of hydrogen-bond formation on the linear response of the OH-stretch mode of ethanol in apolar solution was established fifty years ago [1]. Since then, hydrogen-bonded alcohol has become one of the guinea pigs in the hydrogen-bond research field, and the coupling between the OH-stretch mode and the hydrogen bond in alcohol oligomers has been extensively characterized [47–51].

Nevertheless, detailed knowledge about the dynamical aspects of this coupling was lacking until recently. Graener, Ye and Laubereau [15, 16, 52] were the first to employ picosecond time-resolved mid-infrared pump-probe spectroscopy to investigate the dynamics of the OH-stretch mode of hydrogen-bonded ethanol oligomers in dissolved CCl_4. Their studies revealed that excitation of the OH-stretch mode of hydrogen-bonded ethanol results in a fast predissociation of the hydrogen bond, followed by a much slower reassociation process [15]. The time constant of the reassociation process was found to be 20 ± 5 ps, while an accurate determination of the predissociation lifetime was difficult as it was much shorter than the pulse length. In this Chapter, we present the first femtosecond mid-infrared pump-probe study of the OH-stretch mode of hydrogen-bonded ethanol in CCl_4.

3.2 Experiment

The pump-probe setup used for the experiments in this Chapter has been described in detail in Section 2.5. Mid-infrared pulses generated in a one-color setup (see Section 2.4.1) are split into an intense pump pulse ($\sim$20 μJ) that excites a significant fraction of the molecules, and a weak delayed probe pulse ($\sim$1 μJ) that monitors the induced transmission change. The pulses are focused in the sample by a CaF_2 lens (focal length 100 mm). In most experiments in this Chapter, the polarizations of the pump and probe pulses are parallel. Scans with perpendicularly polarized pump and probe pulses are obtained by means of a zero-order $\lambda/2$-plate in the probe beam. Auto-correlation traces of the mid-infrared pulses are recorded by means of second-harmonic generation in a 3 mm $LiIO_3$ crystal.

In the pump-probe scans the value of the pump-induced transmission change $\ln(T/T_0)$ is determined as a function of the delay τ between pump and probe pulses. We study

solutions of ∼0.4 mol/l ethanol dissolved in CCl_4. In order to avoid steady-state heating effects, the EtOH:CCl_4 solution is rapidly circulated.

3.3 Results

3.3.1 Hydrogen-bond predissociation

The effect of hydrogen bonding on the OH-stretch mode can clearly be seen in Fig. 3.1, which shows the linear infrared absorption spectrum of an 1.5 mol/l solution of ethanol in CCl_4. The fundamental OH-stretch region contains three distinct bands [15]. The intense broad band centered at ν_δ∼3330 cm^{-1} is due to absorption of hydroxylic groups at internal positions of hydrogen-bonded oligomers. The narrow absorption band at 3625 cm^{-1} is due to both hydroxylic groups of non-hydrogen bonded ethanol molecules ($\nu_\alpha = 3630$ cm^{-1}) and hydrogen-bond acceptor molecules at the end of open chain

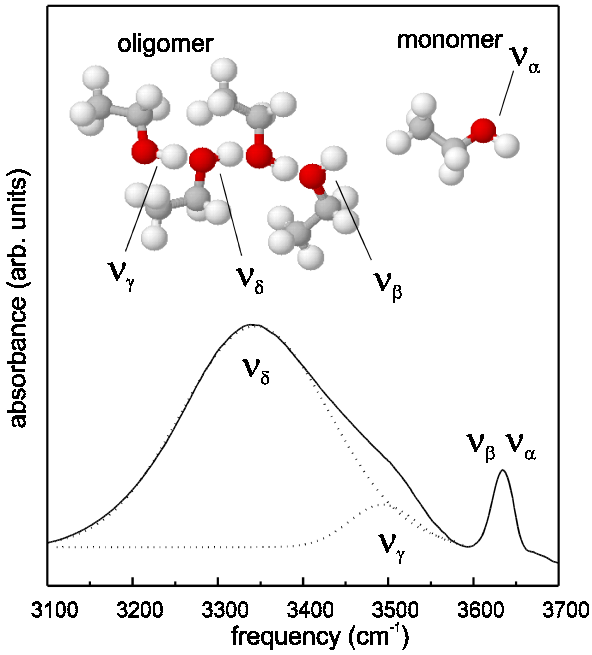

Figure 3.1. Infrared absorption spectrum of 1.5 mol/l ethanol in CCl_4 in the spectral region from 3100 to 3700 cm^{-1} at room temperature, showing the OH-stretch bands, labeled according to Ref. [15]. The dotted curves show the contributions of the internal hydroxylic groups and the terminal hydrogen-bond donor hydroxylic groups, centered at 3330 cm^{-1} (ν_δ) and 3500 cm^{-1} (ν_γ), respectively. The narrow absorption band at 3625 cm^{-1} is due to hydroxylic groups of isolated molecules (ν_α) and of hydrogen-bonded molecules at terminal hydrogen-bond acceptor positions (ν_β).

oligomers ($\nu_\beta = 3620$ cm^{-1}). The hydrogen-bond donor end groups of the open chain oligomers absorb at ν_γ∼3500 cm^{-1}. The integrated absorption cross sections of the internal and terminal hydrogen-bond donor hydroxylic groups are 12 and 3.5 times as large as that of the isolated and hydrogen-bond acceptor terminal groups [47].

We have recorded pump-probe scans with parallel polarizations of the pump and probe beams at four excitation frequencies within the broad OH-stretch band of the hydrogen-

bonded ethanol molecules at internal positions. Fig. 3.2 shows a delay scan recorded at 3330 cm^{-1}, close to the maximum of the absorption band. The population of the $v_{OH} = 1$ state of the hydrogen-bonded ethanol molecules results in a decreased absorption at the

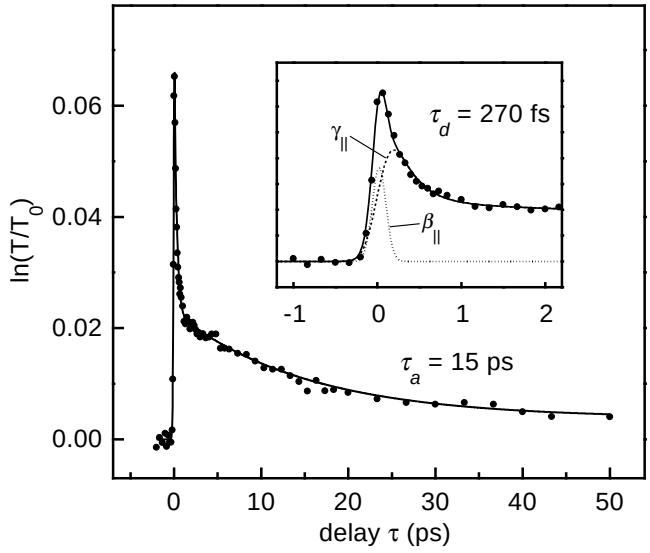

FIGURE 3.2. Delay scan showing the relative transmission change $\ln(T/T_0)$ vs. delay, recorded at an excitation frequency of 3330 cm^{-1}. The solid curve represents a calculation using values of $\tau_d = 270$ fs and $\tau_a = 15$ ps. In the inset, the dashed curve represents the incoherent contribution $\gamma_{||}(\tau)$ to the signal, the dotted curve the coherent contribution $\beta_{||}(\tau)$, as discussed in section 3.3.3.

$v_{OH} = 0 \rightarrow 1$ transition frequency. This bleaching decays in two stages: first a rapid decay takes place (time constant $\sim$250 fs), followed by a slower decay to a slightly elevated transmission level (time constant $\sim$15 ps). These transient bleaching effects cannot be due to a shift in the dissociation-association equilibrium of the oligomers, since temperature jump studies on the EtOH:CCl_4 system have shown that the response of this equilibrium to temperature changes occurs with a time constant of 240 ps [52]. The observed decay of the bleaching can be explained if the vibrational relaxation takes place by a rapid energy transfer from the OH stretching coordinate r_{OH} to the hydrogen-bond coordinate $r_{OH\cdots O}$ [15, 53]. The excitation energy exceeds the binding energy of the hydrogen bond, which is $\sim$2000 cm^{-1} [47]. This means that relaxation to the $v_{OH} = 0$ state leads to dissociation of the hydrogen bond. The depopulation of the $v_{OH} = 1$ state leads to a decrease of the population difference with the vibrational ground state and thereby to a decrease of the bleaching. The dissociation alters the distribution of hydroxylic groups, decreasing the number of internal groups and increasing the number of terminal groups. Since the terminal groups absorb at 3500 cm^{-1} and 3625 cm^{-1} [15], these will not be observed by the probe at 3330 cm^{-1}, so that the predissociation leads to a decrease of the bleaching to half its initial value. As the system relaxes to thermal equilibrium, the hydrogen bonds are again formed and the residual bleaching vanishes with a time constant of $\sim$15 ps. The transmission decays to a plateau value which is somewhat higher than observed for negative delay times because the equilibrium is reached at a slightly elevated temperature, at which there is a relatively smaller concentration of oligomers and thus a reduced absorption at 3330 cm^{-1}.

Fig. 3.3 shows a pump-probe scan recorded at an excitation frequency of 3225 cm^{-1}, at the red side of the absorption band. This scan shows an initial transmission decrease, which vanishes very rapidly (time constant ∼250 fs), followed by a bleaching which decays much more slowly (time constant ∼15 ps). The initial transmission decrease results

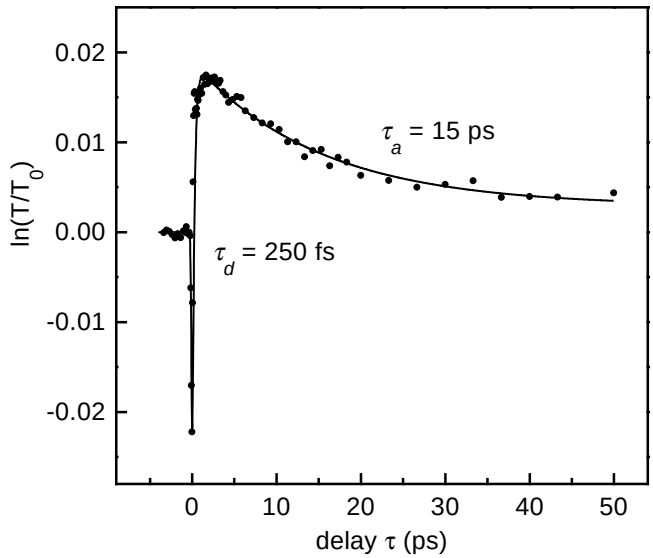

FIGURE 3.3. Delay scan showing the relative transmission change $\ln(T/T_0)$ vs delay, recorded at an excitation frequency of 3225 cm^{-1}. The solid curve represents a calculation using values of $\tau_d = 250$ fs and $\tau_a = 15$ ps.

from absorption of the excited $\nu_{OH} = 1$ state. Overtone studies have shown that the center frequency of the $\nu_{OH} = 1 \rightarrow 2$ absorption band is located at 3110 cm^{-1} [49]. Since the homogeneous linewidth of the $\nu_{OH} = 1 \rightarrow 2$ absorption band can be expected to be larger than that of the $\nu_{OH} = 0 \rightarrow 1$ transition [24], and the cross section of the $\nu_{OH} = 1 \rightarrow 2$ transition is approximately twice that of the $\nu_{OH} = 0 \rightarrow 1$ transition [54], at 3225 cm^{-1} the net effect of the bleaching at 3330 cm^{-1} and the induced absorption at 3110 cm^{-1} is a transmission decrease. Vibrational relaxation through dissociation of the hydrogen bond causes the induced absorption to vanish. As discussed above, the hydrogen-bond dissociation results in a residual bleaching at the OH-stretch frequency of the hydrogen-bonded internal hydroxylic groups, which causes the bleaching observed in Fig. 3.3. As the hydrogen bonds are again formed, the bleaching vanishes. The time constant of the hydrogen bond reassociation process is the same as observed at 3330 cm^{-1}. The observation of induced $\nu_{OH} = 1 \rightarrow 2$ absorption confirms that the system is in the $\nu_{OH} = 1$ state during a finite time before breaking of the hydrogen bond occurs. No significant $\nu_{OH} = 1 \rightarrow 2$ absorption was observed in Ref. [15], probably because the duration of pulses employed there exceeded by far the predissociation time constant.

To investigate whether the hydrogen-bond predissociation rate varies over the absorption band, we have also performed pump-probe scans at excitation frequencies of 3390 and 3450 cm^{-1} (Figs. 3.4 and 3.5). From these scans it is clearly observed that the predissociation lifetime increases significantly with the excitation frequency, reaching a value of ∼900 fs at 3450 cm^{-1}. At 3390 and 3450 cm^{-1} the dissociation of the hydrogen

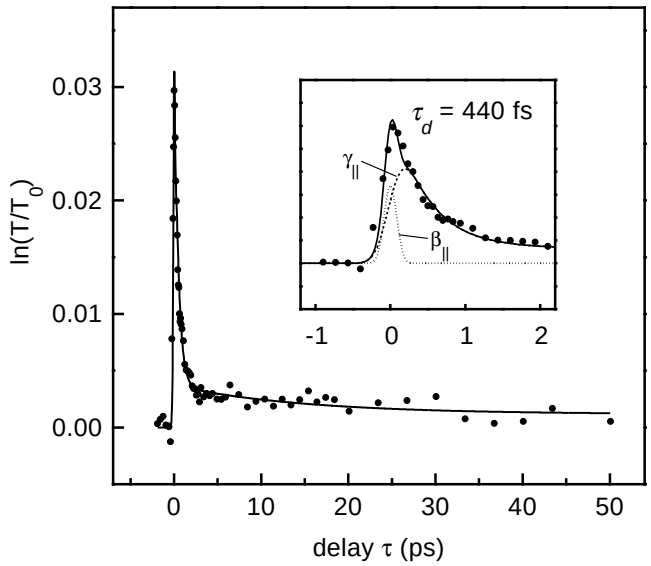

FIGURE 3.4. Delay scan showing the relative transmission change $\ln(T/T_0)$ vs delay, recorded at an excitation frequency of 3390 cm^{-1}. The solid curve represents a calculation using values of $\tau_d = 440$ fs and $\tau_a = 15$ ps. In the inset, the dashed curve represents the incoherent contribution $\gamma_{\|}(\tau)$ to the signal, the dotted curve the coherent contribution $\beta_{\|}(\tau)$.

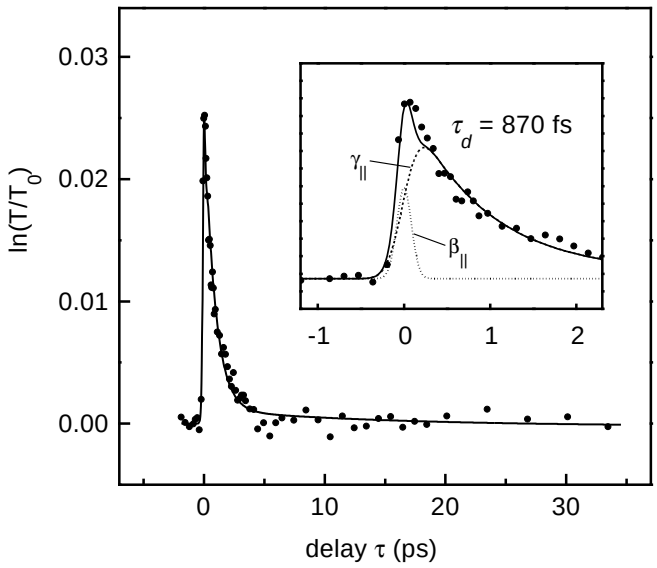

FIGURE 3.5. Delay scan showing the relative transmission change $\ln(T/T_0)$ vs delay, recorded at an excitation frequency of 3450 cm^{-1}. The solid curve represents a calculation using a value of $\tau_d = 870$ fs and $\tau_a = 15$ ps. In the inset, the dashed curve represents the incoherent contribution $\gamma_{\|}(\tau)$ to the signal, the dotted curve the coherent contribution $\beta_{\|}(\tau)$.

bond gives rise to a smaller residual bleaching than at 3225 and 3330 cm^{-1}. The cause for this effect is that the absorption increase at $\nu_\gamma = 3500$ cm^{-1} due to the creation of terminal hydroxylic groups becomes noticeable at these higher frequencies. To verify that predissociation does take place at high excitation frequencies, we have performed a picosecond two-color pump-probe experiment (using a setup described elsewhere [19]), in

which the pulses had a bandwidth of only 20 cm^{-1}. The result is shown in Fig. 3.6. If the ν_δ band is excited at 3450 cm^{-1}, then at a probe frequency of 3500 cm^{-1} indeed a transient absorption is observed. As expected, this absorption decays with a time constant of approximately 15 ps.

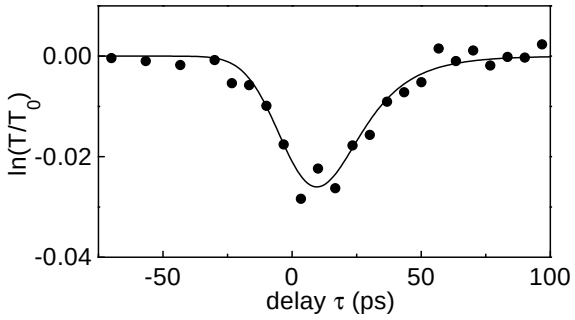

FIGURE 3.6. The points show a two-color pump-probe scan recorded with 20 ps long pulses, in a dilute EtOH:CCl_4 solution. The center frequency of the pump pulse is 3445 cm^{-1}, that of the probe pulse 3506 cm^{-1}. The decrease of the transmission at ν_γ shows that even at ν_{OH} frequencies as high as 3445 cm^{-1} dissociation of the hydrogen bond takes place upon excitation. The solid curve represents a convolution of the cross correlation function with an exponential decay with a time constant of 15 ps.

3.3.2 ORIENTATIONAL RELAXATION

The orientational dynamics of the OH-stretch excitation of the hydrogen-bonded ethanol molecules can be investigated by varying the polarization of the probe pulse with respect to that of the pump pulse. Fig. 3.7 shows two delay scans recorded at 3390 cm^{-1}, one with perpendicular and one with parallel polarizations of the pump and probe pulses. In order to determine accurately the ratio of the signals with parallel and perpendicular polarizations, these scans were recorded by adjusting the $\lambda/2$-plate such as to rotate the polarization of the probe beam 45° with respect to that of the pump beam, and monitoring either the parallel or perpendicular component of the probe beam by means of a polarizer placed in front of the PbSe detector.

The time dependence of the ratio of the pump-probe signals for parallel and perpendicular polarizations is determined by the orientational relaxation of the vibrational excitation. For delays larger than the pulse length, the observed pump-probe signals for parallel and perpendicular polarizations decay with the same time constant, and the ratio of the pump-probe signals $\ln(T_\perp/T_0)/\ln(T_\parallel/T_0)$ has a constant value of $\sim$0.7, which is much larger than the value of 1/3 expected in the case of very slow orientational relaxation [55]. This implies that orientational relaxation occurs on a time scale much faster than the pulse length. Curiously, the ratio of the pump-probe signals with perpendicular and parallel polarizations is less than unity, indicating that the orientational distribution of the excitation has not become fully isotropic after the orientational relaxation.

The most likely mechanism for the fast orientational relaxation is delocalization of the OH-stretch vibration over the hydrogen-bonded oligomer through dipole-dipole coupling. The hydrogen bond is approximately linear, and directed towards a lone electron

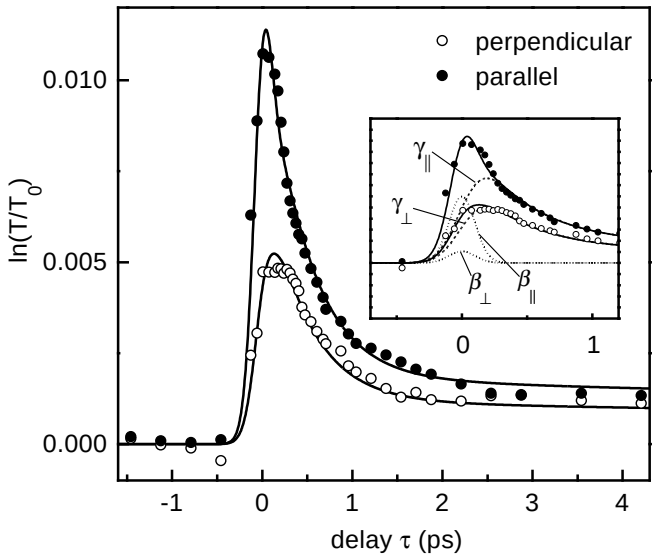

FIGURE 3.7. Delay scans showing the relative transmission change $\ln(T/T_0)$ vs delay, recorded with parallel and perpendicularly polarized pump and probe pulses at an excitation frequency of 3390 cm^{-1}. The solid curves represent the calculated signals, using values of $\tau_d = 440$ fs and $\rho = 0.65$. The dashed curves represent the incoherent contribution $\gamma(\tau)$ to the signal, the dotted curves the coherent contribution $\beta(\tau)$.

pair-containing sp^3 orbital on the oxygen atom of the hydrogen-bond acceptor [6]. This means that within a hydrogen-bonded oligomer the OH bonds point in different directions, and that energy transfer from one hydroxylic group to another leads to orientational scrambling of the vibrational excitation. Since the oligomers contain a finite number of ethanol molecules, the orientational distribution of the vibrational excitation is not completely randomized by the delocalization process, but still has a maximum in the direction parallel to the polarization of the excitation field. A rough estimate for the dipole-dipole energy-transfer rate $k_{a\to b}$ from an excited hydroxylic group a to its nearest neighbor b can be obtained from the Förster expression [56, 57], which in SI units is given by:

$$k_{a\to b} = \frac{\mu_a^2 \mu_b^2 \kappa_{ab}^2}{16\pi^2 n^4 \varepsilon_0^2 \hbar^2 c R_{ab}^6} \int d\nu\, g_a(\nu) g_b(\nu). \tag{3.1}$$

In this expression $\mu_a = \mu_b$ is the transition dipole moment, n the refractive index of the medium surrounding the dipoles, R_{ab} the distance between the dipoles, and $g_{a,b}(\nu)$ are the normalized vibrational line shapes. The relative orientation of the dipoles is expressed by the factor κ_{ab}, which is given by $\kappa_{ab} = \cos\theta_{ab} - 3\cos\theta_a \cos\theta_b$, where θ_{ab} is the angle between the two dipole vector and $\theta_{a,b}$ are the angles between the dipole vectors and the interdipole vector. If it is assumed that two hydroxylic groups have roughly the same excitation frequency, then because of the large homogeneous linewidth of the OH-stretching vibration [15], the integral in Eq. (3.1) will be of the order of unity. Assuming a tetrahedral geometry around the acceptor oxygen atom ($\theta_{ab} = 70°$), and assuming that the dipoles are located at the center of the OH bonds, we have $R_{ab} = 2.53$ Å and $\kappa_{ab} = -1.14$, where an O$\cdots$O distance of 2.8 Å, known from neutron diffraction studies [58], and an OH bond length of 0.967 Å [59] have been used. From the integrated absorption cross section

of the hydrogen-bonded ethanol [47], a value of $\mu = 0.18$ D is found for the transition dipole moment. Furthermore assuming $n = 1.5$, we obtain $k_{a\to b} = (0.3 \text{ fs})^{-1}$. Although this is only a very rough estimate, its order of magnitude does indicate that the very fast orientational relaxation might indeed be caused by delocalization of the OH-stretch excitation over the hydrogen-bonded ethanol oligomers. Dielectric relaxation and nuclear magnetic resonance studies have shown that the orientational relaxation of isolated ethanol molecules and of the hydrogen-bonded oligomer as a whole take place on a much slower time scale [60, 61].

3.3.3 Analysis

In the quantitative interpretation of the data, the influence of coherent coupling effects on the pump-probe signal has to be taken into account [34, 46, 62, 63]. In our experiment pump and probe pulses have the same central wavelength and are non-collinear. This means that when the delay is smaller than the coherence time of the field, the pump and probe pulses will interfere and induce a spatial modulation (grating) of the intensity and thus a grating of the light-induced change in the absorption and refractive index [64]. This grating diffracts the pump pulse into the direction of the probe beam, and constructive interference of the diffracted pump light with the probe leads to an increase of the transmitted probe signal.

The pump-probe transients could in principle be influenced by the free-induction decay, which may alter the pulse shape as the pulse propagates through the sample [65, 66]. However, if the free-induction decay takes place much faster than the pulse coherence time (which in our experiments is nearly equal to the pulse length), this effect does not influence the transients, and the pump-probe signal (including the coherent coupling effect) can be described using a relatively simple model [63]. The time constant of the free-induction decay, which is the inverse of the width of the OH-stretch absorption spectrum, is approximately 25 fs. This is certainly much shorter than the pulse duration, and therefore the present experiment can be well described by the model of Ref. [63]. It should be noticed that spectral diffusion cannot have a significant influence on the transients, since the bandwidth of our laser pulses is very close to the value obtained for the homogeneous linewidth measured using pulses of 10 ps [15]. In this Section, first the case of parallel polarizations of the pump and probe pulses is discussed, then that of perpendicular polarizations. Our analysis follows that of Ref. [62] and Section 1.3.2.

If we write the pump and probe fields as in Eq. (1.4) (with $j = 1$ for the pump and $j = 2$ for the probe), then the unperturbed pump and probe fields $\tilde{E}_j^{(1)}(t)$ are given in the slowly-varying envelope approximation by Eq. (1.8). Since the probe pulse is a weak time-delayed copy of the pump pulse, we have

$$\tilde{E}_1^{(1)}(z,t) = e^{-\frac{1}{2}\alpha_0 z}\tilde{E}(t - z/v) \tag{3.2}$$

$$\tilde{E}_2^{(1)}(z,t) = \zeta\, e^{i\omega\tau - \frac{1}{2}\alpha_0 z}\tilde{E}(t - \tau - z/v), \tag{3.3}$$

where $\omega = \omega_1 = \omega_2$, $\alpha_0 = \alpha_0(\omega_1) = \alpha_0(\omega_2)$, and $\tilde{E}(t) = \tilde{E}_1(0,t)$ is the pump-field in $z = 0$ (at the beginning of the sample). The value of ζ^2 is less than 0.05.

The pump and probe fields interact to give rise to a third-order polarization at frequency ω in the probe direction $\mathbf{k}_2$ which for pump and probe pulses polarized in the x direction is given by [63]

$$P^{(3)}(z,t) \propto \tilde{E}_1(z,t)\int_{-\infty}^{t} dt' \int_{-\infty}^{t'} dt'' \tilde{E}_1^*(z,t')\tilde{E}_2(z,t'')A_{xxxx}(t'-t'') + \tilde{E}_2(z,t)\int_{-\infty}^{t} dt' \int_{-\infty}^{t'} dt'' \tilde{E}_1^*(z,t')\tilde{E}_1(z,t'')A_{xxxx}(t'-t''), \quad (3.4)$$

where $A_{xxxx}(t) = A'_{xxxx}(t) + iA''_{xxxx}(t)$ describes the response of the third-order susceptibility tensor. Since for approximately transform-limited pulses the spatial modulation of the refractive index only results in a second-order intensity change of the probe pulse [63, 64], the present calculation only takes the modulation of the absorption into account, *i.e.*, of the imaginary part $A''_{xxxx}(t)$ of the third-order susceptibility.

The energy loss of the probe pulse as a consequence of the third-order polarization is proportional to $\mathrm{Im}\int dt\, \tilde{E}_2^{(1)*}(0,t)\tilde{P}^{(3)}(0,t)$, see Section 1.3.2. Substituting Eq. (3.2) and (3.3) in Eq. (3.4), we find an explicit expression for the third-order polarization that can be used to calculate the pump-probe signal:

$$\begin{aligned} S(\tau) &\propto \mathrm{Im}\int_{-\infty}^{\infty} dt\; \tilde{E}_2^{(1)*}(0,t)\tilde{P}^{(3)}(0,t) \\ &\propto \gamma_{\parallel}(\tau) + \beta_{\parallel}(\tau), \end{aligned} \quad (3.5)$$

where

$$\gamma_{\parallel}(\tau) = \int_{-\infty}^{\infty} dt \int_{-\infty}^{t} dt' |\tilde{E}(t-\tau)|^2 |\tilde{E}(t')|^2 A''_{xxxx}(t-t') \quad (3.6)$$

and

$$\beta_{\parallel}(\tau) = \int_{-\infty}^{\infty} dt \int_{-\infty}^{t} dt' \tilde{E}^*(t-\tau)\tilde{E}(t)\tilde{E}^*(t')\tilde{E}(t'-\tau)A''_{xxxx}(t-t'), \quad (3.7)$$

and L is the length of the sample. This equation is in agreement with the expressions obtained in Refs. [62, 64] for the pump-probe signal with parallel polarized pump and probe pulses, and holds for arbitrary optical thickness $\alpha_0 L$ of the sample (see Section 1.3.2). The first term in this expression represents the incoherent pump-probe signal, and depends only on the pulse envelope function. The second term, which is only non-zero when the pump and probe pulses coincide in time and are mutually coherent in the sample, represents the coherent coupling effect. This term contains the fourth-order correlation function of the field amplitude. Since the infrared pulses are not fully transform-limited, and since the nature of the phase-modulation is not known, this correlation function cannot be evaluated. However, provided the response function $A''_{xxxx}(t)$ decays slowly compared to the coherence time of the field, knowledge of the nature of the phase modulation is not required, since in that case $A''_{xxxx}(t)$ can be approximated to first order by $A''_{xxxx}(0)$, which simplifies $\beta_{\parallel}(\tau)$ to

$$\beta_{\parallel}(\tau) = \frac{1}{2}A''_{xxxx}(0)\left|\int_{-\infty}^{\infty} dt \tilde{E}^*(t-\tau)\tilde{E}(t)\right|^2. \quad (3.8)$$

It is seen that in this case the coherent coupling part of the signal is proportional to the square of the first-order coherence function of the pulses. This coherence function is the inverse Fourier transform of the power spectrum of the pulses [67]. Therefore, knowledge of the power spectrum and the intensity envelope of the pulses is sufficient to describe the data, and the nature of the phase-modulation is not relevant.

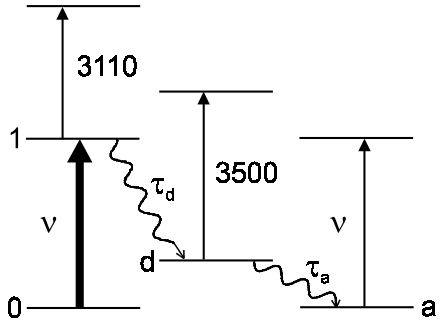

FIGURE 3.8. Schematic representation of the energy levels used in the calculation. Resonant excitation (indicated by the thick arrow) at frequency ν results in population transfer from the $v_{OH} = 0$ to the $v_{OH} = 1$ state. As a consequence, $v_{OH} = 1 \rightarrow 2$ absorption becomes possible at 3110 cm^{-1}. Relaxation with a time constant τ_d results in a change in absorption frequency due to the breaking of the hydrogen bonds. Reassociation of the hydrogen bonds occurs with a time constant τ_a, to a new equilibrium at an elevated temperature. The increase in temperature results in a slightly different absorption cross section for level 3 as compared to level 0.

We now set out to derive the response function $A''_{xxxx}(t)$ for the hydrogen-bonded OH-stretch excitation (see Fig. 3.8). Orientational effects do not have to be taken into account, since due to the fast orientational relaxation the orientational distribution can be assumed to be time independent. Resonant excitation at frequency ν leads to population transfer from the $v_{OH} = 0$ (n_0) to the $v_{OH} = 1$ (n_1) state of the hydrogen-bonded internal ethanol molecules. Vibrational relaxation takes place with a time constant τ_d by predissociation of the hydrogen bond. This leads to creation of terminal hydroxylic groups (n_d) which absorb at 3500 cm^{-1}. Subsequently, reassociation of the hydrogen bonds takes place with a time constant τ_a. The hydrogen-bonded hydroxylic groups created in this way (n_a) will have a slightly different absorption cross section due to the temperature increase in the sample. The equations for the population density of the excited state levels at a given position in the sample and for an intensity profile $I(t)$ at that position are:

$$\frac{dn_1}{dt} = \sigma_0(n_0 - n_1)I(t) - \frac{n_1}{\tau_d} \tag{3.9}$$

$$\frac{dn_0}{dt} = -\sigma_0(n_0 - n_1)I(t) \tag{3.10}$$

$$\frac{dn_d}{dt} = \frac{n_1}{\tau_d} - \frac{n_d}{\tau_a} \tag{3.11}$$

$$\frac{dn_a}{dt} = \frac{n_d}{\tau_a}. \tag{3.12}$$

The transient absorption coefficient $\alpha_{\|}(t)$ at a given position is given by

$$\alpha_{\|}(t) = \sigma_0(n_0 - n_1) + \sigma_1 n_1 + \sigma_{\rm d} n_{\rm d} + \sigma_{\rm a} n_{\rm a}, \tag{3.13}$$

where σ_q are the effective cross sections of the different energy levels, labeled as in Fig. 3.8. Note that these effective cross sections depend on the probing frequency. The response function $A''_{xxxx}(t)$ is defined by [64]

$$\Delta\alpha_{\|}(t) = \alpha_{\|}(t) - \alpha_0 = \alpha_0 \int_{-\infty}^{t} dt'\, I(t') A''_{xxxx}(t - t'), \tag{3.14}$$

where $\alpha_0 = \sigma_0 n_{\rm tot}$ (with $n_{\rm tot} = n_0 + n_1 + n_{\rm d} + n_{\rm a}$ the total population density) is the equilibrium absorption coefficient. Since the population changes are small (typically 5%), the term $\sigma_0(n_0 - n_1)$ at the right-hand side of Eq. (3.9) can be approximated by α_0, and by integrating Eqs. (3.9−3.12) it is easily shown that for the four-level model used here, the response function is given by

$$\begin{aligned} A''_{xxxx}(t) = {} & (\sigma_1 - \sigma_0 + \sigma_{\rm d}\frac{\tau_{\rm a}}{\tau_{\rm d} - \tau_{\rm a}} - \sigma_{\rm a}\frac{\tau_{\rm d}}{\tau_{\rm d} - \tau_{\rm a}})\, e^{-t/\tau_{\rm d}} \\ & + (\sigma_{\rm a} - \sigma_{\rm d})\frac{\tau_{\rm a}}{\tau_{\rm d} - \tau_{\rm a}}\, e^{-t/\tau_{\rm a}} + \sigma_{\rm a} - \sigma_0. \end{aligned} \tag{3.15}$$

Here, $\tau_{\rm d}$ and $\tau_{\rm a}$ are the time constants of the predissociation and reassociation processes. Substitution of Eq. (3.15) in Eq. (3.5) results in an explicit expression for the pump-probe signal.

The numerical analysis of the data was performed by using as input parameters the experimentally determined FWHM of the pulse envelope and of the power spectrum, which are both assumed to be gaussian. The power spectrum was used to calculate the first-order coherence function which occurs in Eq. (3.8). A least-squares fit was performed to obtain values for the predissociation time constant $\tau_{\rm d}$ at the four different excitation frequencies ranging from 3225 to 3450 cm^{-1}. The reassociation time constant $\tau_{\rm a}$ was determined by a least-squares fit to the results at 3225 and 3330 cm^{-1}, and was kept fixed at 15 ps in the least-squares fits to the results at 3390 and 3450 cm^{-1}. The results of the least-squares fitting procedure are given in Table 3.1 and are shown as the solid curves in Figs. 3.2−3.5. The value obtained for the time constant of the hydrogen-bond reassociation process is in agreement with the value of 20±5 ps obtained in the picosecond studies [15]. It must be realized that there might exist a distribution of reassociation time constants in the solution. In that case the value of $\tau_{\rm a}$ obtained here would represent an average over this distribution. The predissociation lifetime reported in Ref. [15] (5±3 ps) is significantly larger than the values obtained here. Probably the length of the pulses employed in that study (10 ps) rendered an accurate determination of $\tau_{\rm d}$ difficult.

The largest observed vibrational lifetime (870 fs) of the hydrogen-bonded ethanol is still an order of magnitude shorter than the lifetime of non-hydrogen bonded ethanol in CCl_4 solution, which has been found to be 8 ps [68]. This indicates that the hydrogen-bond predissociation is indeed a very efficient relaxation channel. It is evident that the predissociation time constant depends strongly on the excitation frequency. This means that the

OH stretching band of the hydrogen-bonded oligomers is inhomogeneously broadened, as was observed previously in picosecond studies on EtOH:CCl_4 [15]. It is well-known that the redshift of the OH-stretch frequency is a measure of the hydrogen-bond strength [69]. Apparently, weaker hydrogen-bonding leads to slower predissociation. In fact, studies on hydrogen-bonded acid:base systems [18, 70] have shown that for very weak hydrogen bonds (small redshift) no significant predissociation occurs. To our knowledge, a frequency dependence of the predissociation rate of the hydrogen bond in the condensed phase, which has been predicted in theoretical studies [53], has not been observed previously.

The results obtained with perpendicular polarizations can be described quantitatively by assuming that the orientational relaxation takes place much faster than the time scale of the experiment, and that it results in an orientational distribution of the vibrational excitation which is time independent. The expression for the pump-probe signal obtained with the pump pulse polarized in the *x* direction and the probe pulse in the *y* direction contains the A''_{yyxx} and A''_{yxxy} components of the third-order susceptibility tensor [62]. Following Ref. [62], we define the depolarization factor

$$\rho = A_{yyxx}/A_{xxxx}, \tag{3.16}$$

which has a value between 1/3 (no orientational scrambling) and 1 (complete orientational scrambling) [62]. If ρ is time independent and the medium isotropic, it can be shown that the incoherent and coherent parts $\gamma_\perp(\tau)$ and $\beta_\perp(\tau)$ of the pump-probe signal observed with perpendicularly polarized pump and probe pulses are related to those observed with parallel polarized pulses by [62]:

$$\gamma_\perp(\tau)/\gamma_\parallel(\tau) = \rho \tag{3.17}$$

$$\beta_\perp(\tau)/\beta_\parallel(\tau) = (1-\rho)/2. \tag{3.18}$$

This means that the difference between the pump-probe scan recorded with parallel polarizations and the pump-probe scan obtained with perpendicular polarizations is determined by ρ only. From a least-squares fit to the results shown in Fig. 3.7 we obtain $\rho = 0.65 \pm 0.05$, which is equivalent to a value of the rotational anisotropy (defined as $R = [\Delta\alpha_\parallel - \Delta\alpha_\perp]/[\Delta\alpha_\parallel + 2\Delta\alpha_\perp]$ [55]) of 0.15 for delays larger than the pulse length.

TABLE 3.1. Predissociation lifetime τ_d and reassociation time constant τ_a at different excitation frequencies ν, obtained from numerical analysis of the data (shown as the solid lines in Figs. 3.2–3.5). The values in parentheses represent 2σ.

ν/cm^{-1}	τ_d/fs	τ_a/ps
3225	250 (50)	15 (3)
3330	270 (40)	15 (3)
3390	440 (40)	
3450	870 (90)	

Note that with perpendicular polarizations the pump-probe signal contains a much smaller coherent coupling contribution than with parallel polarizations. This can be understood as follows. If the polarizations of the exciting fields are perpendicular, there is no spatial intensity modulation, and a coherent coupling effect can only result from an orientational grating. However, due to the virtually instantaneous rotational scrambling only a very weak orientational grating will be present. This results in a comparatively small coherent coupling contribution if the pump and probe pulses have orthogonal polarizations. Since the coherent contribution to $\ln(T_\perp/T_0)$ is smaller than that to $\ln(T_\parallel/T_0)$, the difference between these transmission changes will decay rapidly with increasing delay. This decay is not due to an orientational relaxation process but simply due to the decay of the different coherent contributions. Hence, the signals at small delays only provide information on the orientational distribution of the molecules if the coherent-coupling contributions $\beta_\parallel(\tau)$ and $\beta_\perp(\tau)$ are properly accounted for.

3.4 Conclusions

In this Chapter, we have presented a femtosecond mid-infrared pump-probe study of the vibrational relaxation of the OH-stretch mode of hydrogen-bonded ethanol oligomers. Upon excitation to the $\nu_{OH} = 1$ state, vibrational relaxation takes place on the femtosecond time scale by predissociation of the hydrogen bonds. The predissociation time constant increases strongly with the excitation frequency, indicating that the predissociation rate depends strongly on the hydrogen-bond strength. The reassociation was observed to occur with a time constant of 15 ps, in accordance with previous studies. Finally, a very fast orientational relaxation of the OH-stretch excitation is observed, which is explained by a rapid delocalization of the vibrational stretching excitation over the hydrogen-bonded ethanol oligomers.

4 Vibrational dynamic Stokes shift in liquid water

4.1 Introduction

It was discussed in Chapter 1 that for hydrogen-bonded $O-H\cdots O$ systems the OH-stretch frequency ν_{OH} is strongly correlated to the hydrogen-bond length $R_{O-H\cdots O}$. This correlation results from the difference between the potential-energy functions of the hydrogen-bond mode in the $v_{OH}=0$ and $v_{OH}=1$ states. These potential energy functions have approximately the same shape, but in the $v_{OH}=1$ state the minimum occurs at a smaller value of $R_{O-H\cdots O}$ than in the $v_{OH}=0$ state [8, 11, 71–73]. If the hydrogen-bond potentials are harmonic, this results in a linear relationship between ν_{OH} and $R_{O-H\cdots O}$ [11], in agreement with experimental observations [14].

In isolated (gas-phase) hydrogen-bonded complexes, the difference between the hydrogen-bond potentials in the $v_{OH}=0$ and $v_{OH}=1$ states leads to Franck-Condon progressions in the ν_{OH} spectra [74, 75]. In the condensed phase, the hydrogen-bond mode is strongly damped by interaction with bath modes, resulting in a smooth and broad ν_{OH} absorption band. Upon excitation from the $v_{OH}=0$ to the $v_{OH}=1$ state, the hydrogen-bond will initially be in a non-equilibrium position of the $v_{OH}=1$ potential. Subsequent relaxation (contraction) of the hydrogen-bond to its equilibrium position in the $v_{OH}=1$ state should lead to a dynamic Stokes shift of the ν_{OH} frequency of the excited molecule, in close analogy with the dynamic Stokes shift observed in electronic transitions of fluorescent probe molecules in liquid solution [76].

For harmonic hydrogen-bond potentials (see Fig. 1.1), the relation between the Stokes shift 2λ (in units of angular frequency) and the absorption lineshape $e^{-\omega^2/2\Delta^2}$ is relatively simple [35]:

$$2\lambda = \bar{h}\Delta^2/k_B T, \tag{4.1}$$

with $\bar{h}$ Planck's constant, k_B Boltzmann's constant, and T the temperature. It is clear from this expression that there will be a significant Stokes shift for strongly hydrogen-bonded systems for which the variation in $R_{O-H\cdots O}$ results in a broad absorption band. For instance, for the ν_{OH} mode of HDO dissolved in D_2O, the width (FWHM) of the absorption band of 260 cm^{-1} corresponds to a Stokes shift of approximately 60 cm^{-1}. Nevertheless, a vibrational Stokes shift has never been experimentally observed. This can be partly understood from the fact that it is impossible to observe a vibrational Stokes shift in the fluorescence spectrum, since the quantum yield of the fluorescence will be extremely low due to the short vibrational lifetime of hydrogen-bonded systems in the condensed phase. The Stokes shift can also be probed using ultrafast transient absorption spectroscopy [35]. Unfortunately, for an OH-stretch vibration, the shape of the transient spectrum is strongly affected by excited-state absorption and the very fast and frequency-dependent vibrational relaxation, which makes it far from straightforward to observe the

Stokes shift. As a result, in previous picosecond [22, 23] and femtosecond [31] pump-probe studies of the spectral relaxation of the ν_{OH} mode of HDO:D_2O, the vibrational Stokes shift was not observed. In the femtosecond study [31], the time resolution was sufficient to resolve the spectral dynamics, but the dynamics were interpreted in terms of the first moment of the transient spectrum. This is a very poor parameter to infer a Stokes shift, due to the excited-state absorption and the vibrational relaxation.

In this Chapter, we present the first experimental observation of a vibrational dynamic Stokes shift. This Stokes shift is observed in a femtosecond pump-probe study on the ν_{OH} mode of HDO dissolved in deuterated water (D_2O). The essential difference with the previous work on this system is that the dynamics of the spectral response are investigated via delay scans obtained with different colors for the pump and probe rather than by the first spectral moment. As will be shown, this method has decisive advantages in providing evidence for a vibrational dynamic Stokes shift.

4.2 Experiment

With the two-color setup described in Section 2.4.2, two independently tunable 200 fs mid-infrared pulses are generated. One of these pulses has an energy of $\sim$25 μJ and is used as pump, the other has an energy of less than 1 μJ and is used as probe. The pump pulse is tuned to a specific frequency in the broad $v_{OH} = 0 \rightarrow 1$ absorption band, and the probe frequency is either redshifted of blueshifted with respect to the pump. The pump pulse induces a significant population of the $v_{OH} = 1$ level. This results in transient absorption changes, which are monitored by the probe pulse. The probe polarization is at the magic angle with respect to the pump polarization, ensuring that the observed signals are not influenced by orientational dynamics (see Section 2.5). The sample consists of a 500 μm layer of dilute ($\sim$1:200) solution of HDO in D_2O, prepared by mixing the appropriate amounts of H_2O (HPLC grade) and D_2O (>99.9 atom% D), and is kept between two CaF_2 windows at room temperature (298 K). The water is circulated to avoid steady-state heating effects.

4.3 Results and discussion

Figure 4.1 presents pump-probe scans recorded with a pump frequency of 3450 cm^{-1} and redshifted probe frequencies of 3363 and 3330 cm^{-1}. We took care that the pump and probe have negligible spectral overlap to avoid coherent artefacts. Also shown is a convolution of the cross-correlation of pump and probe with an exponential decay e^{-t/T_1} ($T_1 = 740$ fs, see Chapter 6), which represents the pump-probe signal for instantaneous response that would be observed if no spectral relaxation would take place on the time scale of the experiment. At a probe frequency of 3363 cm^{-1}, the pump-probe signal rises significantly more slowly than this calculated convolution. At a probe frequency of 3330 cm^{-1}, the pump-probe signal rises even more slowly. Figure 4.2 shows pump-probe scans recorded with a pump frequency of 3320 cm^{-1} and blueshifted probe frequencies of 3445 and 3500 cm^{-1}. If the probe is tuned to 3445 cm^{-1}, the measurement can be well described by a convolution of the cross-correlation with e^{-t/T_1}. Only if the probe is tuned

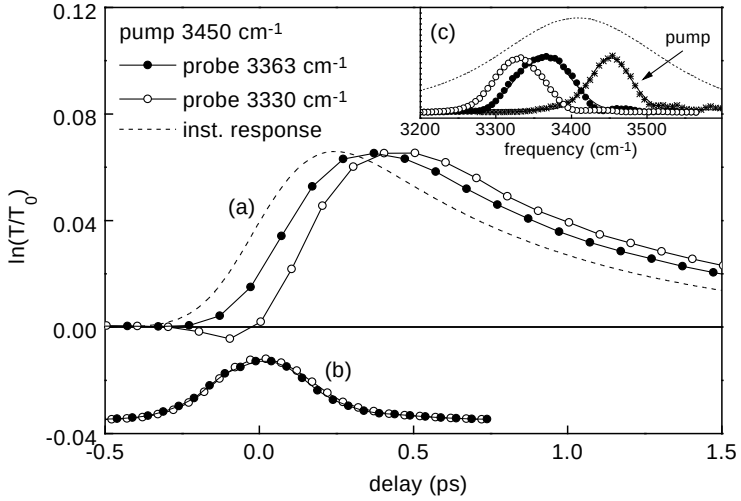

FIGURE 4.1. (a) Pump-probe scans recorded in dilute HDO:D_2O at room temperature, showing the transmission change $\ln(T/T_0)$ of the probe pulse as a function of the delay between pump and probe, with a pump frequency of 3450 $cm^{-1}$and probe frequencies of 3363 and 3330 cm^{-1}. The dashed curve represents the convolution of the cross-correlation with an exponential decay e^{-t/T_1}, with $T_1 = 740$ fs (see Chapter 6). (b) Cross-correlation traces of the pump and probe pulses. (c) Power spectra of the pump and probe pulses (represented as stars and circles, respectively), and the OH-stretch absorption band (dashed curve).

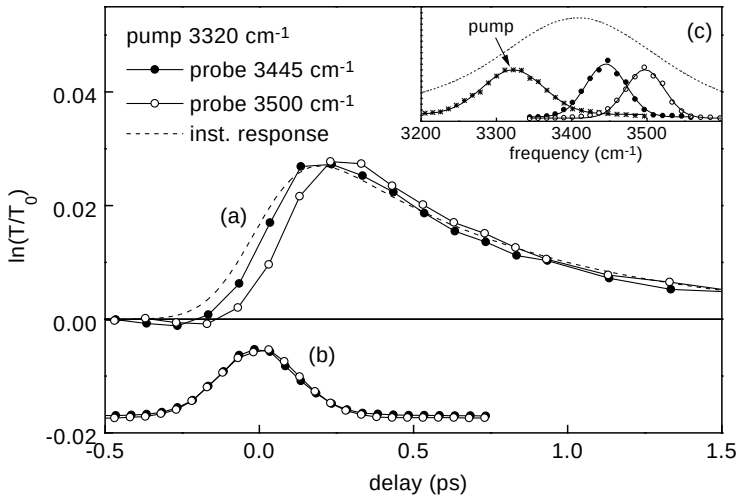

FIGURE 4.2. (a) Pump-probe scans recorded in dilute HDO:D_2O at room temperature, with a pump frequency of 3320 $cm^{-1}$and probe frequencies of 3445 and 3500 cm^{-1}. The dashed curve is the convolution of the cross-correlation with an exponential decay e^{-t/T_1}, with $T_1 = 740$ fs [77]. (b) Cross-correlation traces of the pump and probe pulses. (c) Power spectra of the pump and probe pulses, and the OH-stretch absorption band.

to 3500 cm^{-1}, the pump-probe signal is slightly delayed with respect to the instantaneous signal. It is also observed that the bleaching signals are much smaller than in Fig. 4.1. From the difference between the measurements presented in Figs. 4.1 and 4.2 it is clear that with increasing delay, the bleaching signal broadens much stronger towards lower fre-

quencies than towards higher frequencies. This observation shows that a dynamic Stokes shift of the ν_{OH} frequency indeed occurs in liquid HDO:D_2O.

Figure 4.3 shows schematically what happens after excitation at a specific ν_{OH} frequency. The bleaching is caused by both the depletion of the $v_{OH} = 0$ state (usually referred to as the 'hole' contribution [35]) and the population of the $v_{OH} = 1$ state (the 'particle' contribution [35]). After excitation from the $v_{OH} = 0$ to the $v_{OH} = 1$ state, the hydrogen bond is initially in a non-equilibrium state. Subsequent relaxation of the hydrogen

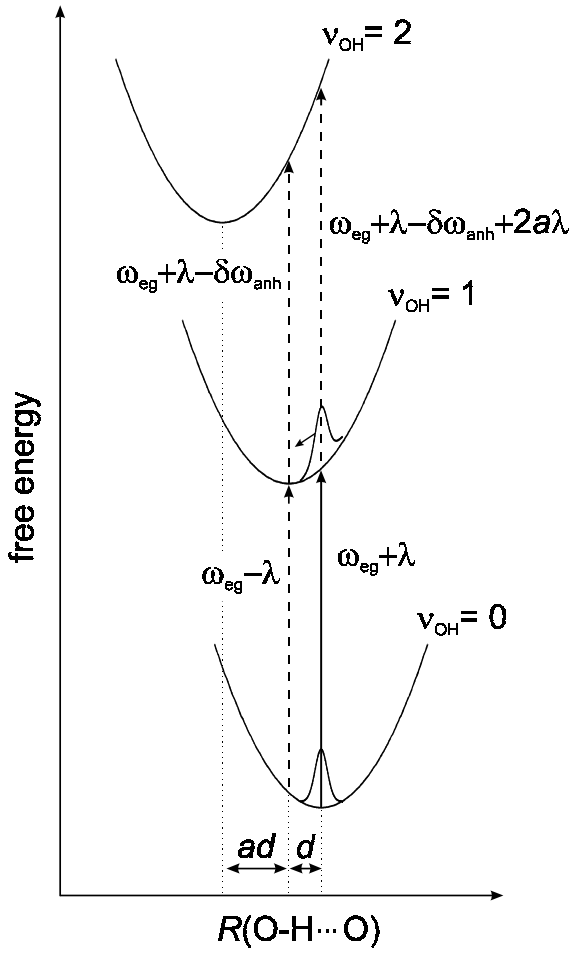

FIGURE 4.3. Schematic picture of the potential energy functions of the $\nu_{O-H\cdots O}$ mode in the $\nu_{OH} = 0$, $\nu_{OH} = 1$, and $\nu_{OH} = 2$ states. After excitation to the $\nu_{OH} = 1$ state, the hydrogen-bond experiences the $\nu_{OH} = 1$ potential. The minimum of this potential occurs at a smaller value of $R_{O-H\cdots O}$, and hence the hydrogen bond is initially in a non-equilibrium state. Subsequent relaxation leads to a redshift of the $\nu_{OH} = 0 \rightarrow 1$ frequency. The linear displacement of the $\nu_{OH} = 2$ potential with respect to the $\nu_{OH} = 1$ potential is a times that of the $\nu_{OH} = 1$ potential with respect to the $\nu_{OH} = 0$ potential.

bond to its new equilibrium position leads to a redshift of the $v_{OH} = 0 \rightarrow 1$ frequency of the excited molecule, and hence to a redshift of the 'particle' contribution to the bleaching. This relaxation corresponds to a contraction of the hydrogen bond. Simultaneously, the depletion in the $v_{OH} = 0$ state at the excitation frequency is gradually filled up due to the

modulation of $R_{O-H\cdots O}$ of the remaining molecules in the $v_{OH} = 0$ state, causing the 'hole' contribution to broaden towards the linear absorption band. The total bleaching signal is the sum of the 'particle' and 'hole' contribution, and therefore broadens mainly towards to the red side of the absorption band. In a previous theoretical study of the dynamics of the OH-stretch mode in HDO:D_2O, only the 'hole' contribution was taken into account, and hence only a broadening of the spectral hole towards the linear ν_{OH} absorption spectrum was predicted [78].

In a recent femtosecond study, it was found that the first spectral moment of the transient spectrum of the OH-stretch mode in HDO:D_2O does not shift to a Stokes-shifted value [31]. This result seems to be inconsistent with the fact that for liquid water ν_{OH} strongly depends on $R_{O-H\cdots O}$, since this dependence implies that the hydrogen-bond potentials of the $v_{OH} = 0$ and $v_{OH} = 1$ states must be displaced with respect to each other. This displacement will lead to a significant Stokes shift. However, it should be realized that the first moment is not only affected by the Stokes shift, but also by two other effects that shift the frequency of the first moment to a higher value. Firstly, the first spectral moment will be strongly influenced by the transient $v_{OH} = 1 \rightarrow 2$ absorption, which is redshifted by $\sim$270 cm^{-1} with respect to the $v_{OH} = 0 \rightarrow 1$ transition frequency [22]. This absorption is extremely broad (approximately 500 cm^{-1} [22]) and strongly overlaps with the red side of the $v_{OH} = 0 \rightarrow 1$ bleaching, leading to a significant blueshift of the first spectral moment. The strong effect of the $v_{OH} = 1 \rightarrow 2$ absorption can be seen from the delay scan with a probe frequency of 3330 cm^{-1} (Fig. 4.1), which shows a decrease of the transmission for small delay times due to this absorption. Secondly, the vibrational lifetime strongly decreases with decreasing ν_{OH} [79], which for longer delays also leads to a blueshift of the first spectral moment. Due to these effects, the frequency to which the first moment converges after spectral relaxation may even be above the maximum of the linear absorption spectrum. Therefore, the first spectral moment is a poor parameter to infer a dynamic Stokes shift. Fortunately, in spite of the above-mentioned effects, it is still possible to observe the dynamic Stokes shift, since it is the only effect that leads to stronger broadening of the bleaching to lower frequencies than to higher frequencies. This effect is clearly observed Figs. 1 and 2.

We describe our data quantitatively assuming that the hydrogen-bond is a Brownian oscillator coupled to the optically excited OH-stretch mode [35]. The Brownian oscillator model assumes harmonic potential energy functions for the low-frequency (hydrogen-bond) mode, which are linearly displaced by a distance d with respect to each other in the ground and first excited state of the optically excited (OH-stretch) mode (see Fig. 4.3). Because of the approximately Gaussian shape of the OH-stretch absorption band we assume that the hydrogen-bond mode is a strongly overdamped mode (SOM) [35]. The motion of the Brownian oscillator is then diffusive, and the dynamics can be described in terms of three parameters: Λ, the inverse of the correlation time of the diffusive motion, 2λ, the Stokes shift in units of angular frequency, and Δ, the linewidth parameter [35]. An explicit expression for the pump-probe signal S_{PP} in terms of Λ, λ, Δ, and the pulse parameters can be found in the literature (Eq. (13.32) of Ref. [35]). The $v_{OH} = 1 \rightarrow 2$ transition is

incorporated by adding an extra term to this expression:

$$S_{\mathrm{PP}}(\omega_1,\omega_2,\tau) = \frac{2\pi e^{-\tau/T_1}}{\sqrt{(\Delta^2+w_1^2)\alpha^2(\tau)}}\, e^{-(\omega_1-\omega_{\mathrm{eg}}^0-\lambda)^2/2(\Delta^2+w_1^2)} \times\{e^{-(\omega_2-\omega_e(\tau))^2/2\alpha(\tau)^2} + e^{-(\omega_2-\omega_{\mathrm{g}}(\tau))^2/2\alpha(\tau)^2} - \sigma_{\mathrm{ea}}\, e^{-(\omega_2-\omega_{\mathrm{ea}}(\tau))^2/2a^2\alpha(\tau)^2}\}, \tag{4.2}$$

with

$$\omega_e(\tau) = \omega_{\mathrm{eg}}^0 - \lambda + e^{-\Lambda\tau}(\omega_0 - \omega_{\mathrm{eg}}^0 + \lambda), \tag{4.3}$$

$$\omega_{\mathrm{g}}(\tau) = \omega_{\mathrm{eg}}^0 + \lambda + e^{-\Lambda\tau}(\omega_0 - \omega_{\mathrm{eg}}^0 - \lambda), \tag{4.4}$$

$$\omega_{\mathrm{ea}}(\tau) = \omega_{\mathrm{eg}}^0 + \lambda - \delta\omega_{\mathrm{anh}} + a\, e^{-\Lambda\tau}(\omega_0 - \omega_{\mathrm{eg}}^0 + \lambda), \tag{4.5}$$

$$\omega_0 = \omega_1 \frac{\Delta^2}{\Delta^2+w_1^2} + (\omega_{\mathrm{eg}}^0+\lambda)\frac{w_1^2}{\Delta^2+w_1^2}, \tag{4.6}$$

$$\alpha^2(\tau) = \Delta^2\left[1 - \frac{\Delta^2}{\Delta^2+w_1^2}\, e^{-2\Lambda\tau}\right] + w_2^2, \tag{4.7}$$

where ω_1, w_1 and ω_2, w_2 are the center frequency and spectral width of the pump and probe pulse, respectively, and $\omega_{\mathrm{eg}}^0+\lambda$ the center frequency of the absorption band. In Eq. (4.2), the first and second term in the braces correspond to the 'particle' and 'hole' contributions to the bleaching, which have delay-dependent center frequencies $\omega_{\mathrm{e}}(\tau)$ and $\omega_{\mathrm{g}}(\tau)$, respectively. The third term represents the excited-state absorption, with center frequency $\omega_{\mathrm{ea}}(\tau)$. The excited-state absorption is characterized by the $v_{\mathrm{OH}} = 1 \rightarrow 2$ cross section σ_{ea} (relative to the $v_{\mathrm{OH}} = 0 \rightarrow 1$ cross section), the anharmonicity $\delta\omega_{\mathrm{anh}}$, and the scale factor a for the displacement of the $v_{\mathrm{OH}} = 2$ potential (see Fig. 4.3). We added a factor $e^{-\tau/T_1}$ to account for the finite excited-state lifetime. We found better agreement between theory and data if a small homogeneous broadening (FWHM 33 cm^{-1}) in addition to the broadening caused by the Brownian oscillator was assumed. Convolution of the result of equation (2) with the experimentally determined cross-correlation trace (Figs. 4.1(b) and 4.2(b)) yields theoretical pump-probe delay scans. To describe the data, the spectral widths and center frequencies of pump and probe were determined from least-squares fits to the power spectra (Figs. 4.1(c) and 4.2(c)). We used $\delta\omega_{\mathrm{anh}} = 270$ cm^{-1} [22], a relative excited-state cross section of $\sigma_{\mathrm{ea}} = 1.54$, and a scale factor of $a = 2$. This value for a implies that the $v_{\mathrm{OH}} = 2$ potential is displaced significantly more with respect to the $v_{\mathrm{OH}} = 1$ potential than the $v_{\mathrm{OH}} = 1$ with respect to the $v_{\mathrm{OH}} = 0$ potential, in agreement with the experimentally observed very broad $v_{\mathrm{OH}} = 1 \rightarrow 2$ and $v_{\mathrm{OH}} = 0 \rightarrow 2$ absorption bands [22, 80]. With $T_1 = 650$ fs, $\Lambda = 2$ THz, $\lambda = 7$ THz, and $\Delta = 19$ THz, we found good agreement (Fig. 4.4(a)). With the same parameter values we could also describe the linear absorption spectrum (Fig. 4.4(b)). The value for λ corresponds to a Stokes shift of 74 cm^{-1}, which is in quite good agreement with the Stokes shift of 60 cm^{-1} obtained from equation (4.1) using the linewidth of 260 cm^{-1} of the ν_{OH} band of HDO:$\mathrm{D_2O}$ as input. The value of 2 THz for Λ corresponds to a correlation time of 500 fs for the diffusive motion of the hydrogen bond.

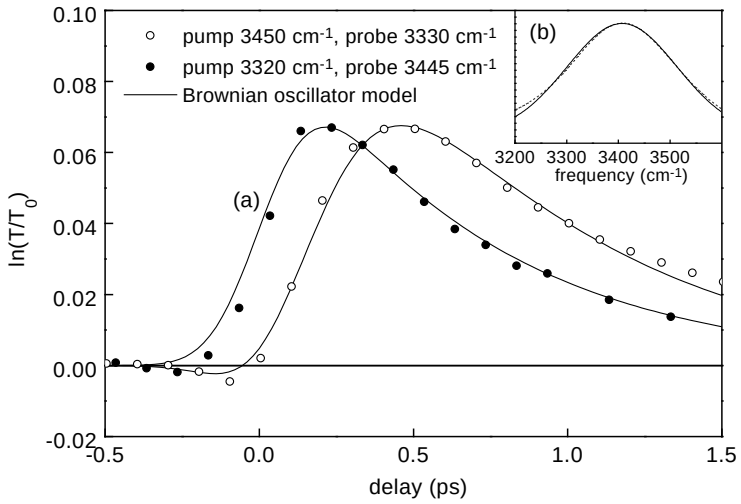

FIGURE 4.4. (a) Experimental pump-probe delay scans (points), and delay scans calculated using the Brownian oscillator model (solid curves). (b) Experimental OH-stretch absorption spectrum (dashed curve) and the absorption spectrum calculated using the Brownian oscillator model (solid curve).

It is clear that the Brownian oscillator model provides a quantitative description of the observed broadening of the bleaching signal towards lower frequencies. Interestingly, this redshift results both from the Stokes shift of the stimulated emission of the $v_{\mathrm{OH}} = 1 \rightarrow 0$ transition and from the Stokes shift of the $v_{\mathrm{OH}} = 1 \rightarrow 2$ induced absorption, that is a times as large. The fact that $T_1 = 650$ fs instead of 740 fs leads to a better description of our data suggests that the Brownian oscillator model does not accurately describe the spectral relaxation for large delay times. This is probably due to the assumption of harmonic potentials [11]. In fact, the hydrogen-bond potential is probably strongly anharmonic [77, 81], and the hydrogen-bond potentials in the $v_{\mathrm{OH}} = 0$ and $v_{\mathrm{OH}} = 1$ states may have different shapes [53]. Both of these effects will lead to more complicated spectral dynamics.

4.4 Conclusion

In conclusion, we have observed evidence for a transient Stokes shift of a molecular vibrational transition. In water, the coupling between the OH-stretch and hydrogen-bond mode is particularly strong, leading to a large difference between the potential energy functions of the hydrogen bond in the $v_{\mathrm{OH}} = 0$ and $v_{\mathrm{OH}} = 1$ states. As a consequence, for water the vibrational Stokes shift is very pronounced. Similar effects can be expected for any other optically excited vibration that is coupled to a low-frequency mode. Hence, this effect should be considered in any study on spectral relaxation of a vibrational transition.

5 Orientational dynamics in liquid water

5.1 Introduction

Knowledge about the orientational dynamics of water is essential for understanding the (bio)chemical and physical processes that take place in this liquid, notably chemical reactions and solvation. Therefore, the reorientational motion of molecules in liquid water has been extensively studied for over half a century, in particular by such methods as dielectric relaxation [82, 83], THz spectroscopy [84, 85], optical and Raman-induced Kerr-effect spectroscopy [86, 87], and nuclear magnetic resonance [61]. However, all of the experimental techniques employed to date probed the orientational motion indirectly or averaged over all molecules in the liquid. In addition, it is often not clear to what kind of molecular motion the relaxation observed with these methods is related. In contrast, polarization-resolved pump-probe spectroscopy yields unambiguous information about the dynamics of orientational relaxation of small molecules in the liquid phase [55, 88]. In this Chapter, we apply this technique to the OH-stretch mode of dilute solution of HDO in D_2O. In this way, we can directly study the orientational motion of OH groups of the HDO molecules. The frequency tunability of the infrared pulses makes it possible to study specific subensembles of the water molecules.

5.2 Experiment

Mid-infrared pulses are generated with the setup described in Section 2.4.1. In the pump-probe experiments, the infrared pulses are split into an intense pump pulse ($\sim$20 μJ) that excites a significant fraction of the HDO molecules, and a weak probe pulse ($\sim$1 μJ) that monitors the induced relative transmission change $\ln(T/T_0)$ as a function of the delay τ between the pump and probe pulses, where T_0 denotes the equilibrium probe transmission (no pump pulse). Autocorrelation traces of the pulses are obtained by second-harmonic generation in a 3 mm thick $LiIO_3$ crystal.

The sample is 200 μm thick and contains 1 mol/l solution of HDO in D_2O, prepared by mixing appropriate amounts of H_2O (HPLC grade) and D_2O (>99.9 atom% D). During the measurements the water is rapidly circulated to ensure that for every laser shot there is a fresh part of the liquid in the focus.

5.3 Results

We have recorded pump-probe scans at excitation frequencies of 3320, 3400 and 3500 cm^{-1}. The power spectra of the pulses at those frequencies are shown in Fig. 5.1, together with the infrared absorption spectrum of the sample in the OH-stretch region,

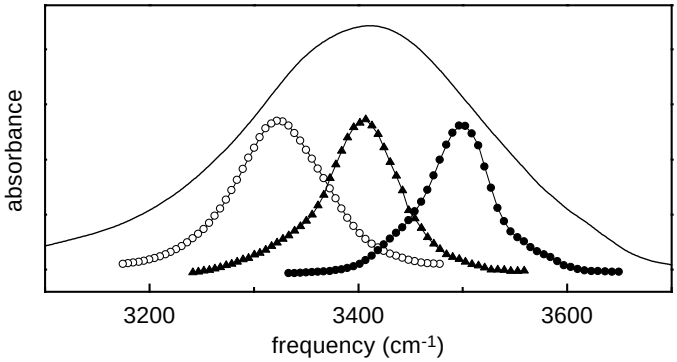

FIGURE 5.1. Infrared absorption spectrum of the OH-stretch mode of HDO in D_2O (1 mol/l in 200 μm), corrected for the D_2O background absorption (black curve), and normalized power spectra of the laser pulses, centered at 3320 (open points), 3400 (triangles) and 3500 cm^{-1}(solid points), respectively.

measured using a conventional infrared spectrometer. The intensity of the pump pulse is sufficient to excite a significant fraction of the HDO molecules to the $v_{OH} = 1$ state. Due to the large anharmonicity of the v_{OH} mode (270 cm^{-1} [22]), these molecules no longer absorb the probe pulse. This results in a transmission increase of the probe pulse for positive delays. The decay of the relative transmission changes $\ln(T/T_0)_{\parallel,\perp}$ of the probe pulse is determined by both vibrational relaxation of the molecules in the $v_{OH} = 1$ state and the spectral and orientational relaxation of the molecules in the $v_{OH} = 0$ and $v_{OH} = 1$ states.

In order to study the orientational relaxation of the excited molecules, we use the method described in Section 2.5: the polarization of the probe pulse is rotated 45° with respect to that of the pump pulse using a zero-order $\lambda/2$-plate, and the transmission changes $\ln(T/T_0)$ of the components of the probe pulse polarized parallel and perpendicular to the pump pulse are monitored by means of a polarizer placed behind the sample. If the pump field is polarized along the *z*-axis, the $v_{OH} = 0 \rightarrow 1$ transition probability of a HDO molecule is proportional to $\cos^2\theta$, where θ is the angle between the molecular transition dipole moment (directed along the OH-bond) and the *z*-axis. Since at thermal equilibrium the molecular transition dipole moments are randomly oriented, the excitation by the pump field results in an orientational distribution of the OH-bonds of the excited molecules given by $f(\theta) = \frac{3}{4\pi}\cos^2\theta$. As a consequence, initially the transmission change for the probe pulse component parallel to the pump field ($\ln(T/T_0)_{\parallel}$) is three times larger than for the perpendicular component ($\ln(T/T_0)_{\perp}$) [55]. As rotational reorientation of the molecules takes place, the difference between the $\ln(T/T_0)_{\parallel}$ and $\ln(T/T_0)_{\perp}$ components decreases, and in the limit of complete orientational scrambling vanishes ($f(\theta) \rightarrow \frac{1}{4\pi}$).

Fig. 5.2 shows the results obtained by pumping at 3400 cm^{-1}, at the center of the ν_{OH} absorption band, for the parallel ($\parallel$) and perpendicular ($\perp$) components of the probe pulse. Vibrational relaxation leads to a population transfer from the $v_{OH} = 1$ to the $v_{OH} = 0$ state and thus to a decrease of the bleaching for both polarization components of the probe pulse, but does not change the ratio $[\ln(T/T_0)_{\parallel}/\ln(T/T_0)_{\perp}]$. It is easily shown that the rotation-free signal $\Delta\alpha_{RF}(\tau)$, which is defined as [55]

$$-\Delta\alpha_{RF}(\tau) = \ln(T(\tau)/T_0)_{\parallel} + 2\ln(T(\tau)/T_0)_{\perp}, \tag{5.1}$$

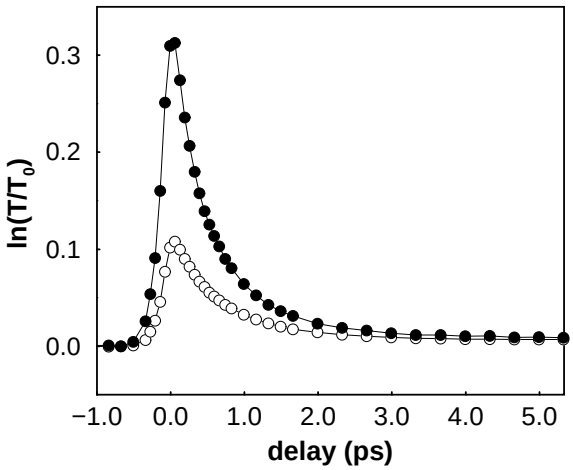

FIGURE 5.2. Pump-probe scans recorded pumping and probing at an excitation frequency of 3400 cm^{-1} (pulse spectrum shown as the triangles in Figure 5.1). The relative transmission change $\ln(T/T_0)_{\parallel,\perp}$ of the probe pulse is plotted versus the delay τ, for the components polarized parallel (solid points) and perpendicular (open points) to the pump pulse.

reflects only the excited-state population dynamics, whereas the rotational anisotropy $R(\tau)$, which is defined as [55]

$$R(\tau) = \frac{\ln(T(\tau)/T_0)_{\parallel} - \ln(T(\tau)/T_0)_{\perp}}{\ln(T(\tau)/T_0)_{\parallel} + 2\ln(T(\tau)/T_0)_{\perp}}, \tag{5.2}$$

reflects only the orientational dynamics (independent of the vibrational relaxation), with a value between 0 (complete orientational scrambling) and 0.4 (maximal anisotropy).

Fig. 5.3 shows the observed rotational anisotropy as a function of delay, for three excitation frequencies within the ν_{OH} absorption band. The power spectra are shown in Fig. 5.1 (the point styles of Figs. 5.1 and 5.3 match). The orientational dynamics clearly depend dramatically on the excitation frequency. At the high frequency side of the absorption band (solid points) the decay of the rotational anisotropy occurs much faster than at the low frequency side (open points), where it remains nearly constant. Since the OH-stretch frequency ν_{OH} decreases with increasing hydrogen-bond strength (see Section 1.2), our results imply that the orientational relaxation takes place much faster for weakly hydrogen-bonded molecules (high ν_{OH} frequency) than for strongly hydrogen-bonded molecules (low ν_{OH} frequency), which apparently remain more or less fixed in their environment. Surprisingly, at the center frequency (triangles) and the high-frequency side (solid points) of the absorption band, the decay occurs in a non-exponential manner. For small delays the decay is very fast, for large delays the rotational anisotropy decays much slower.

5.4 Discussion

In order to rotate and change its angle with respect to the polarization of the pump pulse, an OH group must break its hydrogen bond. Such a process will cost more energy for strongly hydrogen-bonded OH groups than for weakly hydrogen-bonded groups. This explains

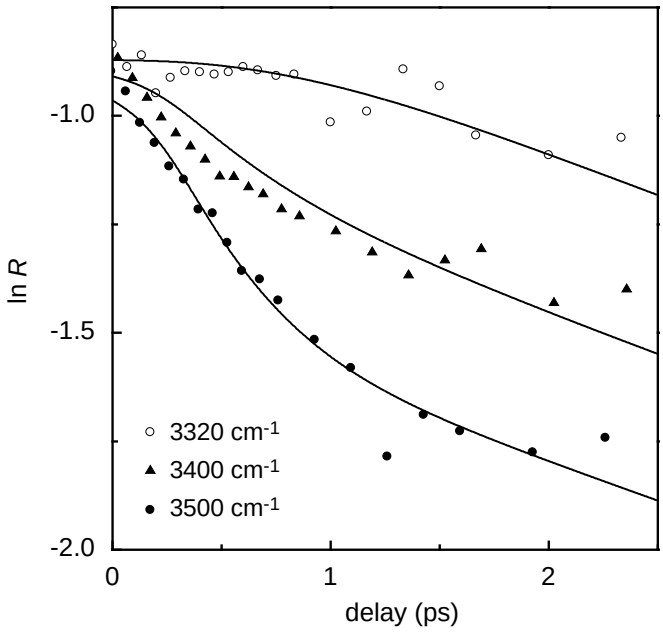

FIGURE 5.3. Logarithm of the rotational anisotropy as a function of the delay between the exciting and probing pulse, at three excitation frequencies within the ν_{OH} absorption band of water. The point styles of the data and the power spectra shown in Fig. 5.1 match. The curves represent decays calculated using the model described in the text.

why the orientational relaxation takes place much more slowly at low than at high ν_{OH} frequencies. In order to quantitatively describe this effect, we assume that the orientational relaxation is a thermally activated process. The activation energy $E_A(\nu_{OH})$ of this process, which will be on the order of the hydrogen-bond dissociation energy of 2000 cm^{-1} [47], is assumed to increase linearly with decreasing ν_{OH} (increasing hydrogen-bond strength). This leads to a frequency dependent decay constant of the rotational anisotropy:

$$\tau_R(\nu_{OH}) = C\, e^{E_A(\nu_{OH})/k_B T} + \tau_R^0. \tag{5.3}$$

We have added a constant τ_R^0 in the above expression to account for the fact that even for very weakly hydrogen-bonded OH groups, the orientational relaxation rate should still have a finite value, determined by the moment of inertia of the HDO molecule and steric effects.

In a quantitative description of the decay of the rotational anisotropy, we must take account of the spectral relaxation of the ν_{OH} excitation, which takes place on a time scale of approximately 500 fs (see Chapter 4). To do this, we use the Brownian oscillator model, which was described in Chapter 4. When τ_R is frequency dependent, it is difficult to obtain explicit expressions for the decay of the rotational anisotropy of an optically excited mode coupled to a Brownian oscillator. Fortunately, for a strongly overdamped mode, the Brownian oscillator model is equivalent to a spectral diffusion model [35], in which the $\nu_{OH} = 0 \rightarrow 1$ frequency of a molecule in the $\nu_{OH} = 0$ state is given by

$$\omega_{01}(t) = \omega_{eg}^0 + \lambda + \delta\omega_{01}(t), \tag{5.4}$$

where the detuning $\delta\omega_{01}(t)$ is a Gauss-Markov random process, with a correlation function [35]

$$\langle \delta\omega_{01}(t)\delta\omega_{01}(0)\rangle = \Delta^2 e^{-\Lambda t}. \tag{5.5}$$

Similarly, the $\nu_{\mathrm{OH}} = 1 \rightarrow 0$ transition frequency of a molecule in the $\nu_{\mathrm{OH}} = 1$ state is given by

$$\omega_{10}(t) = \omega_{\mathrm{eg}}^0 - \lambda + \delta\omega_{10}(t), \tag{5.6}$$

with

$$\langle \delta\omega_{10}(t)\delta\omega_{10}(0)\rangle = \Delta^2 e^{-\Lambda t}. \tag{5.7}$$

In Eqs. (5.5) and (5.7), Δ is the linewidth parameter and Λ the inverse spectral relaxation time constant, both of which are defined in Chapter 4. This spectral diffusion process can be implemented numerically, which allows us to calculate the decay of the rotational anisotropy.

The initial spectral distribution of the 'particle' ($\nu_{\mathrm{OH}} = 1 \rightarrow 0$) and 'hole' ($\nu_{\mathrm{OH}} = 0 \rightarrow 1$) contributions to the bleaching is given by a convolution of the power spectrum of the pump pulse with the homogeneous linewidth of 33 cm^{-1}(see Chapter 4). The spectral diffusion causes the spectral distribution of the 'hole' to broaden towards the linear absorption spectrum, and that of the 'particle' towards the linear absorption spectrum Stokes-shifted by 2λ (see Chapter 4). The spectral distributions of the 'particle' and 'hole' contributions were calculated as a function of time by numerical integration of the equations for the spectral diffusion. After each time step, the decay of the rotational anisotropy $R(\omega)$ in each frequency bin was evaluated using Eq. (5.3). The observed rotational anisotropy is obtained by integrating the product of $R(\omega)$ and the power spectrum of the probe pulse over ω. In the calculation, the values for Δ, Λ, and λ obtained in Chapter 4 were used. We used Gaussian pulse envelopes for the pump and probe pulses, the width of which was obtained from autocorrelation traces recorded after each of the scans shown in Fig. 5.3.

We found good agreement between the calculated anisotropy and our data at all excitation frequencies using the parameter values $\tau_R^0 = 0.7$ ps, $C = 0.08$ fs and $E_{\mathrm{A}} = 9.6(3670 - \nu_{\mathrm{OH}})$ cm^{-1} (see Fig. 5.3). The decay constant $\tau_R(\nu_{\mathrm{OH}})$ for these parameter values, calculated using Eq. (5.3), is shown in Fig. 5.4. Clearly, it exhibits a dramatic frequency dependence. In fact, the water molecules may be divided in a fraction that is strongly hydrogen-bonded (low ν_{OH} frequency), and that exhibits virtually no orientational relaxation, and a fraction that is weakly hydrogen-bonded (high ν_{OH} frequency), and that shows orientational relaxation with a time constant of approximately τ_R^0. Thus, with regard to the orientational dynamics, our measurements suggest a two-component model for liquid water. The fact that the orientational anisotropy still shows a decay at the lowest probe frequency of 3320 cm^{-1}(see Fig. 5.3) even though the orientational relaxation rate at that frequency is practically zero (see Fig. 5.4), is caused by the spectral diffusion, which causes exchange between the OH-groups with high and low ν_{OH} frequencies. Orientational relaxation of an OH-group with a high ν_{OH} frequency (short $\tau_R(\nu_{\mathrm{OH}})$) and a subsequent change of its ν_{OH} frequency to a low value (due to spectral diffusion) will contribute to the decay of the rotational anisotropy at this low ν_{OH} frequency. This leads to an effective decay of the rotational anisotropy at low ν_{OH} frequency that is much faster than would be expected from the value of $\tau_R(\nu_{\mathrm{OH}})$ at that frequency.

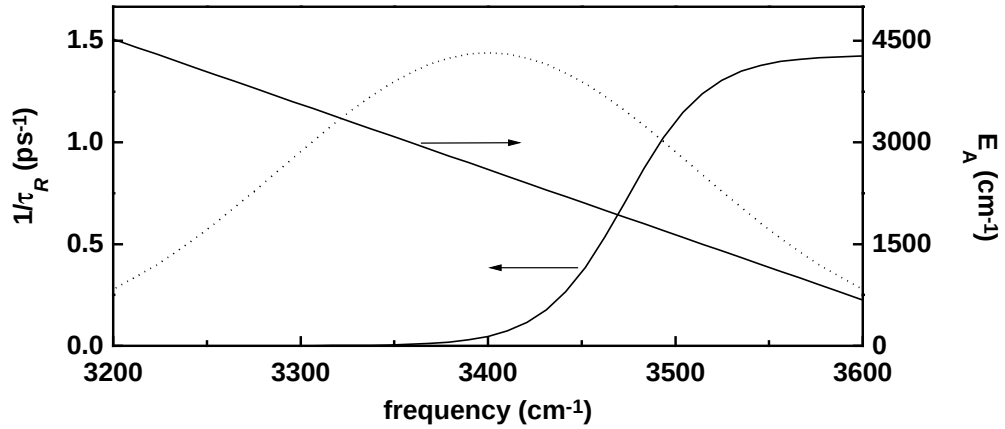

FIGURE 5.4. Frequency dependence of the activation energy $E_{\mathrm{A}}(\nu_{\mathrm{OH}})$ and the decay constant $\tau_R(\nu_{\mathrm{OH}})$. The dotted curve shows the Gaussian ν_{OH} absorption band used in the calculation.

It is interesting to compare the results presented in this Chapter to dielectric relaxation and THz studies on liquid water. In these experiments, one measures the complex dielectric function $\varepsilon(\omega)$ at low frequencies (GHz and THz regime). The dielectric function is related to the relaxation of the electric polarization as follows [89]:

$$\varepsilon(\omega) = \varepsilon_\infty + \int_0^\infty dt\, e^{i\omega t}\phi(t), \tag{5.8}$$

where the relaxation function $\phi(t)$ is the decay of the electric polarization $\mathbf{P}$ that would be observed upon instantaneous switching off of a constant electric field applied to the system until time $t = 0$ [89]. Usually, the relaxation function $\phi(t)$ is assumed to be a sum of exponentially decaying functions $\exp(-t/\tau_{D,j})$, which results in the well-known Debye-type dielectric function [83, 89]:

$$\varepsilon(\omega) = \varepsilon_\infty + \sum_j \frac{c_j}{1 - i\omega\tau_{D,j}}, \tag{5.9}$$

where c_j are constants, and $\tau_{D,j}$ are referred to as Debye relaxation times. In dielectric relaxation and THz experiments, the orientational relaxation in water has often been observed to occur on two time scales. The slow time scale has an associated Debye relaxation time of $\tau_{D,1} \approx 8$ ps [83, 85, 90], whereas the values reported for the Debye constant associated with the fast time scale vary from $\tau_{D,2} < 200$ fs to $\tau_{D,2} = 1.02$ ps [83, 85, 90]. The difficulty in obtaining an accurate value for $\tau_{D,2}$ is due to the fact that the contribution of the fast process to the dielectric function is very small compared to that of the slow process.

We can use our model for $\tau_R(\nu_{\mathrm{OH}})$ to calculate the relaxation function $\phi(t)$ of the electric polarization, which describes the dielectric function through Eq. (5.8). It can be shown that for an ensemble of dipoles that exhibit orientational diffusion [89], the Debye constant τ_D and the decay constant τ_R of the rotational anisotropy are related by $\tau_D = 3\tau_R$ (see the Appendix). Our model therefore implies a Debye constant that depends on ν_{OH}. That is, each subensemble of water molecules with a specific ν_{OH} frequency

(and hence, a specific hydrogen-bond strength) exhibits orientational diffusion with an associated Debye constant given by $\tau_D(\nu_{OH}) = 3\tau_R(\nu_{OH})$, where $\tau_R(\nu_{OH})$ is determined by Eq. (5.3). The total electric polarization is the sum of the electric polarizations of each of the subensembles. It should be noted that the decay of the total electric polarization is determined not only by $\tau_D(\nu_{OH})$, but also by the spectral diffusion, which causes exchange between the subensembles with high and low $\tau_D(\nu_{OH})$. This leads to a faster decay of the electric polarization than would be observed in absence of spectral diffusion, since the subensembles with long $\tau_D(\nu_{OH})$ will have a faster effective decay route for reorientation through spectral exchange with subensembles with short $\tau_D(\nu_{OH})$.

To calculate the relaxation function $\phi(t)$ of the total electric polarization, we assume that at $t = 0$ the electric polarizations of all subensembles are equal, and that all molecules are in the $v_{OH} = 0$ state. The decay of each subensemble is calculated by numerical integration, in which we take the spectral diffusion in the $v_{OH} = 0$ state (described by Eqs. (5.4) and (5.5)) and the decay of the electric polarization (described by $\tau_D(\nu_{OH})$) of each subensemble into account. The total electric polarization is evaluated at each time step by adding the electric polarizations of each of the subensembles, weighted by the distribution of ν_{OH} frequencies, which we assume to be given by the ν_{OH} absorption band (shown as the dotted curve in Fig. 5.4).

The calculated relaxation function $\phi(t)$ of the electric polarization is shown in Fig. 5.5(a). After an initial fast decay, $\phi(t)$ becomes exponential with a decay constant of 7.1 ps. The relaxation function can be well described with a biexponential decay with time constants of 7.1 ps and 0.3 ps (see Fig. 5.5(a)), which implies a dielectric function of the form (5.9) with $\tau_{D,1} = 7.1$ ps and $\tau_{D,2} = 0.3$ ps. The decay constant of 7.1 ps agrees well with the Debye constant of approximately 8 ps often observed in THz and dielectric relaxation studies on liquid water. The slight discrepancy between the two values might be due to the fact that τ_R, which was used to calculate $\phi(t)$, describes the orientational relaxation of the ν_{OH} transition dipole moment of HDO, whereas τ_D describes the orientational relaxation of the permanent dipole moment of the water molecule, or to the different moments of inertia of HDO and H_2O. The decay constant of 0.3 ps corresponds to the fast time constant $\tau_{D,2}$ observed in dielectric relaxation, THz, and Kerr-effect measurements. This fast part of the decay is determined by both the orientational and spectral relaxation. It is clear from Fig. 5.5(a) that the contribution of this fast process to the dielectric function is very small.

Note that both the dielectric relaxation measurements and the polarization-resolved pump-probe experiments show that the orientational relaxation takes place on two distinct time scales. However, that these two time scales are associated with different hydrogen-bond strengths can only be shown with pump-probe spectroscopy, which allows us to selectively study subensembles with a specific hydrogen-bond strength (ν_{OH} frequency). This information could not have been obtained with linear techniques such as dielectric relaxation and THz experiments, which inherently measure an average over all molecules in the liquid.

Fig. 5.5(b) shows the frequency-dependent part of the complex dielectric function $\varepsilon(\omega)$, obtained from the calculated $\phi(t)$ using Eq. (5.8). The calculation agrees well with the experimentally observed dielectric function, as presented in for example Ref. [83],

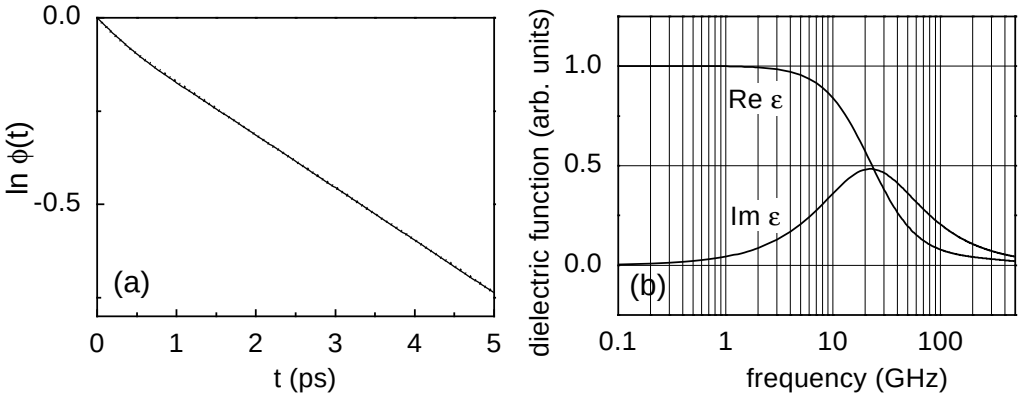

FIGURE 5.5. (a) The solid curve represents the logarithm of the calculated relaxation function $\phi(t)$ for the electric polarization. The dotted curve is a biexponential decay with time constants of 0.3 and 7.1 ps. (b) Real and imaginary part of the frequency-dependent part of the dielectric function, calculated from $\phi(t)$ using Eq. (5.8).

and we can conclude that both the polarization-resolved pump-probe experiments and the dielectric relaxation measurements can be well described with the model for the orientational relaxation in liquid water presented here.

5.5 Conclusion

In this Chapter, we have studied the orientational relaxation of frequency-selected molecules in liquid water. It is found that the orientational relaxation takes place on two distinct time scales: weakly hydrogen-bonded molecules show rapid orientational relaxation with a decay constant on the order of $\tau_R^0 = 0.7$ ps, whereas strongly hydrogen-bonded molecules retain their orientation for a much longer period of time. These results suggest that a mixture model applies to liquid water, and that with respect to the orientational dynamics two molecular species exist in the liquid. The model for the orientational relaxation proposed in this Chapter also gives a good quantitative description of the complex dielectric function of liquid water.

Appendix: Relation between τ_R and the Debye relaxation time τ_D

Let $f(\theta,\phi,t)$ be the distribution of orientations (θ,ϕ) of an ensemble of dipoles at time t. If the dipoles undergo Brownian rotational motion, it can be shown that in absence of external fields the orientational distribution function satisfies the equation [89]:

$$\frac{\partial f(\theta,\phi,t)}{\partial t} = \frac{1}{2\tau_D}\left\{\frac{1}{\sin\theta}\frac{\partial}{\partial\theta}\left[\sin\theta\frac{\partial f(\theta,\phi,t)}{\partial\theta}\right] + \frac{1}{\sin^2\theta}\frac{\partial^2 f(\theta,\phi,t)}{\partial\phi^2}\right\}, \tag{5.10}$$

where τ_D is the Debye relaxation constant, which contributes to the dielectric function of the system in the form [89]

$$\frac{\varepsilon_s - \varepsilon_\infty}{1 - i\omega\tau_D}. \tag{5.11}$$

We use Eq. (5.10) to calculate the decay of the rotational anisotropy R of the dipoles in case the initial distribution is given by

$$f(\theta,\phi,0) = \frac{3}{4\pi}\cos^2\theta. \tag{5.12}$$

The solution of Eq. (5.10) is then found to be

$$f(\theta,\phi,t) = \frac{1}{4\pi}\left[(3\cos^2\theta - 1)e^{-3t/\tau_D} + 1\right]. \tag{5.13}$$

The rotational anisotropy is the difference between $\cos^2\theta$ and $\cos^2\phi\sin^2\theta$ weighted with the distribution $f(\theta,\phi,t)$:

$$R(t) = \frac{\int\int d\Omega\,(\cos^2\theta - \cos^2\phi\sin^2\theta)\,f(\theta,\phi,t)}{\int\int d\Omega\,(\cos^2\theta + 2\cos^2\phi\sin^2\theta)\,f(\theta,\phi,t)} = (2/5)e^{-3t/\tau_D}. \tag{5.14}$$

We see that the decay constant of the rotational anisotropy is given by $\tau_R = \tau_D/3$.

6 Anomalous temperature dependence of vibrational lifetimes in water and ice

6.1 Introduction

Many physical properties of water exhibit a remarkable temperature dependence. The best known example is probably the density, which is larger in the liquid than in the solid phase. Other examples include the viscosity, the specific heat, and the static dielectric constant, all of which show temperature dependences that differ significantly from what is generally observed in liquids. In many cases the anomalous temperature dependence of these properties has provided fundamental information on the dynamics and structure of water.

A better understanding of the physical properties of liquids can be obtained by studying the dynamics of the elastic and inelastic microscopic molecular interactions. Information on the inelastic molecular interactions can in turn be obtained by measuring the lifetime of molecular vibrations. Of special interest in this respect is the measurement of the vibrational lifetime as a function of temperature, since in many cases this allows the identification of the modes to which the energy of the excited mode is transferred. In most theories for vibrational relaxation [91–93] the vibrational lifetime strongly decreases with temperature, in most cases as a result of the increased occupation of the energy-accepting modes. Measuring the temperature dependence of the lifetime allows the determination of the frequencies of these modes and thus may help in their identification. It is clear that measuring the lifetime of a vibration of the water molecule as a function of temperature might provide us with new insights in the microscopic molecular couplings in water, which eventually may lead to a better understanding of the anomalous macroscopic properties of this liquid. The OH-stretching mode of water is obviously the most suitable candidate, as it is a very sensitive probe for the hydrogen-bond structure [13]. Unfortunately, the time resolution in previous time-resolved mid-infrared studies on ice and water was not sufficient to accurately determine the OH-stretching lifetimes [22, 23, 94, 95]. In this Chapter, we report on the determination of OH-stretching lifetime and its temperature dependence in dilute HDO:D_2O solution, both in the liquid and solid (ice I*h*) phase.

6.2 Experiment

For the pump-probe experiments, we use the two-color setup described in Section 2.4.2. The pump and probe pulses are focused to a spot with a diameter of $\sim$300 μm and have spatial overlap in the sample. The pump pulse is tuned to the $\nu_{OH} = 0 \rightarrow 1$ frequency, and the probe pulse to either the $\nu_{OH} = 0 \rightarrow 1$ or the $\nu_{OH} = 1 \rightarrow 2$ frequency. The pump pulse

induces a significant population of the $\nu_{OH} = 1$ level, which is monitored by the probe pulse. By measuring the excited state ($\nu_{OH} = 1 \rightarrow 2$) absorption as a function of delay between the pump and probe pulses, we determine the vibrational lifetime T_1. The probe polarization was at the magic angle with respect to the pump polarization, ensuring that the observed transients are determined by the vibrational relaxation only [55].

The sample consisted of a 500 μm layer of dilute ($\sim$1:500) solution of HDO in D_2O kept between two sapphire windows, and was mounted on the cold finger of a closed-cycle He cryostat equipped with a heater. This enabled us to continuously tune the temperature of the sample from 30 to 363 K with an accuracy of 0.2 K. The ice was prepared by slowly cooling down sample until solidification occurred, typically at $\sim$265 K. Since the sample cannot be circulated, we had to lower the pump pulse repetition rate to 70 Hz to avoid heating of the sample in the focus. Using the differential equation for diffusion of heat and the thermophysical properties of D_2O, an upper bound can be obtained for the steady-state heating in the focus, which is 2.6 K for water and 1 K for ice (see the Appendix at the end of this Chapter). These values represent the uncertainty in the reported temperature values.

6.3 Results

6.3.1 General considerations

It has been shown recently that in inhomogeneously broadened bands of hydrogen-bonded OH groups the vibrational lifetime can be strongly dependent on the excitation frequency [79, 96]. In addition, there can be spectral relaxation effects [23, 97]. To investigate if such effects occur, we have recorded pump-probe scans in liquid water at room temperature, with a fixed pump frequency of 3500 cm^{-1}, which is at the high-frequency side of the ν_{OH} band, and three different probe frequencies within the broad $\nu_{OH} = 0 \rightarrow 1$ band (Fig. 6.1). If the probe pulse is tuned to the same frequency as the pump, the decay rate of the bleaching is initially larger than the value approached for large delays, which is clearly suggestive of spectral relaxation [88]: the spectral relaxation of the excited OH groups out of the spectral window of the probe pulse gives rise to an extra contribution to the decay of the bleaching, which adds to that of the vibrational relaxation. At probe frequencies away from the pump frequency, the decay rate is initially slower due to spectral relaxation of the excited OH groups into the spectral window of the probe, a process that competes with the vibrational relaxation. The spectral relaxation also causes the bleaching at these frequencies to rise to a maximum at larger delay values than at the pump frequency. After approximately 1 ps, the decay rate has become equal at all probing frequencies, indicating that no more spectral relaxation takes place (see also Chapter 4).

6.3.2 Vibrational lifetimes

Typical pump-probe scans recorded in ice and in water, showing the excited state ($\nu_{OH} = 1 \rightarrow 2$) absorption vs. the delay between pump and probe, are presented in Fig. 6.2. These scans show that in water at 353 K the vibrational lifetime is significantly *longer* than

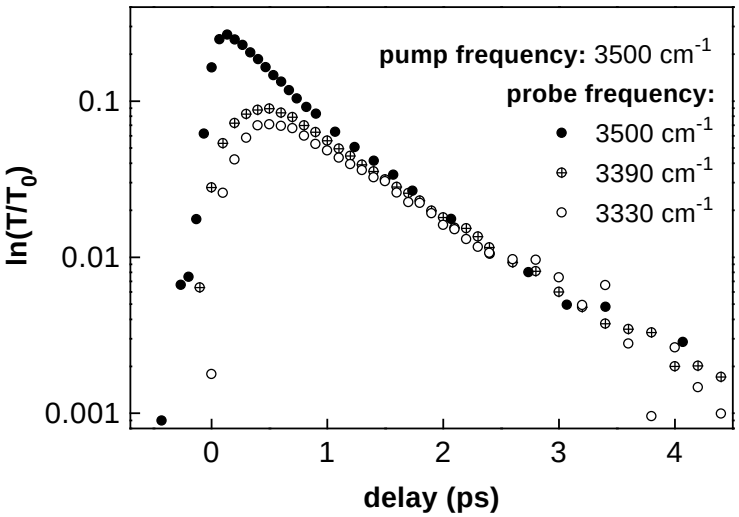

FIGURE 6.1. Pump-probe scans recorded in dilute HDO:D_2O at room temperature, showing the transmission change $\ln(T/T_0)$ of the probe pulse as a function of the delay between pump and probe, at three different $\nu_{OH} = 0 \rightarrow 1$ probing frequencies and with $\nu_{pump} = 3500$ cm^{-1}.

at 298 K, in striking contrast with the generally observed decrease of excited-state lifetimes with temperature, both for vibrational [98–101] and electronic [102–104] transitions. Fig. 6.2 also shows that the vibrational relaxation takes place approximately *twice as fast* in ice as in water.

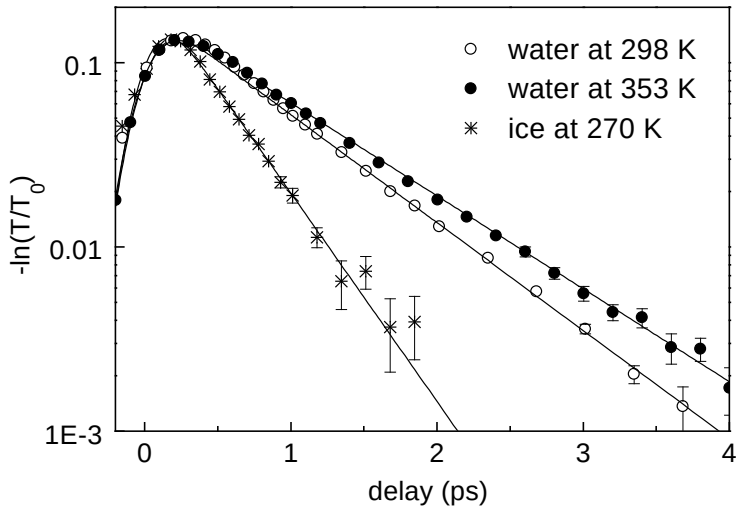

FIGURE 6.2. Pump-probe scans recorded in HDO:D_2O in the liquid (ν_{pu} = 3400 cm^{-1}, ν_{pr} = 3150 cm^{-1}) and solid phase (ν_{pu} = 3330 cm^{-1}, ν_{pr} = 3090 cm^{-1}), showing the absorption increase at the probe frequency vs. the delay between the pump and probe pulses. The drawn curves are convolutions of a Gaussian with mono-exponential decays with time-constants of 740 fs (298 K), 861 fs (353 K), and 385 fs (270 K), respectively.

We have recorded pump-probe scans in a broad range of temperatures, keeping the pump frequency fixed at 3400 cm^{-1} for water and 3330 cm^{-1} for ice (the center frequencies of the ν_{OH} band at room temperature and 260 K, respectively). The probe was always

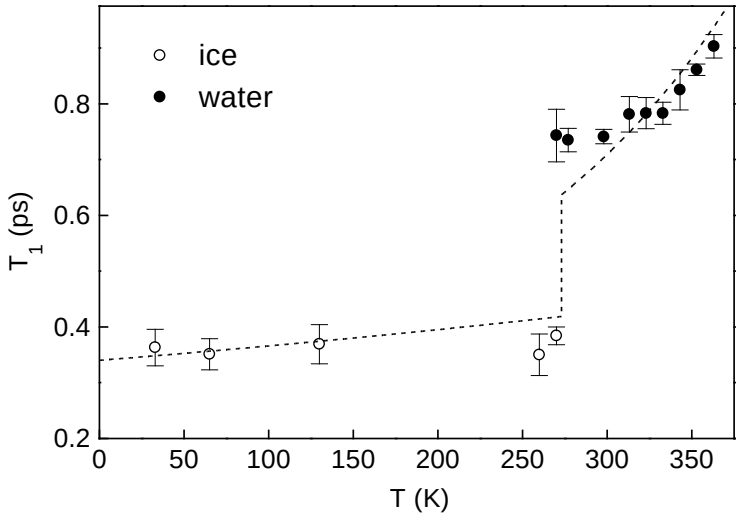

FIGURE 6.3. Vibrational lifetime T_1 of the OH-stretching mode of dilute HDO:D_2O as a function of temperature. Note that the lifetime at $T = 270$ K has been measured both in the solid and (undercooled) liquid phase. The dashed curve has been calculated using a power-law dependence of T_1 on the hydrogen-bond induced redshift of the OH-stretch frequency: $T_1 \propto (\delta\nu_{OH})^{-1.8}$ [53].

tuned to the $\nu_{OH} = 1 \rightarrow 2$ frequency (3150 cm^{-1} for water, 3090 cm^{-1} for ice). By fitting mono-exponential decays to the pump-probe scans, we have determined the vibrational lifetime T_1 as a function of temperature. Even though the observed transients can be well described by a convolution of a Gaussian with a mono-exponential decay (Fig. 6.2), it cannot be excluded that for small values of the delay the decay of the absorption at the $\nu_{OH} = 1 \rightarrow 2$ frequency might be partly determined by effects of spectral relaxation, similar to the decay of the bleaching at the $\nu_{OH} = 0 \rightarrow 1$ frequency (see the previous paragraph and Chapter 4). For this reason, only the data points for delay values larger than 1 ps were used in the fits to the measurements on liquid water.

Fig. 6.3 presents T_1 as a function of temperature. In ice, no significant temperature dependence is observed all the way from 30 K up to the melting point. At the transition from the solid to the liquid phase, T_1 suddenly increases from 384±16 to 745±47 fs. Note that in undercooled water at 270 K the vibrational lifetime is close to the value at room temperature, and roughly twice that measured in ice at 270 K. As the temperature of the water increases, the vibrational lifetime becomes significantly longer.

6.4 Discussion

6.4.1 THEORETICAL BACKGROUND

In describing the temperature dependence of vibrational relaxation rates in the condensed phase, it is often assumed that the accepting modes are harmonic oscillators, either phonons (in solids) or instantaneous normal modes (in liquids) [93]. This always leads to a vibrational lifetime that decreases with temperature. To illustrate this, let us assume for simplicity that only one accepting mode is involved in the vibrational relaxation process. We will call the high-frequency coordinate q and the low-frequency (accepting-mode) co-

ordinate Q. If the high-frequency excitation relaxes by the emission of m phonons of energy $\omega_Q = \omega_q/m$, the decay rate $K = 1/T_1$ due to the anharmonic coupling operator $\hat{q}\hat{Q}^m$ can be calculated with first-order perturbation theory [105]:

$$K(T) \propto \sum_{n_Q} P_{n_Q} |\langle 0_q\, n_Q + m | \hat{q}\hat{Q}^m | 1_q\, n_Q \rangle|^2, \tag{6.1}$$

where $|1_q\, n_Q\rangle$ and $|0_q\, n_Q + m\rangle$ denote the initial and final states of the relaxing system, and $P_{n_Q} = e^{-n_Q \hbar\omega_Q/k_\mathrm{B}T} / \sum_k e^{-k\hbar\omega_Q/k_\mathrm{B}T}$ is the thermal probability distribution. Writing $\hat{Q}$ in terms of phonon creation and annihilation operators, one obtains:

$$K(T) \propto |\langle 0_q | \hat{q} | 1_q \rangle|^2 \, (\bar{n}_Q + 1)^m, \tag{6.2}$$

where $\bar{n}_Q = (e^{\hbar\omega_Q/k_\mathrm{B}T} - 1)^{-1}$ is the thermal occupation number of the phonon. The same result is obtained if the anharmonic coupling is $\hat{q}\hat{Q}$, and mth-order perturbation theory is used to describe the relaxation [105]. Since $\bar{n}_Q$ increases with temperature, Eq. (6.2) predicts that the vibrational lifetime should decrease with increasing temperature.

This temperature dependence can be understood as follows: the value of the matrix element $\langle 0_q\, n_Q + m | \hat{q}\hat{Q}^m | 1_q\, n_Q \rangle$ strongly depends on the overlap of the q and Q wavefunctions, and increases with n_Q, since for a harmonic oscillator the corresponding $|n_Q\rangle$ and $|n_Q + m\rangle$ wavefunctions are more extended. With increasing temperature, higher levels of the Q mode will be occupied, and the thermally averaged value of the coupling matrix element increases.

Summarizing, if the accepting mode is a harmonic oscillator, the vibrational lifetime is predicted to decrease with temperature. This holds not only for the very simple situation discussed above, but also when more than one accepting mode is involved [93], or when higher-order perturbation theory is used to describe the relaxation [105].

6.4.2 The hydrogen bond as accepting mode

Previous studies have shown that in the vibrational relaxation of the $\nu_{\mathrm{OH}} = 1$ state of a hydrogen-bonded OH group a large part of the energy is transferred to the hydrogen-bond (O−H···O) mode [15, 79], which typically has a frequency of $\sim$200 cm^{-1}. Therefore, by virtue of the discussion in the previous section, one would expect a strong decrease of the vibrational lifetime with temperature, both in ice and in water. The observation that in ice the relaxation is nevertheless temperature independent, might be due to the fact that the hydrogen bond is a strongly anharmonic oscillator, the potential function possibly containing two minima separated by a barrier and/or strong quartic contributions [14, 81, 106]. As a result, the wavefunctions of the excited hydrogen-bond states are probably not much more extended than that of the ground state. Therefore, the matrix element $\langle 1_q n_Q | q Q^m | 0_q n_Q + m \rangle$ will be virtually independent of n_Q. Consequently, the thermal average of this matrix element, and therefore the vibrational lifetime, may be expected to depend only weakly on the temperature, as is indeed observed in ice.

At first sight, in liquid water a similar independence of temperature could be expected as in ice. However, the vibrational lifetime in water actually *increases* with temperature.

To our knowledge, up to now such an increase of the vibrational lifetime with temperature has only been observed for the T_{1u} stretching mode of $W(CO)_6$ dissolved in some organic solvents and in supercritical fluids [107–110]. For the latter systems, the increase of T_1 with temperature could be explained from the strong temperature dependence of the properties of the solvent just above the critical point. At temperatures sufficiently far above the critical point, the lifetime exhibited the usual decrease with increasing temperature. In the case of $W(CO)_6$ in some organic solvents, it was found that the increase of T_1 with temperature must result from a strong decrease of the coupling to the accepting modes with temperature, but the reason for this decrease could not be identified [111].

There are two temperature-dependent parameters that in principle could lead to a decrease of the coupling between the OH-stretching mode and the accepting bath mode with temperature (and thus to a decrease in vibrational lifetime), namely the density and the average hydrogen-bond strength.

Above 277 K, the density of liquid water decreases with increasing temperature, which in principle could lead to a lengthening of the vibrational lifetime [111]. Although it cannot be excluded that for liquid water the increase of T_1 with temperature partly results from the decrease in density, it is clear that the density in itself is not an important parameter since the T_1 of liquid water is much longer than that of the less dense ice.

A much more important effect is that the average hydrogen-bond strength decreases with increasing temperature [112], as can be derived from the redshift of the hydrogen-bond ($O-H\cdots O$) stretching frequency observed in the far-infrared and low-frequency Raman spectra of water [113, 114], and from the blueshift of the OH-stretching mode in the Raman and infrared spectra [115, 116]. In ice, the OH-stretch frequency varies much more slowly with temperature [115], which indicates that the effects mentioned below will be less relevant for ice.

A decrease of the hydrogen-bond strength will lead to a decrease of the anharmonic interaction between the OH-stretching mode and the hydrogen bond. If the hydrogen bond forms one of the accepting modes of the vibrational energy, this will lead to an increase of the vibrational lifetime. To see if such a mechanism could explain the observed temperature dependence of T_1(OH), we tried to describe our data with a previously developed model for the vibrational relaxation of hydrogen-bonded OH groups [53]. This model describes the vibrational relaxation of an isolated OH group hydrogen-bonded to an oxygen atom, and assumes that all vibrational energy initially present in the OH-stretching mode flows to the hydrogen-bond ($O-H\cdots O$) mode. It shows that the vibrational lifetime T_1(OH) strongly depends on the hydrogen-bond induced redshift $\delta\nu_{OH}$ of the OH-stretching frequency with respect to the gas-phase value, and predicts the power-law relation $T_1(\mathrm{OH}) \propto (\delta\nu_{OH})^{-1.8}$, which has been observed experimentally for a wide range of hydrogen-bonded complexes [117]. We used this relation and the experimentally observed temperature dependence of $\delta\nu_{OH}$ in dilute HDO:D_2O [115] to calculate the vibrational lifetime T_1(OH) as a function of temperature. The proportionality constant was chosen such that the calculated T_1 at 323 K equals the experimentally observed value. Since the thermal occupation of the hydrogen-bond mode is not expected to influence the temperature dependence of T_1 (see above), it was not incorporated in the analysis. The calculated T_1 is shown as the dashed curve in Fig. 6.3. The agreement between the calculated and

observed values is reasonably good over the entire temperature range from 30 to 363 K, especially in view of the fact that the model of Ref. [53], which describes an isolated O−H···O unit, is surely a strong oversimplification of the actual situation in liquid water.

It thus seems likely that the origin of the strong correlation between T_1(OH) and the hydrogen-bond strength lies in the anharmonic coupling between the OH-stretch and the hydrogen-bond modes, although it cannot be excluded that the hydrogen-bond strength and T_1(OH) are related in a different manner. For instance, the decrease of the hydrogen-bond induced redshift of the OH-stretch frequency with temperature might lead to an increase of the energy gap between the OH-stretch and *other* accepting modes, thereby decreasing the rate of vibrational energy transfer to these other modes. We think that as yet it is not possible to determine the precise mechanism behind the correlation between the lifetime and the hydrogen-bond strength, but we hope that our data will stimulate theoretical work to elucidate this mechanism.

6.5 Conclusions

Summarizing, we have found that the vibrational lifetime of the OH-stretching mode dramatically increases at the phase transition from ice to water, and shows a highly anomalous temperature dependence in the liquid phase. In ice, T_1(OH) is independent of temperature, probably due to the strong anharmonicity of the hydrogen-bond mode, which causes the coupling between the OH-stretch and hydrogen-bond modes to depend only weakly on the thermal occupation of the excited levels of the latter modes. We think the strong increase of T_1 at the phase transition from ice to water, and the increase of T_1 with temperature in the liquid both result from the concomitant decrease of the average hydrogen-bond strength.

Appendix: An upper limit for the heating in the focus

During the vibrational relaxation process the energy of the mid-infrared pump pulse, which is initially in the OH-stretch mode, is rapidly converted into heat. Between two laser pulses, this heat has some time to diffuse out of the focus to the sapphire windows, which have a much larger heat conductivity than D_2O and hence serve as a heat sink. After a sufficient number of laser shots, a steady state will establish, in which the amount of heat diffusing out of the focus in between two laser pulses is equal to the amount dumped per pulse. In this steady state, the temperature in the focus will be somewhat higher than in the rest of the sample.

To estimate in a simple way an upper limit for the steady-state temperature increase in the focus with respect to the rest of the sample, we assume that after the vibrational relaxation the heat is distributed uniformly over a cylindrically shaped volume, with a diameter of 300 μm (the diameter of the focus) and a length of $L = 500$ μm (the thickness of the sample). Since we only want to obtain an upper limit for the temperature in the focus, we will neglect the transverse diffusion of heat, and assume that all heat diffuses longitudinally, to the sapphire windows. This means that the problem reduces to a one-dimensional

heat diffusion problem, and the local temperature increase $\Delta T(z,t)$ is determined by [118]

$$\frac{\partial \Delta T(z,t)}{\partial t} = \kappa \frac{\partial^2 \Delta T(z,t)}{\partial z^2}, \text{ with } \kappa = \lambda/\rho c_p, \tag{6.3}$$

where c_p is the heat capacity per unit mass, ρ is the mass density, and λ is the thermal conductivity. Since the thermal conductivity of sapphire is orders of magnitude larger than that of liquid and solid D_2O [59], the windows are assumed not to heat up significantly. Hence we can safely the boundary conditions $\Delta T(0,t) = \Delta T(L,t) = 0$ for all t, where L is the length of the sample. Let T_0 be the initial temperature increase in the cylindrical volume due to one laser pulse. For the case of a single pump pulse hitting the sample at $t = t_0$ (initial condition $\Delta T(z,t_0) = T_0$ for $0 < z < L$), Eq. (6.3) is easily solved by writing $\Delta T(z,t)$ as a Fourier series in z. For the steady-state situation, we want to know $\Delta T(z,t)$ after an infinite number of pump pulses, at the moment just before the next pump pulse arrives. If the time between two laser pulses is Δt, this means we must add all separate temperature increases $\Delta T(z,0)$ due to the pump pulses hitting the sample at $t_0 = -m\Delta t$ ($m = 1,2,\ldots$). After carrying out the summation over m, the result is

$$\Delta T(z,0) = \sum_{n=0}^{\infty} \frac{4T_0 (e^{\kappa \Delta t[(2n+1)\pi/L]^2} - 1)^{-1}}{(2n+1)\pi} \sin\left(\frac{(2n+1)\pi z}{L}\right), \tag{6.4}$$

which has a maximum in $z = \frac{1}{2}L$. Using the thermophysical properties of D_2O ($c_p = 2.22 \cdot 10^3\ \mathrm{J\,kg^{-1}\,K^{-1}}$, $\rho = 1.018 \cdot 10^3\ \mathrm{kg\,m^{-3}}$, $\lambda = 2.28\ \mathrm{W\,K^{-1}\,m^{-1}}$ for D_2O ice at 260 K [119–121], and $c_p = 4.15 \cdot 10^3\ \mathrm{J\,kg^{-1}\,K^{-1}}$, $\rho = 1.105 \cdot 10^3\ \mathrm{kg\,m^{-3}}$, $\lambda = 0.589\ \mathrm{W\,K^{-1}\,m^{-1}}$ for liquid D_2O at 293 K [59, 119]). With a pump pulse energy of 25 μJ we have $T_0 = 0.154$ K in water and $T_0 = 0.314$ K in ice. Using Eq. (6.4) with $\Delta t = 14$ ms, we find $\Delta T(\frac{1}{2}L,0) = 0.53$ K in ice and $\Delta T(\frac{1}{2}L,0) = 2.60$ K in water. At lower temperatures the temperature rise in ice will be smaller than at 260 K, since λ scales approximately as T^{-1} [121] and c_p as T [119]. It should also be noted that in Eq. (6.4) only the $n = 0$ term contributes significantly to the steady-state heating. For this reason, approximately the same answer is obtained if a more realistic (exponentially decaying) z-dependence of the temperature profile shortly after a pump pulse is used. Finally, we see that the temperature increase T_0 caused by a single laser pulse is very small, so that the temperature during the pump pulse and the vibrational relaxation is well defined. In the experiments on pure water (see Chapter 8) this is no longer the case.

7 Comment on "Dynamics of Local Substructures in Water Observed by Ultrafast Infrared Hole Burning" and "Transient Hole Burning in the Infrared in an Ethanol Solution"

7.1 Introduction

Recently, a picosecond two-color pump-probe study on the OH-stretch absorption band of dilute HDO:D_2O has been published in Physical Review Letters by Laenen, Rauscher and Laubereau [23]. On the basis of their measurements, the authors claim to have burned spectral holes in the OH-stretch band of HDO:D_2O, and conclude that water has a three-component structure. The same authors have previously reported on very similar transient spectra in a pump-probe study on the OH-stretching mode of ethanol oligomers in CCl_4 [20].

Curiously, Laenen *et al.* completely neglect the coherent coupling between the pump and probe pulses in the analysis of their results. It has been known for quite some time that these coherent effects strongly influence the observed pump-probe signals [34, 46, 62, 66, 122–125] and lead to an increased probe transmission at the frequency of the pump pulse, even if the absorption line which is studied is homogeneously broadened [122]. Such a transmission increase in the transient spectrum might erroneously be interpreted as a spectral hole [124].

The purpose of the comment presented in this chapter is to demonstrate that the "spectral holes" observed by Laenen *et al.* are caused by a coherent coupling effect, and not by the selective bleaching of a certain "local substructure" in the OH-stretch absorption band. To demonstrate this, we will simply assume that the OH-stretch band is homogeneously broadened, calculate the pump-probe signal using the experimental parameters of Laenen *et al.*, and compare the results to their experimental observations on water [23] and ethanol [20].

7.2 Calculation

We describe the optical response of the OH-stretch mode in terms of the Bloch model for a homogeneously broadened transition, with center frequency ω_0, linewidth $2\gamma_2$ (in units of angular frequency), and population lifetime T_1. The pump and probe angular frequencies are ω_1 and ω_2 respectively, and the total electromagnetic field is given by

$$E(\mathbf{r},t) = \tfrac{1}{2}\left\{\tilde{E}_1(t)\,e^{i\mathbf{k}_1\cdot\mathbf{r}-i\Omega_1 t} + \tilde{E}_2(t-\tau)\,e^{i\mathbf{k}_2\cdot\mathbf{r}-i\Omega_2 t+i\omega_2\tau}\right\}e^{-i\omega_0 t} + \text{c.c.}, \qquad (7.1)$$

where $\Omega_j = \omega_j - \omega_0$ are the detunings of the pump ($j = 1$) and probe ($j = 2$) frequencies with respect to the resonance frequency ω_0, and τ is the delay between pump and probe. We will assume that the absorption band is much broader than the width of the power spectra of the pump and probe pulses. This is justified, since the FWHM of the OH-stretch band is 250 cm^{-1} [126], certainly much larger than the FWHM of the power spectra of the pump and probe pulses used in the experiment (8 cm^{-1} and 16 cm^{-1}, respectively [23]). When the absorption band is much broader than the power spectra of the pump and probe pulses, the free-induction decay can be considered instantaneous. Therefore, the polarizations induced by the pump and probe do not influence the shape of the pump and probe pulses, and to first order, the only effect the absorption band has on the pump and probe fields is to introduce an exponential decay of the amplitude as the beams propagate through the sample. Hence, in order to find the pump-probe signal, it suffices to calculate the third-order polarization at one specific position in the sample.

We write the first and third-order polarizations as

$$P^{(1)}_{\mathbf{k}_j}(\mathbf{r},t) = \tfrac{1}{2}\tilde{P}^{(1)}_{\mathbf{k}_j}(t)\, e^{i\mathbf{k}_j\cdot\mathbf{r} - i\omega_0 t} + \text{c.c.} \tag{7.2}$$

$$P^{(3)}_{\mathbf{k}_j}(\mathbf{r},t) = \tfrac{1}{2}\tilde{P}^{(3)}_{\mathbf{k}_j}(t)\, e^{i\mathbf{k}_j\cdot\mathbf{r} - i\omega_0 t} + \text{c.c.} \tag{7.3}$$

with $j = 1, 2$ for pump and probe, respectively. The equations for the time dependence of the first-order polarizations $\tilde{P}^{(1)}_{\mathbf{k}_j}$, the excited-state population $n^{(2)}_0$, the excited-state population grating $n^{(2)}_{\mathbf{k}_2-\mathbf{k}_1}$ and the third-order polarization $\tilde{P}^{(3)}_{\mathbf{k}_2}$ are given by perturbative solution of the Bloch equations for a homogeneous two-level system. In the rotating-wave approximation we have [124, 125]:

$$\frac{d\tilde{P}^{(1)}_{\mathbf{k}_1}}{dt} = \frac{iN|\mu_{12}|^2}{\hbar}\,\tilde{E}_1(t)\, e^{-i\Omega_1 t} - \gamma_2 \tilde{P}^{(1)}_{\mathbf{k}_1} \tag{7.4}$$

$$\frac{d\tilde{P}^{(1)}_{\mathbf{k}_2}}{dt} = \frac{iN|\mu_{12}|^2}{\hbar}\,\tilde{E}_2(t-\tau)\, e^{-i\Omega_2 t + i\omega_2\tau} - \gamma_2 \tilde{P}^{(1)}_{\mathbf{k}_2} \tag{7.5}$$

$$\frac{dn^{(2)}_0}{dt} = \frac{i}{4\hbar N}\left[\tilde{E}_1(t)\, e^{-i\Omega_1 t}\tilde{P}^{(1)*}_{\mathbf{k}_1} - \tilde{E}^*_1(t)\, e^{i\Omega_1 t}\tilde{P}^{(1)}_{\mathbf{k}_1}\right] - \gamma_1 n^{(2)}_0 \tag{7.6}$$

$$\frac{dn^{(2)}_{\mathbf{k}_2-\mathbf{k}_1}}{dt} = \frac{i}{4\hbar N}\left[\tilde{E}_2(t-\tau)\, e^{-i\Omega_2 t + i\omega_2\tau}\tilde{P}^{(1)*}_{\mathbf{k}_1} - \tilde{E}^*_1(t)\, e^{i\Omega_1 t}\tilde{P}^{(1)}_{\mathbf{k}_2}\right] - \gamma_1 n^{(2)}_{\mathbf{k}_2-\mathbf{k}_1} \tag{7.7}$$

$$\frac{d\tilde{P}^{(3)}_{\mathbf{k}_2}}{dt} = -\frac{2iN|\mu_{12}|^2}{\hbar}\left[\tilde{E}_1(t)\, e^{-i\Omega_1 t} n^{(2)}_{\mathbf{k}_2-\mathbf{k}_1} + \tilde{E}_2(t-\tau)\, e^{-i\Omega_2 t + i\omega_2\tau} n^{(2)}_0\right] - \gamma_2 \tilde{P}^{(3)}_{\mathbf{k}_2}, \tag{7.8}$$

where $\gamma_1 = 1/T_1$ and γ_2 is half the FWHM of the absorption band (in units of angular frequency). The excited-state density grating $n^{(2)}_{\mathbf{k}_2-\mathbf{k}_1}$ is formed by interference between the pump and probe pulses, and decays with the excited-state lifetime T_1. Diffraction of

the pump pulse from this grating gives rise to a contribution to the third order polarization in the direction of the probe. This coherent contribution to the pump-probe signal is represented by the first term in Eq. (7.8). The excited-state population $n_0^{(2)}$ caused by the pump pulse also decays with T_1, and interaction of $n_0^{(2)}$ with the probe pulse leads to the bleaching part of the pump-probe signal, represented by the second term in Eq. (7.8).

Solving equation (7.4), we obtain

$$\tilde{P}^{(1)}_{\mathbf{k}_1}(t) = \frac{iN|\mu_{12}|^2}{\hbar}\int_{-\infty}^{t} dt'\,\tilde{E}_1(t')\,e^{-i\Omega_1 t'+\gamma_2(t'-t)}. \tag{7.9}$$

We now use the fact that the pulse envelope varies very slowly compared to γ_2^{-1} to replace $\tilde{E}_1(t')$ by $\tilde{E}_1(t)$. One then obtains

$$\tilde{P}^{(1)}_{\mathbf{k}_1}(t) = \frac{iN|\mu_{12}|^2}{\hbar}\,\frac{\tilde{E}_1(t)\,e^{-i\Omega_1 t}}{\gamma_2 - i\Omega_1}, \tag{7.10}$$

and in the same way, by solving Eq. (7.5):

$$\tilde{P}^{(1)}_{\mathbf{k}_2}(t) = \frac{iN|\mu_{12}|^2}{\hbar}\,\frac{\tilde{E}_2(t-\tau)e^{-i\Omega_2 t+i\omega_2\tau}}{\gamma_2 - i\Omega_2}. \tag{7.11}$$

Substituting these equations into (7.6) and (7.7) and integrating, one obtains expressions for $n_0^{(2)}(t)$ and $n^{(2)}_{\mathbf{k}_2-\mathbf{k}_1}(t)$. Substituting these into (7.8) and integrating again, we obtain the following expression for the third-order polarization in the direction $\mathbf{k}_2$:

$$\begin{aligned}\tilde{P}^{(3)}_{\mathbf{k}_2}(t) = -\frac{iN|\mu_{12}|^4}{\hbar^3}\,\frac{1}{\gamma_2 - i\Omega_2}\,e^{-i\Omega_2 t+i\omega_2\tau}\int_{-\infty}^{0} dt'\,\Bigg[\frac{2\gamma_2}{\gamma_2^2+\Omega_1^2}\,e^{\gamma_1 t'}E_2(t-\tau)|E_1(t'+t)|^2 \\ + \left(\frac{1}{\gamma_2+i\Omega_1}+\frac{1}{\gamma_2-i\Omega_2}\right)e^{i(\Omega_1-\Omega_2)t'+\gamma_1 t'}E_1(t)E_1^*(t'+t)E_2(t'+t-\tau)\Bigg],\end{aligned} \tag{7.12}$$

where again the fact has been used that the pump and probe fields vary slowly compared to the free-induction decay. The pump-probe (bleaching) signal is given by the time-integrated gain $-\mathrm{Im}[E_2^* P^{(3)}_{\mathbf{k}_2}]$ of the probe field (see Section 1.3.2):

$$\begin{aligned}S(\Omega_1,\Omega_2,\tau) &= -\mathrm{Im}\int_{-\infty}^{\infty} dt\,\tilde{E}_2^*(t-\tau)e^{i\Omega_2 t-i\omega_2\tau}\tilde{P}^{(3)}_{\mathbf{k}_2}(t) \\ &= \frac{N|\mu_{12}|^4}{\hbar^3}\Bigg\{\frac{2\gamma_2^2}{(\gamma_2^2+\Omega_1^2)(\gamma_2^2+\Omega_2^2)}\int_{-\infty}^{0} dt' e^{\gamma_1 t'}\int_{-\infty}^{\infty} dt\,|E_2(t-\tau)|^2|E_1(t+t')|^2 \\ &\qquad + \mathrm{Re}\left[\frac{1}{\gamma_2-i\Omega_2}\left(\frac{1}{\gamma_2+i\Omega_1}+\frac{1}{\gamma_2-i\Omega_2}\right)\int_{-\infty}^{0} dt' e^{i(\Omega_1-\Omega_2)t'+\gamma_1 t'}\right. \\ &\qquad\qquad \left.\times\int_{-\infty}^{\infty} dt E_2^*(t-\tau)E_1(t)E_1^*(t'+t)E_2(t'+t-\tau)\right]\Bigg\}.\end{aligned} \tag{7.13}$$

This expression consists of two terms (which correspond to the $\gamma(\tau)$ and $\beta(\tau)$ terms of section 3.3.3). The first term in this expression is a convolution of the cross-correlation function of the pump and probe intensities with an exponential decay with time constant T_1.

This is the well-known incoherent part of the pump-probe signal, and its delay dependence is determined by the value of the population lifetime T_1. As expected, its probe-frequency (Ω_2) dependence simply follows the broad Lorentzian absorption lineshape. The second term in Eq. (7.13) is caused by coherent coupling between pump and probe. Its delay dependence is determined by the temporal overlap of the pump and probe fields. This is to be expected, since it represents an interference effect between pump and probe.

In case the pump and probe fields are Gaussian:

$$\tilde{E}_j(t) = e^{-d_j t^2}, \tag{7.14}$$

with $j = 1,2$ for pump and probe, the integrations in Eq. (7.13) can be carried out, and the result is:

$$\begin{aligned} S(\Omega_1,\Omega_2,\tau) = \frac{\pi N|\mu_{12}|^4}{2\hbar^3}\Bigg\{ & \frac{\gamma_2^2}{(\gamma_2^2+\Omega_1^2)(\gamma_2^2+\Omega_2^2)} \exp\left(\gamma_1 \frac{\gamma_1(d_1+d_2)-8d_1d_2\tau}{8d_1d_2}\right) \\ & \times\left(1+\operatorname{erf}\left(\frac{4d_2d_1\tau-\gamma_1(d_1+d_2)}{2\sqrt{2(d_1+d_2)d_1d_2}}\right)\right) + \operatorname{Re}\Bigg[\frac{1}{\gamma_2-i\Omega_2}\left(\frac{1}{\gamma_2+i\Omega_1}+\frac{1}{\gamma_2-i\Omega_2}\right) \\ & \times\exp\left(\frac{[\gamma_1+i(\Omega_1-\Omega_2)]^2-4d_1d_2\tau^2}{d_1+d_2}\right)\left(1-\operatorname{erf}\left(\frac{\gamma_1+i(\Omega_1-\Omega_2)}{\sqrt{2(d_1+d_2)}}\right)\right)\Bigg]\Bigg\} \end{aligned} \tag{7.15}$$

7.3 Results

7.3.1 "Spectral holes" in water

Both in Ref. [23] and in Ref. [20] the pulse envelopes were Gaussian, the FWHM of the pump and probe intensity envelopes being 1 and 2 ps. This means we can use Eq. (7.15), with $d_1 = 0.347$ ps^{-2} and $d_2 = 1.386$ ps^{-2}, to calculate the transient spectra and delay scans that would be obtained if the OH-stretch absorption band of HDO:D_2O were homogeneously broadened. We take $\gamma_2 = 23.6$ THz, which corresponds to a FWHM of the absorption band of 250 cm^{-1} (this is the actual FWHM of the OH-stretch absorption band [126]), and $\gamma_1 = 1.35$ Thz ($T_1 = 0.74$ ps, see Chapter 6), and a band center frequency of 3410 cm^{-1}. In the remainder of this section, we will subsequently analyze all of the measurements presented in Ref. [23] in terms of a homogeneously broadened OH stretch band, that is, in terms of Eq. (7.15).

Fig. 7.1 shows transient spectra calculated using Eq. (7.15), for four different delay values and a pump frequency of 3490 cm^{-1}. The reader should note the good agreement between these calculated transient spectra and the transient spectra presented by Laenen *et al.* in Fig. 1(a)–(c) of their article [23]. Since the analysis above only takes the $v_{OH} = 0$ and $v_{OH} = 1$ levels into account, we only reproduce the bleaching part of the transient spectrum (probe frequencies larger than 3200 cm^{-1}), and the experimentally observed excited-state ($v_{OH} = 1 \rightarrow 2$) absorption at $\sim$3000 cm^{-1} is not reproduced in our calculation. Of course, the calculation can easily be extended to include the $v_{OH} = 2$ level (and hence the excited-state absorption) as well.

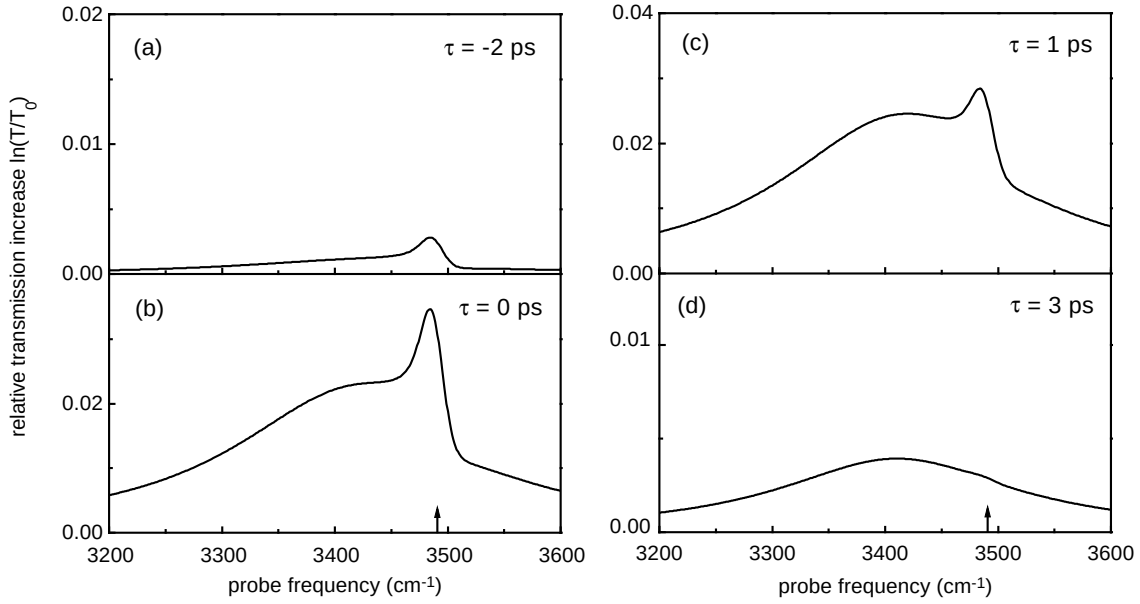

FIGURE 7.1. Calculated transient spectra for delay values of (a) $\tau = -2$ ps, (b) $\tau = 0$ ps, (c) $\tau = 1$ ps, and (d) $\tau = 3$ ps. The pump frequency is 3490 cm^{-1} (indicated with an arrow on the frequency axis). These calculated spectra should be compared to the experimental transient spectra shown in Figs. 1(a)–(c) of Ref. [23].

The transient spectra consist of two parts: a broad background due to the bleaching of the absorption band by the pump pulse (the first term in Eq. (7.13)), and a sharp feature which is only present when pump and probe have temporal overlap, and which is due to coherent coupling (the second term in Eq. (7.13)). The good agreement between Eq. (7.15) and the measurements strongly suggests that the sharp peaks at the pump frequency observed by Laenen *et al.* at delay values of $\tau = -2$ and $\tau = 1$ ps simply represent the coherent coupling between pump and probe, and not a spectral hole due to the bleaching of a "selected subensemble" [23]. At delay $\tau = 3$ ps, see Fig. 7.1(d), the coherent peak in the transient spectrum disappears since the pump and probe pulses no longer overlap. This is precisely what is observed in the experimental transient spectrum at $\tau = 3$ ps, shown in Fig. 1(c) of the article [23]. The broad background signal on the other hand, which represents the true bleaching and decays with the excited-state population lifetime T_1, is still present at $\tau = 3$ ps, both in the calculated and the experimental transient spectrum.

In Fig. 2 of the paper [23], transient spectra are presented in which the pump frequency was 3430 cm^{-1}, and the delay set to $\tau = 0$ ps. Again, coherent coupling gives rise to an increased transmission of the probe pulse at the pump frequency. A transient spectrum calculated using Eq. (7.15) is shown in Fig. 7.2. There is reasonable agreement between the calculated and experimental transients, especially in view of the simple model we used to describe the optical response.

It is well known that coherent coupling between the pump and probe pulses not influences the transient spectra, but also the pump-probe delay scans [64]. When pump and probe have the same frequency, it is clear that coherent coupling gives rise to an extra contribution to the pump-probe signal when the pulses have temporal overlap (see Ref. [64]

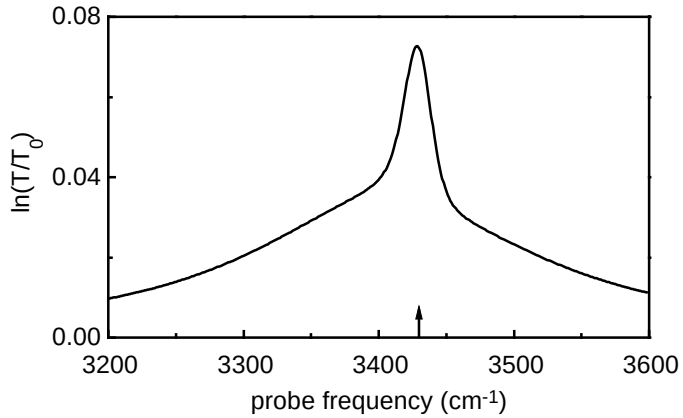

FIGURE 7.2. Calculated transient spectrum for $\tau = 0$ ps and a pump frequency of 3430 cm^{-1} (indicated with an arrow on the frequency axis). Cf. the experimental transient spectrum presented in Fig. 2(b) of Ref. [23].

or section 3.3.3). This extra contribution around delay zero is not present when pump and probe have different frequencies. This is precisely what is observed in the delay scans presented in Fig. 3 of the article. When the probe is tuned to the pump frequency of 3410 cm^{-1} (curves labeled 'II' in Fig. 3 of the article [23]), the coherent contribution to the signal causes the signal to rise significantly faster than when the probe is tuned to 3340 cm^{-1} (curves labeled 'I' in Fig. 3 of the article). This effect is nicely reproduced by Eq. (7.15), as can be seen from the calculated delay scans shown in Fig. 7.3. According to Laenen *et al.* however (p. 2624 of the article [23]), the "slower amplitude growth" of curve 'I' with respect to curve 'II' is not caused by a coherent effect, but by "cross relaxation, i.e., conversion of molecules in environments I and II."

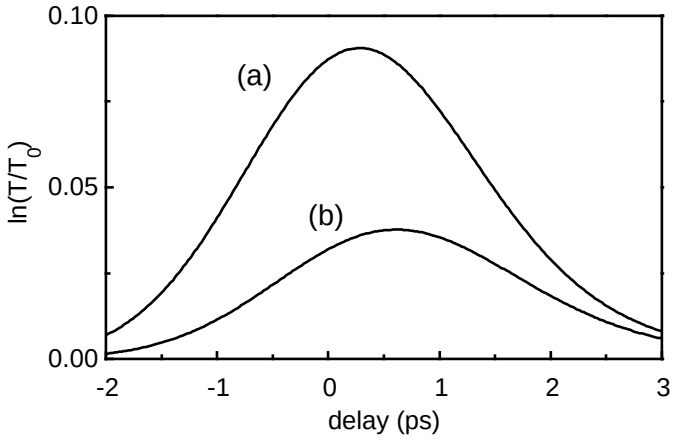

FIGURE 7.3. Delay scans calculated using Eq. (7.15), with a pump frequency of 3410 cm^{-1}, and probe frequencies of 3410 cm^{-1} (a) and 3340 cm^{-1} (b). Cf. the experimental delay scans presented in Fig. 3 of Ref. [23], where they are labeled as 'II' and 'I', respectively.

7.3.2 "SPECTRAL HOLES" IN ETHANOL

The explicit expression (7.15) for the pump-probe signal in a two-color experiment on a homogeneous transition is a very general one, and applies for arbitrary γ_1, γ_2, and pulse durations. The only assumption made is that the pulse is significantly longer than the free-induction decay, which is very often satisfied, in particular in the case of the very broad OH stretching bands.

Equation (7.15) can therefore also be applied to the two-color pump-probe experiments on the OH-stretch mode of hydrogen bonded ethanol, which were presented previously by Laenen, Rauscher and Laubereau [20]. In the transient spectra of their study on ethanol, the authors again observe sharp "spectral holes" at the pump frequency, again superimposed on a very broad bleaching signal. Interestingly, these "spectral holes" always have the same width, *independent* of the pump frequency. Furthermore, in ethanol they have virtually the same width as the "spectral holes" in water. Precisely as in water, in ethanol the "spectral holes" disappear when the pump and probe pulses have no temporal overlap, see Fig. 1(c) of the article [20].

All of this strongly suggests that the "spectral holes" in ethanol are also caused by coherent coupling between the pump and probe pulses. This is confirmed by the good agreement between transient spectra calculated using Eq. (7.15) and the experimentally observed transient spectra [20]. As an example, Fig. 7.4 presents a calculated transient spectrum for delay $\tau = 0$ and a pump frequency of 3450 cm^{-1}, which the reader should

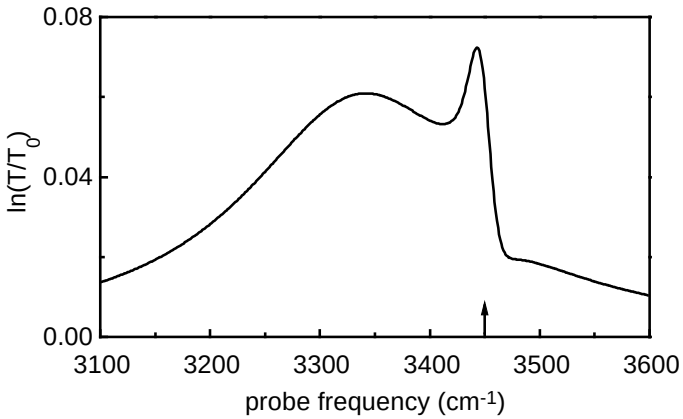

FIGURE 7.4. Transient spectrum for the OH-stretch mode of ethanol oligomers calculated using Eq. (7.15), with a pump frequency of 3450 cm^{-1}, and delay $\tau = 0$ ps. Cf. the experimentally observed transient spectrum shown in Fig. 2(b) of Ref. [20].

compare to the experimental transient spectrum presented in Fig. 2(a) of Ref. [20]. We have taken $\gamma_1 = 1.11$ Thz ($T_1 = 0.9$ ps, see Table 3.1), and $\gamma_2 = 18.8$ THz (which corresponds to the experimental FWHM of 200 cm^{-1} of the absorption band [15]), and a band-center frequency of 3330 cm^{-1} (see Fig. 3.1).

In their analysis of the ethanol experiments, Laenen *et al.* again do not take coherent coupling effects into account, and they interpret the sharp feature in the transient spectrum as due to selective bleaching of certain ethanol oligomers. Indeed, the authors explicitly exclude the possibility that the "spectral holes" in ethanol are caused by a coherent cou-

pling effect. They support this claim by noting that the ratio of the sharp peak and the broad bleaching signal does not change when changing pump intensity (p. 3204 of the article [20]). This however, is *precisely* what one expects for a coherent artefact, since both the bleaching and the coherent artefact scale linearly with the pump intensity. This is clearly seen in Eq. (7.13): both the incoherent bleaching term and the coherent coupling term contain twice the pump amplitude $\tilde{E}_1$. Therefore, this intensity-independence confirms rather than excludes that the sharp peaks are caused by coherent effect.

7.4 Conclusions

Summarizing, we see that the peaks Laenen *et al.* refer to as "spectral holes" are caused by coherent coupling between pump and probe, and they contain no information whatsoever about the broadening mechanism of the OH-stretch absorption band, neither in water nor in ethanol. Nearly all of the results presented by Laenen *et al.* in Refs. [23] and [20] can be well described by assuming a homogeneously broadened OH-stretch absorption band. Of course, this does not imply that the absorption band is indeed homogeneously broadened; it does imply that it is not possible to decide whether or not the band is homogeneous on the basis of the results of Laenen *et al.*, and that an interpretation of their measurements on water in terms of three different "local substructures" can hardly be taken seriously.

8 Vibrational Förster transfer in liquid water

8.1 Introduction

In the previous four chapters, the dynamics of the OH-stretch vibration have been studied in dilute solutions of HDO in D_2O, a system that is often used to study vibrational dynamics in liquid water [22, 23, 31, 115, 127]. The use of HDO:D_2O solutions was motivated by the fact that the intermolecular coupling of the OH-stretch vibrations of different HDO molecules will be negligible if the solutions are sufficiently diluted. As a consequence, the OH-stretch oscillators can be regarded as isolated with respect to each other, and their dynamics are determined only by their (hydrogen-bond) interactions with the surrounding D_2O molecules.

It may be expected that in 'real' water (H_2O) the coupling between the OH-stretch vibrations is very strong. This means that the OH-stretch excitation will not remain on one molecule, but will rapidly be transferred to surrounding OH-oscillators. It is the purpose of this Chapter to investigate this intermolecular transfer of the OH-stretch excitation in liquid water.

In general, the OH-groups of two molecules in liquid water will not be oriented parallel, and transfer of an OH-stretch excitation from one molecule to another will result in a change of the polarization of the excitation. This means that the energy transfer leads to a decay of the rotational anisotropy of the excitation. Hence, a straightforward method to study the intermolecular transfer of the OH-stretch excitation is to excite a fraction of the OH-oscillators to the $v_{OH} = 1$ state, and to measure how the anisotropy of the absorption of the excited molecules decays with increasing time.

Since the transfer rate depends strongly on the distance between the 'donor' and 'acceptor' molecule, the average transfer rate will depend strongly on the concentration of OH-oscillators. Hence, by varying the concentration, we can distinguish the direct energy transfer from other contributions to the decay of the rotational anisotropy, in particular the orientational diffusion of the OH-groups.

8.2 Experiment

With the setup described in Section 2.4.2, two independently tunable mid-infrared pulses with a duration of approximately 200 fs are generated. One of these pulses has an energy of approximately 20 μJ and is used as pump, the other has an energy of less than 1 μJ and is used as probe. The pump pulse is tuned to the center frequency of the $v_{OH} = 0 \rightarrow 1$ absorption band, and the probe pulse to the $v_{OH} = 1 \rightarrow 2$ transition frequency. The pump pulse induces a significant population of the $v_{OH} = 1$ level. This results in transient anisotropic absorption changes, which are monitored by the probe pulse. The probe polarization

is at 45° with respect to the pump polarization, and the relative transmission changes $\ln(T/T_0)_{||}$ and $\ln(T/T_0)_{\perp}$ of the parallel and perpendicular polarization components are monitored simultaneously as a function of delay. In this way, both the rotation-free signal $\ln(T/T_0)_{||} + 2\ln(T/T_0)_{\perp}$ and the rotational anisotropy R (defined by Eq. (5.2)) are determined as a function of the delay between pump and probe.

The samples consist of a thin layer of either HDO dissolved in D_2O or pure H_2O. The HDO:D_2O samples are prepared by mixing appropriate amounts of H_2O (HPLC grade) and D_2O (>99.9 atom% D), and are kept between two CaF_2 windows separated by a teflon spacer of 15 or 25 μm thickness. Samples consisting of pure H_2O are prepared by squashing a droplet of H_2O (HPLC grade) between two CaF_2 windows, and applying pressure until the sample is sufficiently thin. The sample thickness achieved in this way is approximately 1 μm, as determined from the sample transmission and literature values [128, 129] of the infrared extinction coefficient of liquid H_2O. All experiments are performed at room temperature (298 K).

In order to perform pump-probe spectroscopy in transmission, the sample has to be sufficiently thin to transmit a measurable fraction of the probe intensity. More specifically, with the highly concentrated HDO:D_2O and pure H_2O samples used in this chapter, the required thickness varies from 1 to 25 μm. At these densities of OH-groups, the vibrational relaxation process (conversion of the vibrational energy into heat) results in a significant temperature increase in the focus. In fact, even a single laser shot will result in a temperature increase of several K. This means that it is essential to avoid accumulated heating in the focus. In the previous chapters, this was done by circulating the water. However, with the thin samples used in this chapter, very high pressures would be needed to achieve this. Therefore, we have used a different method to make sure that a fresh part of the sample is in the focus with each laser shot (see Fig. 8.1). In this approach, the entire sample is rapidly rotated using a small DC motor. The sample cell holder and the motor are mounted on a heavy aluminum block to reduce mechanical vibration.

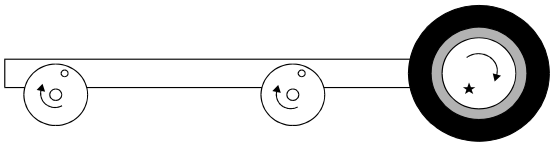

FIGURE 8.1. Sample-cell mount used in the experiments presented in this chapter. The laser beam is directed perpendicular to the plane of the page, and the focus (represented by an asterisk) is at a fixed position. The sample is rapidly rotated to avoid steady-state heating.

8.3 Results and discussion

8.3.1 General considerations

Fig. 8.2 represents a typical pump-probe scan, recorded in an 8.7 M solution of HDO in D_2O, with a pump frequency of 3400 $cm^{-1}$and a probe frequency of 3000 cm^{-1}. The relative transmission changes $\ln(T/T_0)_{||}$ and $\ln(T/T_0)_{\perp}$ of the probe polarization components parallel and perpendicular to the pump polarization are plotted as a function of delay

between pump and probe. The negative value of $\ln(T/T_0)$ observed for small delay values is due to the excited-state ($\nu_{OH} = 1 \rightarrow 2$) absorption, and decays as the excited HDO molecules relax to the vibrational ground state. For large delay, $\ln(T/T_0)$ approaches a small positive value due to the temperature increase that occurs upon vibrational relaxation. Both in HDO:D_2O [126] and in pure H_2O [128, 129] the $\nu_{OH} = 0 \rightarrow 1$ absorption band shifts towards higher frequency and decreases in magnitude with increasing temperature. Since the spectrum of the probe pulse slightly overlaps with the $\nu_{OH} = 0 \rightarrow 1$ absorption band, the increase in temperature upon vibrational relaxation causes a small increase of the transmission of the probe pulse. In order to study the orientational and

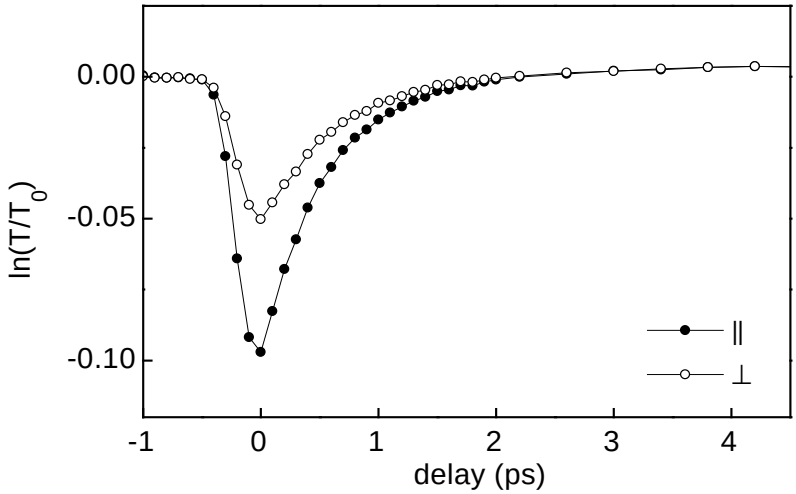

FIGURE 8.2. Pump-probe scans recorded in liquid HDO:D_2O with $\nu_{pu} = 3400$ cm^{-1}and $\nu_{pr} = 3150$ cm^{-1}, showing the absorption increase at the probe frequency vs. the delay between the pump and probe pulses, for the parallel (solid circles) and perpendicular (open circles) components of the probe pulse.

vibrational relaxation in more detail, we subtract the small transmission increase caused by the temperature rise. In this way, we obtain the parallel and perpendicular components of the excited-state absorption as a function of delay. From these we calculate the rotation-free signal $\ln(T/T_0)_{||} + 2\ln(T/T_0)_{\perp}$, which is not sensitive to the orientational dynamics and only probes the excited-state decay, and the rotational anisotropy R (defined by Eq. (5.2)), which is only sensitive to the orientational dynamics and not to the population relaxation [46].

8.3.2 HDO DISSOLVED IN D_2O

The rotation-free signal observed for three different HDO concentrations is shown in Fig. 8.3. For delay values larger than 1 ps, all transients can be described with a single-exponential decay with a time constant of 720 fs. This value represents the vibrational lifetime T_1 of the OH-stretch mode (see Chapter 6). Clearly, the vibrational relaxation dynamics of the OH-stretch mode of HDO in D_2O shows no significant dependence on the HDO concentration.

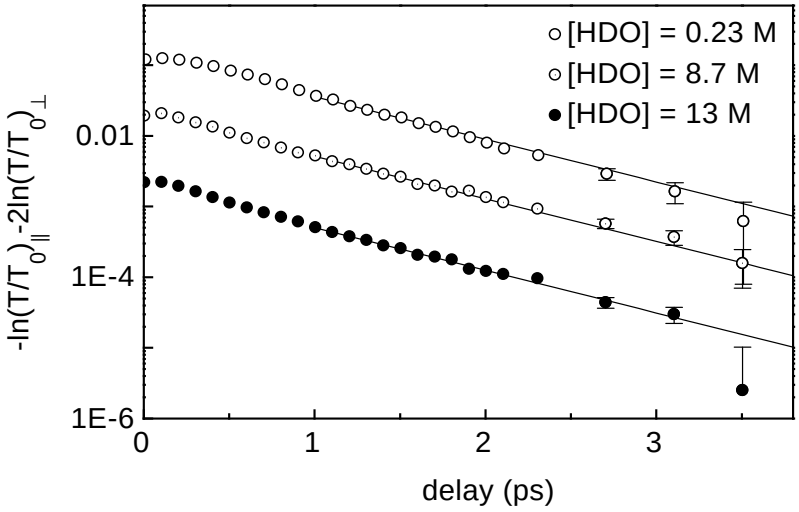

FIGURE 8.3. Rotation-free excited-state absorption $-\ln(T/T_0)_{||} - 2\ln(T/T_0)_{\perp}$ recorded in HDO:D_2O solutions with three different HDO concentrations. The pump frequency and probe frequencies are $\nu_{pu} = 3400$ cm^{-1}and $\nu_{pr} = 3150$ cm^{-1}, respectively. The transients for [HDO] = 8.7 M and [HDO] = 13 M have been vertically displaced for clarity. The solid lines represent a single-exponential decays with a time constant of 720 fs.

From the transmission changes $\ln(T/T_0)_{||}$ and $\ln(T/T_0)_{\perp}$ of the parallel and perpendicular components of the probe pulse, we can calculate the rotational anisotropy *R*, defined by Eq. (5.2). Fig. 8.4 shows *R*, normalized with respect to the value at zero delay, as a function of the delay between pump and probe. In contrast to the vibrational relaxation, the orientational relaxation dynamics of the OH-stretch excitation clearly depend strongly on the HDO concentration. Clearly, the contribution of the orientational diffusion of the HDO molecules to the decay of *R* will not depend on the HDO concentration. The observation of a concentration dependence of the orientational dynamics therefore constitutes strong evidence for direct transfer of the OH-stretch excitation between the HDO molecules. This process is usually referred to as Förster energy transfer [56], and has been observed previously both for electronic [130–133] and vibrational excitations [57, 134]. The rate of Förster transfer by dipole-dipole coupling between an excited molecular oscillator and an oscillator in the ground state is proportional to $1/r^6$, where *r* is the distance between the two oscillators (see Eq. (3.1)). Since the 'acceptor' transition dipole will generally not be oriented parallel to the 'donor' transition dipole, the Förster transfer leads to a decay of the rotational anisotropy. Because of the strong dependence of the transfer rate on the intermolecular distance, Förster transfer causes the rotational anisotropy to decay faster with increasing concentration, as observed in Fig. 8.4. To our knowledge, this constitutes the first observation of vibrational Förster transfer in a liquid.

In a quantitative analysis of the data, it must be realized that the decay of the rotational anisotropy with increasing delay τ is determined by two processes: (1) the random orientational motion of the HDO molecules (discussed in Chapter 5); (2) Förster energy transfer of the OH-stretch excitation from the optically excited 'donor' HDO molecules (oriented approximately parallel to the polarization of the pump pulse) to randomly oriented surrounding 'acceptor' HDO molecules. In a model often used to describe Förster energy

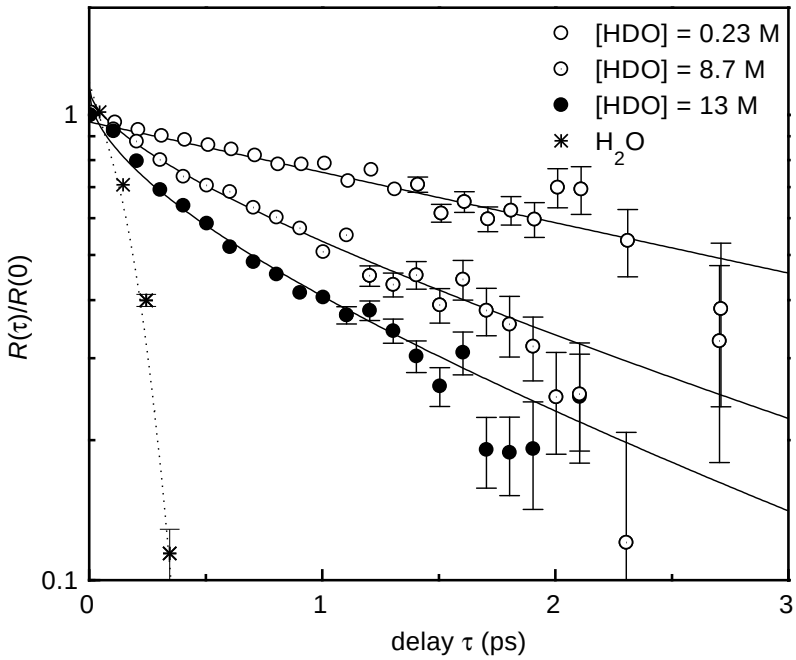

FIGURE 8.4. Rotational anisotropy R, normalized with respect to the value at delay zero, recorded in HDO:D_2O solutions with three different HDO concentrations and in pure H_2O. The pump frequency and probe frequencies are $\nu_{pu} = 3400$ cm^{-1}and $\nu_{pr} = 3150$ cm^{-1}, respectively. The solid curves have been calculated using Eq. (8.7). The dotted curve has been calculated using Eq. (8.8).

transfer [133, 135], it is assumed that once the excitation has been transferred from an optically excited ($v_{OH} = 1$) molecule to a randomly oriented acceptor ($v_{OH} = 0$) molecule, it no longer contributes to the rotational anisotropy. Detailed calculations show that after one or more transfers the excitation will contribute less than 3% to the rotational anisotropy [135]. Note that the acceptor molecules will indeed be randomly oriented, since only a very small fraction of the HDO molecules is excited to the $v_{OH} = 1$ state (approximately 1%, as determined from the relative absorption change). This means that the (anisotropic) depletion of the ground state will not significantly change the isotropic orientational distribution of the acceptor ($v_{OH} = 0$) molecules. If we momentarily neglect the orientational random motion of the exited molecules, then the contribution of an OH-stretch excitation to the rotational anisotropy will decay as the probability that it is still on the initially excited HDO molecule. If a particular molecule is excited at $t = 0$, then the probability $\rho(\tau)$ that at $t = \tau$ the molecule is still excited is given by [136]

$$\rho(\tau) = \langle \prod_{j=1}^{N} \exp[-w_j \tau] \rangle, \tag{8.1}$$

where w_j is the rate constant for Förster energy transfer from the excited molecule to acceptor molecule j, N is the number of acceptor molecules, and $\langle \ldots \rangle$ denotes a statistical average over all possible spatial distributions of the acceptor molecules. The assumption that once the excitation has been transferred, it no longer contributes to the rotational

anisotropy implies that $R(\tau)$ is proportional $\rho(\tau)$. If we assume for simplicity that w_j depends only on the distance r_j between the donor and acceptor (not on their relative orientation), we have the well-known relation

$$w_j = \frac{1}{T_1}\left(\frac{r_0}{r_j}\right)^6, \tag{8.2}$$

where r_0 is a constant, usually referred to as the Förster radius [136, 137]. The acceptor molecules are randomly distributed, so the probability of finding acceptor j at a distance between r_j and $r_j + dr_j$ is simply $4\pi r_j^2 dr_j/V$, with V the total volume of the sample. Averaging over this probability distribution for each molecule, we have

$$\rho(\tau) = \left\{\frac{4\pi}{V}\int_0^\Lambda \exp\left[-\frac{\tau}{T_1}\left(\frac{r_0}{r}\right)^6\right] r^2 dr\right\}^N, \tag{8.3}$$

where we have assumed that the sample is a sphere with radius Λ, centered at the excited molecule (hence $V = 4\pi\Lambda^3/3$). Performing the integration, we obtain

$$\rho(\tau) = \left\{\exp\left[-\frac{\tau}{T_1}\left(\frac{r_0}{\Lambda}\right)^6\right] + \sqrt{\frac{\pi\tau}{T_1}\left(\frac{r_0}{\Lambda}\right)^6}\left[\operatorname{erf}\left(\sqrt{\frac{\pi\tau}{T_1}\left(\frac{r_0}{\Lambda}\right)^6}\right) - 1\right]\right\}^N. \tag{8.4}$$

Using the fact that the concentration (expressed in particles per unit of volume) is $[\mathrm{C}] = 3N/4\pi\Lambda^3$ to eliminate Λ, and expanding in terms of $1/N$, we obtain

$$\rho(\tau) = \left\{1 - \frac{4\pi^{3/2}[\mathrm{C}]}{3}\sqrt{\frac{r_0^6\tau}{T_1}}\left(\frac{1}{N}\right) + O\left(\frac{1}{N}\right)^2\right\}^N. \tag{8.5}$$

Taking the thermodynamic limit $N \to \infty$, we obtain

$$\rho(\tau) = \exp\left(-\frac{4\pi^{3/2}}{3}[\mathrm{C}]\sqrt{\frac{r_0^6\tau}{T_1}}\right). \tag{8.6}$$

This delay and concentration dependence of the decay of the rotational anisotropy as a consequence of Förster transfer has been experimentally confirmed for optical excitations in the visible [131, 132].

It is reasonable to assume that the orientational motion of the HDO molecules and the Förster transfer are independent processes. If we furthermore assume that the orientational random motion of the HDO molecules results in an exponential decay of R with time constant τ_{or}, then the total decay of the anisotropy will given by:

$$\frac{R(\tau)}{R(0)} = \exp\left(-\frac{\tau}{\tau_{\mathrm{or}}} - \frac{4\pi^{3/2}}{3}[\mathrm{HDO}]\sqrt{\frac{r_0^6\tau}{T_1}}\right). \tag{8.7}$$

We found that all scans recorded in HDO:D_2O can be well described by Eq. (8.7), with $\tau_{or} = 4.0$ ps and a Förster radius $r_0 = 2.2$ Å (solid curves in Fig. 8.4). From Eq. (8.2) we see that r_0 is the distance between two OH-oscillators at which the Förster transfer rate becomes comparable to the vibrational relaxation rate. The large value of τ_{or} is due to the fact that in the pump-probe scans presented in this chapter the $v_{OH} = 1$ state is probed, which is more strongly hydrogen-bonded than the $v_{OH} = 0$ state (see Chapter 4). As a consequence, the orientational motion will take place very slowly (see Chapter 5).

8.3.3 LIQUID H_2O

Fig. 8.4 also shows the decay of the rotational anisotropy observed for the OH-stretch excitation in liquid H_2O. This decay occurs on a very rapid time scale, only slightly slower than the cross-correlation trace $C(\tau)$ of the pump and probe intensity envelopes.

To investigate this in more detail, we compare both the numerator $\ln(T/T_0)_{||} - \ln(T/T_0)_{\perp}$ and the denominator $\ln(T/T_0)_{||} + 2\ln(T/T_0)_{\perp}$ of R with the cross-correlation function $C(\tau)$, see Fig. 8.5. Clearly, the denominator decays more slowly than the cross-correlation function, which implies that the population relaxation, and hence the decay of $\ln(T/T_0)_{||}$ and $\ln(T/T_0)_{\perp}$, does not take place very fast. On the other hand, the numerator $\ln(T/T_0)_{||} - \ln(T/T_0)_{\perp}$ does not differ significantly from the cross-correlation. Since the decay of $\ln(T/T_0)_{||}$ and $\ln(T/T_0)_{\perp}$ is much slower (on the order of that of the rotation-free signal), this must be due to an instantaneous orientational scrambling of the OH-stretch excitation that rapidly reduces the difference between $\ln(T/T_0)_{||}$ and $\ln(T/T_0)_{\perp}$ to zero.

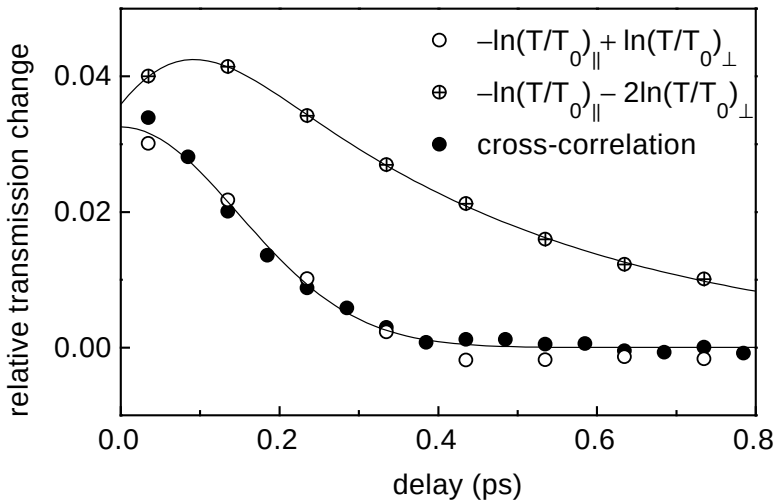

FIGURE 8.5. Numerator $\ln(T/T_0)_{||} - \ln(T/T_0)_{\perp}$ and denominator $\ln(T/T_0)_{||} + 2\ln(T/T_0)_{\perp}$ of the rotational anisotropy. The denominator has been scaled by a factor 1/6 for better comparison. Also shown is the cross-correlation of the intensity envelopes of the pump and probe pulses. The solid lines show least-squares fits to the cross-correlation (Gaussian) and to the denominator (convolution of a Gaussian with a single-exponential decay).

Curiously, even though the difference $\ln(T/T_0)_{||} - \ln(T/T_0)_{\perp}$ follows the cross-correlation $C(\tau)$, the decay of $R(\tau)$ can nevertheless still take place *slower* than that of

$C(\tau)$. This can be understood as follows. If the orientational relaxation takes place instantaneously on the time scale of the pulses, the delay dependence of the numerator of R is given by $C(\tau)$, and we have

$$R(\tau) \propto \frac{C(\tau)}{\ln[T(\tau)/T_0]_{||} + 2\ln[T(\tau)/T_0]_{\perp}}. \tag{8.8}$$

If the denominator decays on a fast enough time scale, it will decrease significantly with increasing τ even within the duration of the cross-correlation. In that case, $R(\tau)$ is given by $C(\tau)$ divided by a rapidly decaying function, and hence will decay slower than $C(\tau)$. Only if the denominator is a constant (infinitely slow decay of the rotation-free signal) R will decay equally fast as $C(\tau)$. Thus, the decay of R in H_2O observed in Fig. 8.4 does not mirror the orientational relaxation, but is determined by the cross-correlation function and the decay of the rotation-free signal (the denominator of R), which is determined by population relaxation only.

Indeed, if we evaluate (8.8) using least-squares fits to the cross-correlation function and rotation-free signal (solid curves in Fig. 8.5), we find that this expression gives a reasonable description of decay of the rotational anisotropy in H_2O (dotted curve in Fig. 8.4). This shows that in liquid water the orientational scrambling of the OH-stretch excitation occurs instantaneously on the time scale of our experiments ($\sim$100 fs).

Part of the orientational scrambling observed in H_2O will be due to intramolecular transfer of the OH-stretch excitation. Excitation of the either the symmetric or antisymmetric OH-stretch mode of the H_2O molecule is followed by a rapid intramolecular redistribution of the excitation over the two modes [138]. It is easily shown that the complete transfer of a dipole excitation from an initially excited oscillator to an accepting oscillator changes the rotational anisotropy from the initial value of $\frac{2}{5}$ to $\frac{2}{5}P_2(\cos\delta)$, where P_2 is the second-order Legendre polynomial and δ the angle between the two transition dipole moments [139]. Since for the symmetric and antisymmetric OH-stretch modes of H_2O we have $\delta = 90°$, and the excitation will be distributed with equal probabilities over the symmetric and antisymmetric modes, we expect that the intramolecular redistribution will reduce the anisotropy to $\frac{1}{2}(\frac{2}{5} + \frac{2}{5}P_2(0)) = \frac{1}{10}$. Thus, the intramolecular transfer causes the rotational anisotropy to decrease to a quarter of its initial value. The complete vanishing of R is caused by the intermolecular energy transfer.

It should be noted this intermolecular energy transfer will be of a more complicated nature than is described by Eq. (8.2). Because of the high density of OH-groups in liquid H_2O a simple expression of the form (8.2), which describes the interaction between two point dipoles separated by large distance, can no longer be used. In fact, the OH-groups in water are so close to each other that not only dipole-dipole, but also dipole-quadrupole, quadrupole-quadrupole, and higher-order interactions will become important, as well as mechanical anharmonic coupling [140]. The Förster expression hinges on the fact that these other interactions decrease much more rapidly with increasing distance than the dipole-dipole interaction, and thus become less important. At the short distances occurring in H_2O this is of course not the case, and a more general treatment of the intermolecular coupling is necessary to accurately describe this liquid.

The process of orientational scrambling can also be described in terms of delocalized excitations instead of excitation transfer. As Förster has remarked [141], the two descriptions are complementary, the former being more appropriate to describe stationary states of the system, the latter to describe non-stationary states. The eigenstates of liquid H_2O will be states in which the OH-stretch excitation is delocalized over many molecules [142]. These delocalized states are nondegenerate because of the intermolecular coupling term in the Hamiltonian. Optical excitation of the system with a linearly polarized pulse will result in an excited-state wave function that is a superposition of many of these eigenstates, such that the resulting excited-state absorption has a maximum in the polarization direction of the excitation pulse. The loss of coherence between the contributing eigenstates and homogeneous dephasing processes will rapidly render the excited-state absorption isotropic.

8.4 Conclusions

We have studied the decay of the rotational anisotropy of the OH-stretch excited-state absorption in water as a function of the concentration of OH-oscillators. In HDO:D_2O, the decay rate increases significantly with increasing HDO concentration. This constitutes evidence for rapid intermolecular transfer of the OH-stretch excitation. We found that the transfer can be well described quantitatively by a dipole-dipole energy (Förster) transfer mechanism.

In H_2O, the orientational scrambling occurs instantaneously. This is caused by both intramolecular redistribution of the OH-stretch excitation over the symmetric and asymmetric OH-stretch modes of the H_2O molecules, which reduces the anisotropy to a quarter of its initial value, and very rapid intermolecular transfer of the OH-stretch excitation between the H_2O molecules.

9 Infrared photon echoes with parametrically generated incoherent light

9.1 Introduction

Vibrational lineshapes in the condensed phase contain information on the interactions of molecular vibrations with their environment [143]. In a crude approximation, the vibrational linewidth is caused by mechanisms referred to as inhomogeneous broadening (a distribution of transition frequencies which can be regarded as static on the time scale of the experiment) and homogeneous broadening (frequency fluctuations faster than the time scale of the experiment). In order to study vibrational dynamics, it is essential to separate the homogeneous and inhomogeneous contributions to the lineshape. Recently, nonlinear spectroscopic techniques have been employed in order to separate the two contributions. Raman-active vibrations have been studied with Raman-echo spectroscopy [144, 145], while infrared-active vibrations have been investigated with transient hole-burning [24, 26] and infrared photon-echo spectroscopy [36, 146, 147]. The echo techniques probe the homogeneous dephasing in the time domain, and provide an elegant means of determining the homogeneous dephasing time T_2.

Since dephasing of molecular vibrations in the condensed phase typically occurs on picosecond and subpicosecond time scales, it would seem that in order to perform nonlinear time-resolved studies, infrared pulses of the same or shorter duration are required. Moreover, high intensities are needed, as infrared absorption cross sections are generally rather small. Until recently, such pulses were difficult to generate, and for a long time the only infrared photon-echo experiments reported were performed on the CO-stretch mode (famous for its large absorption cross section), using picosecond infrared pulses generated with a free-electron laser [36, 146, 148].

Morita and Yajima [149] were the first to realize that the time resolution in a time-delayed four-wave mixing experiment is not determined by the pulse duration, but rather by the coherence time of the electromagnetic field, which, in case of an incoherent light source, can be shorter by several orders of magnitude [150]. The main advantage of spectroscopy with incoherent pulses is that the same time-resolution can be obtained as with coherent pulses of the same bandwidth, but that the incoherent light is usually much easier to generate. Up to now, photon-echo studies with incoherent light have mainly been done in the visible region, in particular by employing broadband dye lasers [150–153]. But the incoherent light need not even be generated with a laser: femtosecond photon-echo experiments can be performed with such diverse light sources as synchrotron radiation [154], a light-emitting diode [155], and even an incandescent lamp [156]. In the latter particularly amusing photon-echo study, a time-resolution of 150 fs was achieved using a light bulb.

In this Chapter, we present the first incoherent photon-echo experiments on a vibrational transition. In these experiments, subpicosecond time-resolution was obtained using mid-infrared pulses with a duration of 20 ps, which were generated by means of parametric generation and amplification.

9.2 Experiment

9.2.1 Experimental setup

The setup laser used to generate the incoherent mid-infrared pulses is shown in Fig. 9.1. Parametric generation and amplification are used to downconvert the fundamental output of a commercial mode-locked Nd:YAG laser (35 ps pulses at a repetition rate of 10 Hz). The parametric downconversion takes place in three $LiNbO_3$ crystals (5 cm long, optical axis cut at 47.1°). The first crystal is pumped with approximately 10 mJ and generates signal and idler via type I phase matching. The signal generated in the first crystal is fur-

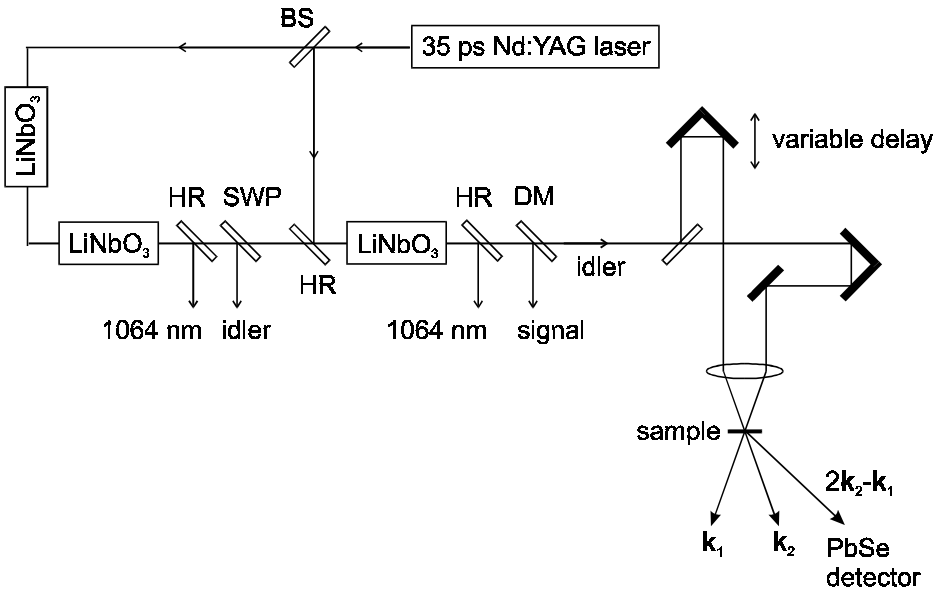

FIGURE 9.1. Parametric generation and amplification setup to generate incoherent idler pulses (left part), and four-wave mixing setup (right part). BS: beamsplitter for 1064 nm; HR: 1064 nm high-reflective mirrors; SWP: short-wave pass filter; DM: dichroic mirror to separate signal and idler.

ther amplified in the second crystal using the remaining pump. The second crystal is at a distance of 2 m from the first to ensure that only the signal collinear with the pump is amplified. After the second crystal, idler and pump are blocked, and the signal is further amplified in the third $LiNbO_3$ crystal with a fresh pump pulse of 8 mJ. The mid-infrared pulses generated in this process have a duration of approximately 20 ps (FWHM), and an energy of 100 μJ. The center frequency is tunable from 2500 to 6900 cm^{-1}, and the bandwidth is 20 cm^{-1} at 3450 cm^{-1}. The parametrically generated light is highly temporally incoherent. The incoherence is due to the process of parametric generation, which is

essentially formed by the amplification of zero-point fluctuations of the electromagnetic field [39].

The four-wave mixing setup is also shown in Fig. 9.1. The infrared beam is split and one part is sent through a variable delay. The two beams are focused into the sample by a 100 mm CaF_2 lens in slightly different directions $\mathbf{k}_1$ and $\mathbf{k}_2$ making an angle of approximately 5°. The FWM signal in the direction $2\mathbf{k}_2 - \mathbf{k}_1$ is detected as a function of delay using a PbSe detector.

9.2.2 SAMPLES

Since infrared hole-burning studies have shown that the OH-stretch band can be strongly inhomogeneously broadened in hydrogen bonded systems [24, 26], we have applied the method to the OH-stretch mode of a methanol solution and of a hydrogen-bonded polymer film. The methanol was studied in a 100 μm thick sample consisting of a 2.2 mol/l solution of methanol in bromoform at room temperature. The hydrogen bonding of the methanol molecules gives rise to a broad OH stretch band centered at $\sim$3330 cm^{-1}, which is identical to that of ethanol shown in Fig 3.1.

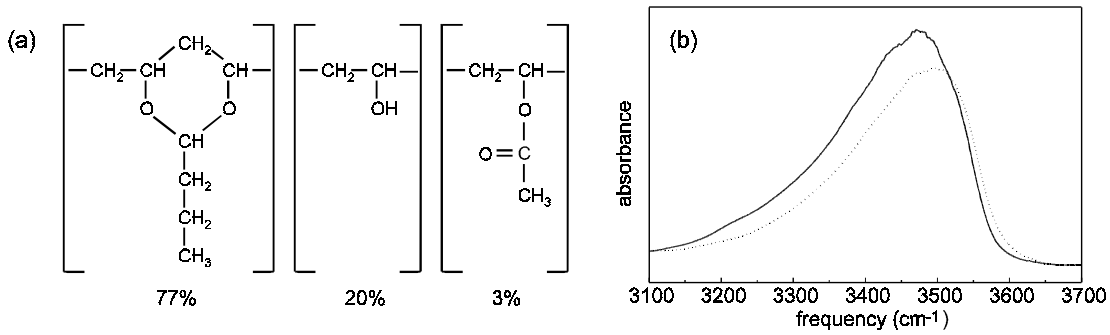

FIGURE 9.2. (a) Chemical structure of poly(vinylbutyral). (b) Infrared absorption spectra of poly(vinylbutyral) from 3100 to 3700 cm^{-1} at room temperature (dotted line) and at 15 K (solid line).

The polymer sample is a terpolymer consisting of 77% poly(vinylbutyral), 20% poly(vinylalcohol) and 3% poly(vinylacetate) (chemical structure shown in Fig. 9.2(a)). The OH-groups in the polymer are hydrogen-bonded, and the OH-stretch band, shown in Fig. 9.2(b), is known to be strongly inhomogeneously broadened [24]. A layer of approximately 50 μm of this polymer was deposited on a sapphire plate following the procedure described by Graener *et al* [24]. The sapphire plate was mounted on the cold finger of a closed-cycle helium cryostat.

9.2.3 PHYSICAL MECHANISM OF THE PHOTON ECHO WITH INCOHERENT LIGHT

In the condensed phase, molecules in different environments often have different resonance frequencies ω_0. This leads to inhomogeneous broadening of the spectral line, determined by a distribution function $g(\omega_0)$ of resonance frequencies. If such an inhomogeneously broadened system is coherently excited, the macroscopic polarization will

rapidly decay as molecules with different resonance frequencies start to run out of phase. The dephasing of the individual molecules, characterized by the homogeneous dephasing time T_2, often takes place on a much slower time scale. Photon-echo spectroscopy provides a means of determining the homogeneous dephasing time of predominantly inhomogeneously broadened systems. In the remainder of this section, we will first discuss the physical mechanism of the coherent ('ordinary') photon echo, and then focus on the somewhat more complicated mechanism of the photon echo generated with incoherent light.

In a coherent two-pulse photon-echo experiment, the first pulse (with wavevector $\mathbf{k}_1$) creates a macroscopic polarization in the resonant medium, which rapidly decays due to the inhomogeneous broadening. Provided the delay τ between the first and second pulse is shorter than the homogeneous dephasing time T_2, the polarization of each subensemble with a particular transition frequency, which decays as e^{-t/T_2}, will still exist at the moment the second pulse arrives. The second pulse (with wavevector $\mathbf{k}_2$) then generates population gratings for each transition frequency (with grating vector $\mathbf{k}_2 - \mathbf{k}_1$), which are spatially shifted with respect to each other because of the phase differences accumulated during the delay time. The second pulse generates from each grating a third-order polarization, whose initial phase is determined by the spatial shift of the grating, and which oscillates at the appropriate transition frequency. At time $t = 2\tau$, all the third-order polarization components interfere constructively to form a macroscopic polarization in the direction $2\mathbf{k}_2 - \mathbf{k}_1$, which generates the photon echo. The decay of the intensity of the echo with increasing delay τ is determined by the homogeneous dephasing which takes place during the time interval 2τ. This homogeneous dephasing causes the third-order polarization to decay as $e^{-2\tau/T_2}$, and hence the echo intensity as $e^{-4\tau/T_2}$.

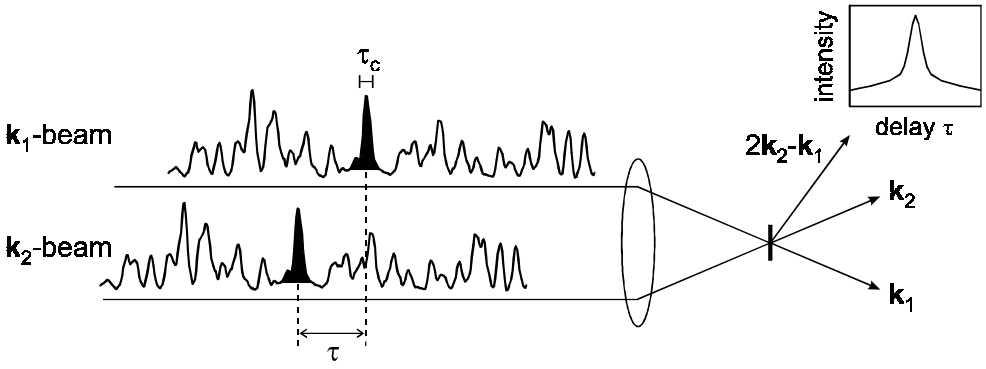

FIGURE 9.3. Schematic picture of an incoherent two-pulse photon-echo experiment. The two beams $\mathbf{k}_1$ and $\mathbf{k}_2$ are time-delayed copies of each other, and can be considered to consist of a train of 'subpulses', each of which has a length of approximately the coherence time τ_c. When the dephasing is instantaneous, the time-integrated signal consists of a broad background signal and a sharp peak centered at delay zero, with a width of approximately τ_c.

The time resolution of photon-echo spectroscopy with incoherent pulses is determined by the coherence time τ_c, which is approximately the inverse of the spectral bandwidth, and can be orders of magnitude shorter than the duration of the pulses. In order to understand how this time resolution arises, it is convenient to view the incoherent pulse as a

train if short transform-limited 'subpulses', each of which has a different phase and amplitude, and an average duration of τ_c [157]. The $\mathbf{k}_2$-beam is a time-delayed copy of the $\mathbf{k}_1$-beam, see Fig. 9.3. A subpulse in the beam $\mathbf{k}_1$ and a subpulse in the beam $\mathbf{k}_2$ can generate an excited-state population grating in the same way as in a coherent photon echo experiment, provided the delay between the subpulses is less than T_2. All subpulses in $\mathbf{k}_2$ following and including the one that created the grating, can generate a third-order polarization, and hence an echo signal, from this grating (provided the grating, which decays as e^{-t/T_1}, still exists). When the delay τ is less than T_2, excited-state population gratings are generated by pairs of correlated subpulses. This means that the total grating amplitude will grow linearly with the number of contributing subpulses. The third-order polarization generated from this grating constitutes the coherent contribution to the signal ('coherence spike'), and its decay with increasing delay is determined mainly by the homogeneous dephasing time T_2 and the coherence time τ_c. Excited-state population gratings can also be generated by pairs of uncorrelated subpulses. In this case, there will be a random phase difference between the two pulses that generate the grating, and each grating generated by a pair of uncorrelated subpulses will be displaced randomly with respect to the others. Hence, in this case the grating amplitude will only grow as the square root of the number of contributing subpulses. The third-order polarization generated from this grating gives rise to an incoherent background contribution to the echo signal. This incoherent background signal is nearly independent of delay, its intensity being determined mainly by the temporal overlap of the average-intensity envelopes of the incoherent pulses.

The fact that the coherence time is much shorter than the pulse duration renders the photon echo generated with incoherent light similar to an accumulated photon echo [158, 159]. The subpulses in the incoherent pulse $\mathbf{k}_2$ generate the echo from a grating that is the sum of the gratings generated by the previous pairs of correlated subpulses in the incoherent pulses (within T_1). The accumulation of the grating amplitude during the incoherent pulse results in an echo signal that can be much larger than could be generated with a pair of coherent pulses of the same length and intensity as the subpulses in the incoherent pulse train.

9.3 Results

9.3.1 METHANOL

Figure 9.4 represents a scan recorded in methanol, obtained by monitoring the time-integrated intensity in the direction $2\mathbf{k}_2 - \mathbf{k}_1$ as a function of delay τ, at an excitation frequency of 3330 cm^{-1}. The signal consists of a coherence spike with a width of approximately 1 ps superposed on a broad background with a width of approximately 20 ps. This can be understood in terms of the discussion in the previous section. For small delays, the subpulses in the two incoherent pulses $\mathbf{k}_1$ and $\mathbf{k}_2$ are strongly correlated and generate a strong echo signal. This signal forms the coherence spike and its decay with increasing delay reflects the homogeneous dephasing if $T_2 > \tau_c$ [149]. In Figure 9.4, which has been obtained by excitation of the OH-stretch mode of methanol at room temperature, the coherence spike is symmetric around delay zero. This indicates that under these circum-

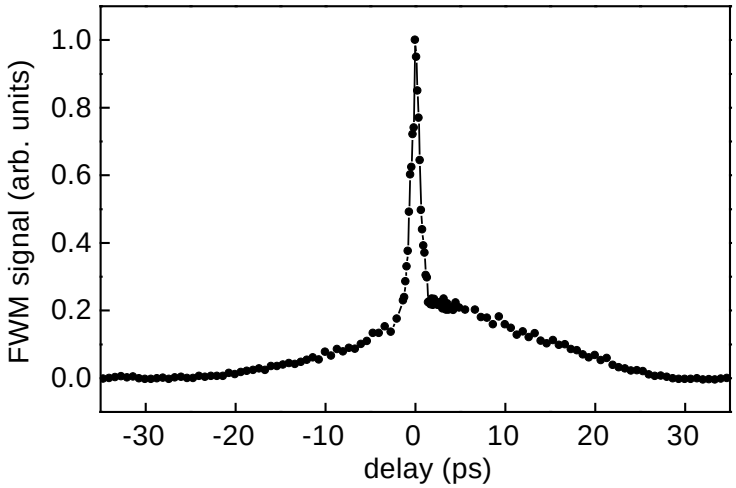

FIGURE 9.4. Integrated four-wave mixing intensity as a function of delay between $\mathbf{k}_1$ and $\mathbf{k}_2$, at an excitation wavelength of 3.0 μm in a 100 μm thick sample consisting of a 2.2 mol/l solution of methanol in bromoform at room temperature. The signal consists of a symmetric coherence spike superposed on a broad background.

stances the homogeneous dephasing time T_2 is much shorter than τ_c, and that the width of the coherence spike is determined only by τ_c. Note that the coherence time is about 20 times smaller than the pulse duration, demonstrating clearly that the pulses are incoherent. For delays much larger than τ_c and T_2, the signal is generated by uncorrelated subpulses and depends mainly on the overlap of the two pulse envelopes (see previous section). This signal forms the broad incoherent background, which can be asymmetric if the excited state lifetime T_1 is of the order of the the width of the pulse intensity envelope or longer. In that case the background signal is due to subpulses in $\mathbf{k}_2$ that diffract from a grating which is the sum of the gratings created by all previous pairs of uncorrelated subpulses in the pulse envelope. As this sum is largest at the end of the pulse envelope, the maximum of the background signal will occur at positive delay, as is observed in Figure 9.4. If T_1 is much shorter than the width of the pulse intensity envelope, the background signal will represent a third-order autocorrelation function of this envelope (see below, Eq. (9.14)).

9.3.2 POLY(VINYLBUTYRAL)

Delay scans of the coherence peak at room temperature and 15 K are shown in Fig. 9.5. At room temperature, the FWM signal is symmetric around $\tau = 0$, implying that at this temperature the homogeneous dephasing time is much shorter than the coherence time of the field. In this case, the observed signal is determined only by the correlation function of the electromagnetic field. At low temperature the signal becomes asymmetric, indicating that T_2 is at least of the order of τ_c. Furthermore, the maximum shifts to a larger delay time, which implies that the induced polarization lasts long enough to build up during a subpulse, confirming that T_2 is larger than τ_c. Note that the linear absorption spectrum (shown in Fig. 9.2) hardly changes going from room temperature to 15 K.

From the measured data at 15 K (Fig. 9.5) the homogeneous dephasing time at this temperature can be derived, but this is somewhat less straightforward than in the case of a

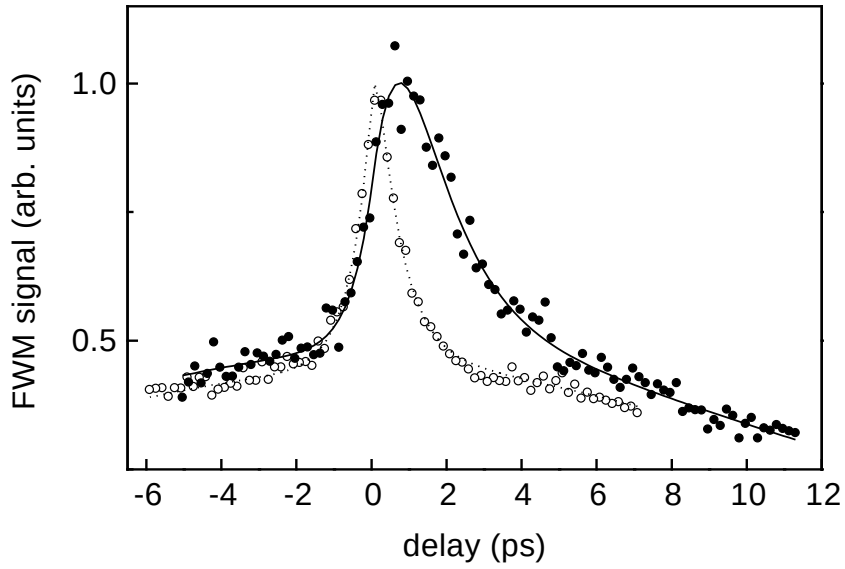

FIGURE 9.5. Integrated four-wave mixing intensity as a function of delay between pulses with wavevectors $\mathbf{k}_1$ and $\mathbf{k}_2$, at an excitation frequency of 3450 cm^{-1} at room temperature (open points) and 15 K (solid points). At low temperature the signal becomes asymmetric, which indicates that T_2 is larger than the the coherence time of the field. The lines have been calculated using the model described Section 9.4.

photon echo generated with coherent pulses. An important difference is that whereas the observed decay of the signal generated with coherent light is determined by a single time constant T_2 (which in itself depends on the pure dephasing rate and T_1), in the present case the observed decay is determined by both the values of T_2 and T_1 [149]. This is due to the occurrence of scattering events involving three subpulses: a subpulse p in $\mathbf{k}_2$ may scatter off a grating created by its correlated subpulse p' in $\mathbf{k}_1$ and an arbitrary subpulse q in $\mathbf{k}_2$, provided q occurs between p' and p. The FWM signal due to such processes will depend both on the decay rate of the polarization and the decay rate of the grating amplitude, resulting in a delay dependence determined by both T_1 and T_2 [149]. Hence, if T_1 is of the order of T_2, a detailed quantitative analysis is needed to obtain T_2 from incoherent photon-echo spectroscopy.

9.4 Quantitative description

To describe the data quantitatively, we follow the analysis by Morita and Yajima [149], which describes the four-wave mixing interaction of a two-level system with the incoherent field using a third-order perturbation approximation for the density matrix. It will be assumed that the material response can be described by the Bloch (T_1, T_2) model (the calculation can easily be modified to cover more complicated situations), and that $\tau_{\text{pulse}} \gg T_1, \tau_c, T_2$. It is also assumed that the incoherent field amplitude is a Gaussian process. This assumption is rigorously justified, since quantum-optical calculations have shown that parametrically generated light is indeed a Gaussian process [160].

This section is organized as follows: first, an expression for the FWM signal will

be obtained for arbitrary T_2, T_1 and coherence function $f(t)$. The case of instantaneous material response, where the FWM signal is determined by the coherence function $f(t)$ alone, will then be obtained by taking the limit $T_2 \to 0$. Comparing this limit to the room temperature FWM signal, we obtain the second-order correlation function $f(t)$ of the parametrically generated light. With this $f(t)$ we then calculate the FWM signal for finite T_2 and compare the result to the measurement at low temperature.

Following Ref. [149], we write the total electric field as the sum of two incoherent fields:

$$E(\mathbf{r},t) = \tilde{E}(t+\tau)e^{i(\mathbf{k}_1\cdot\mathbf{r}-\omega(t+\tau))} + \tilde{E}(t)e^{i(\mathbf{k}_2\cdot\mathbf{r}-\omega t)} + \text{c.c.}, \tag{9.1}$$

with ω the central frequency of the field, and τ the delay between the two fields. The two fields with wavevectors $\mathbf{k}_1$ and $\mathbf{k}_2$ are time-delayed replicas, since they are generated from the same field using a beamsplitter. The amplitudes

$$\tilde{E}(t) = \varepsilon(t)R(t) \tag{9.2}$$

are products of the pulse envelope function $\varepsilon(t)$ and the stationary complex circular Gaussian random process $R(t)$ which describes the random fluctuations of the field [161], with [149]

$$\begin{gathered} \langle R(s)\rangle = 0, \\ \langle R(s)R(s+t)\rangle = \langle R^*(s)R^*(s+t)\rangle = 0, \\ \langle R^*(s)R(s+t)\rangle = f(t), \end{gathered} \tag{9.3}$$

where $f(t)$ is called the second-order moment function. The random process is normalized such that

$$f(0) = \langle R(t)R^*(t)\rangle = 1. \tag{9.4}$$

The FWM intensity can now be calculated using a third-order perturbation approximation for the density matrix. In this approach, the third-order polarization in the direction $2\mathbf{k}_2 - \mathbf{k}_1$ is given by [149]:

$$P^{(3)}(\mathbf{r},t) = \tilde{P}^{(3)}(\mathbf{r},t)e^{-i\omega t} + \text{c.c.}, \tag{9.5}$$

$$\tilde{P}^{(3)}(\mathbf{r},t) = N\mu\int_0^\infty d\omega_0 \tilde{\rho}^{(3)}(\mathbf{r},t,\omega_0)g(\omega_0), \tag{9.6}$$

where $g(\omega_0)$ represents the inhomogeneous distribution of oscillator frequencies, N is the number density of oscillators, μ the transition dipole moment (assumed to be real), and $\tilde{\rho}^{(3)}(\mathbf{r},t)$ the component in the direction $2\mathbf{k}_2 - \mathbf{k}_1$ of the third-order off-diagonal matrix element of the density matrix. By perturbative solution of the optical Bloch equations it can be shown that [149]:

$$\begin{aligned} \tilde{\rho}^{(3)}(\mathbf{r},t) = {} & -2i\left(\frac{\mu}{\hbar}\right)^3 \exp\{i[(2\mathbf{k}_2-\mathbf{k}_1)\cdot\mathbf{r}-\omega t]\} \\ & \times \int_{-\infty}^{t} dt_1 \int_{-\infty}^{t_1} dt_2 \int_{-\infty}^{t_2} dt_3 \ \exp\{-(t_1-t_2)/T_1 - (t-t_1+t_2-t_3)/T_2\} \\ & \{\tilde{E}(t_1)\tilde{E}(t_2)\tilde{E}^*(t_3+\tau)\exp[-i(\omega_0-\omega)(t-t_1-t_2+t_3)] \\ & + \tilde{E}(t_1)\tilde{E}^*(t_2+\tau)\tilde{E}(t_3)\exp[-i(\omega_0-\omega)(t-t_1+t_2-t_3)]\}. \end{aligned} \tag{9.7}$$

The observed FWM signal is the time-integrated squared modulus of this third-order polarization, statistically averaged over the fluctuations of $R(t)$:

$$\int_{-\infty}^{\infty} dt\ \langle |\tilde{P}^{(3)}(\mathbf{r},t)|^2 \rangle, \tag{9.8}$$

where the brackets $\langle \ldots \rangle$ denote a statistical average over $R(t)$. Substitution of Eq. (9.7) into (9.6) and (9.6) into (9.8) yields an expression for the FWM signal [149]. This expression can be substantially simplified for a strongly inhomogeneously broadened system. In that case, which often applies (in particular in the present experiment), the width of the inhomogeneous distribution is much larger than T_2^{-1} and than the width of the pulse spectrum, and we can set $g(\omega_0)$ constant in Eq. (9.6), and after substitution of this simplified expression for $P^{(3)}(\mathbf{r},t)$ into Eq. (9.8) one obtains a FWM signal proportional to

$$\begin{aligned} S(\tau) = C(\tau) \int_{-\infty}^{\tau} dt_1 \int_{-\infty}^{t_1} dt_2 \int_{-\infty}^{\tau} ds_1 \int_{-\infty}^{s_1} ds_2 \\ \langle R(t_1)R(t_2)R^*(t_1+t_2)R^*(s_1)R^*(s_2)R(s_1+s_2)\rangle \\ \times \exp\left(-\frac{t_1-t_2+s_1-s_2}{T_1} + \frac{2t_1+2s_1-4\tau}{T_2}\right), \end{aligned} \tag{9.9}$$

with

$$C(\tau) = \int_{-\infty}^{\infty} dt\ |\varepsilon(t)|^4 |\varepsilon(t-\tau)|^2 \tag{9.10}$$

the third-order autocorrelation of the average pulse intensity envelope $|\varepsilon(t)|^2$. Since $\tau_{\text{pulse}} \gg T_1, \tau_c, T_2$, this is a slowly varying function compared to the other time scales of the experiment. We now use the Gaussian property of $R(t)$ to factorize the sixth-order correlation function:

$$\begin{aligned} &\langle R(t_1)R(t_2)R^*(t_1+t_2)R^*(s_1)R^*(s_2)R(s_1+s_2)\rangle = \\ &\quad f^*(t_2)\,f(t_2-s_1)\,f(s_1) + f^*(t_2)\,f(t_2-s_2)\,f(s_2) + f(t_1-s_1)\,f^*(t_1)\,f(s_1) \\ &\quad + f(t_1-s_1)\,f(t_2-s_2)\,f(s_1+s_2-t_1-t_2) + f(t_1-s_2)\,f^*(t_1)\,f(s_2) \\ &\quad + f(t_1-s_2)\,f(t_2-s_1)\,f(s_1+s_2-t_1-t_2). \end{aligned} \tag{9.11}$$

Substitution of Eq. (9.11) into (9.9) yields an expression for the FWM signal in terms of T_2, T_1, and the second-order moment $f(t)$ only. It applies to temporally incoherent Gaussian light with arbitrary second-order moment function $f(t)$.

In the limit of instantaneous optical dephasing, we have $T_2 \ll \tau_c$, and equation (9.9) is easily shown to reduce to [162]

$$S(\tau) = C(\tau)\left[\text{const.} + |f(\tau)|^2\right]. \tag{9.12}$$

This means that if the dephasing is instantaneous, the FWM signal as a function of delay τ is determined by the coherence properties of the light only, and is given by $|f(\tau)|^2$ (neglecting the constant background signal and the delay dependence of the slowly varying function $C(\tau)$). This can be understood as follows: the two beams $\mathbf{k}_1$ and $\mathbf{k}_2$ interfere to

create a transient population grating $\mathbf{k}_2 - \mathbf{k}_1$, from which the beam $\mathbf{k}_2$ is diffracted in the direction $2\mathbf{k}_2 - \mathbf{k}_1$. If the dephasing is instantaneous, the grating amplitude is determined only by the coherence of $\mathbf{k}_1$ and $\mathbf{k}_2$ and is given by $f(\tau)$. The amplitude of the light diffracted from the grating is proportional the grating amplitude, and hence the diffracted intensity will be proportional to $|f(\tau)^2|$.

Thus when the dephasing is instantaneous, the FWM signal is the square modulus of the second-order moment of the incoherent light. This means that we can use the room temperature FWM signal (where $T_2 \ll \tau_c$) to obtain $f(t)$. As seen in Fig. 9.5, the room temperature signal is well described by a double-sided exponential. This means that $f(t)^2$, and hence $f(t)$, is a double-sided exponential, and that for the parametrically generated light we can assume

$$f(t) = \exp(-|t/\tau_c|), \tag{9.13}$$

with the coherence time τ_c to be determined from the room temperature measurement.

We now want to obtain the FWM signal (Eq. (9.9)) for a second-order moment function of the form (9.13). In the literature, explicit expressions are given for the incoherent FWM signal are given for various limiting cases of the relative magnitudes of τ_c, T_1 and T_2 ($T_1 \gg T_2, \tau_c$ in Ref. [162], $T_1, T_2 \gg \tau_c$ in Ref. [149]). In the present case however, T_1, T_2 and τ_c are all of the same order of magnitude, and no simplifying assumptions can be made except that the pulse duration τ_{pulse} is much larger than the other time constants involved.

Fortunately, with some effort, the FWM signal of Eq. (9.9) can be calculated analytically without any assumptions concerning the relative magnitude of τ_c, T_2 and T_1, if $f(t)$ is of the form (9.13). Performing the multiple integration in Eq. (9.9), we find:

$$S(\tau) = C(\tau)\,(S_1(\tau) + S_0)\,, \tag{9.14}$$

with S_0 the delay-independent background FWM signal discussed in Section 9.2.3, and $S_1(\tau)$ the delay-dependent FWM signal, given by

$$S_1(\tau) = \frac{(2{\gamma_1}^3 + 2(1+\gamma_2) + 4{\gamma_1}^2(2+\gamma_2) + \gamma_1(7+5\gamma_2))\,e^{2x}}{{\gamma_1}^2(1+\gamma_1)(2+\gamma_1)(1+\gamma_2)(1+2\gamma_2)(2+\gamma_1+2\gamma_2)} \quad \text{if } \tau < 0,$$

$$\begin{aligned}
S_1(\tau) = \Bigg\{ & \frac{24e^{2(-\gamma_1+\gamma_2)x}(-e^{\gamma_1 x} + e^{2\gamma_2 x})}{(4-5{\gamma_1}^2+{\gamma_1}^4)(\gamma_1-2\gamma_2)^2} + \frac{4(3-3e^{-2\gamma_1 x+4\gamma_2 x})}{(4-5{\gamma_1}^2+{\gamma_1}^4)(\gamma_1-2\gamma_2)^2} \\
& + \frac{8(-1+e^{-(2+\gamma_1-4\gamma_2)x})}{(\gamma_1-2)\gamma_1(2+\gamma_1)(2+\gamma_1-4\gamma_2)(\gamma_1-2\gamma_2)} \\
& + \frac{4-4e^{-(2+\gamma_1-4\gamma_2)x}}{(-2+\gamma_1)\gamma_1(2+\gamma_1)(2+\gamma_1-4\gamma_2)(-1+\gamma_2)} \\
& + \frac{4e^{-\gamma_1 x+2\gamma_2 x}(-1+e^{2(-1+\gamma_2)x})}{(-2+\gamma_1)\gamma_1(2+\gamma_1)(\gamma_1-2\gamma_2)(-1+\gamma_2)} \\
& + \frac{4e^{2(-1+\gamma_2)x}(-1+e^{-\gamma_1 x+2\gamma_2 x})}{(\gamma_1-2)\gamma_1(2+\gamma_1)(\gamma_1-2\gamma_2)(\gamma_2-1)} + \frac{e^{2(-1+\gamma_2)x}(-1+e^{2\gamma_2 x})}{(\gamma_1-2)\gamma_1(\gamma_2-1)\gamma_2} \\
& - \frac{2(-1+e^{-\gamma_1 x+2\gamma_2 x})}{\gamma_1(2+\gamma_1)(\gamma_1-2\gamma_2)(1+\gamma_2)} + \frac{2(-1+e^{-\gamma_1 x+2\gamma_2 x})}{(-4+{\gamma_1}^2)(\gamma_1-2\gamma_2)(1+\gamma_2)}
\end{aligned}$$

$$
\begin{aligned}
&+\frac{-1+e^{2(-1+\gamma_2)x}}{(-4+{\gamma_1}^2)(-1+\gamma_2)(1+\gamma_2)}+\frac{1}{\gamma_1(2+\gamma_1)\gamma_2(1+\gamma_2)}\\
&-\frac{2(-1+e^{(-2+4\gamma_2)x})}{(\gamma_1-2)(\gamma_1-1)\gamma_1(\gamma_1-2\gamma_2)(2\gamma_2-1)}-\frac{-1+e^{(4\gamma_2-2)x}}{(\gamma_1-2)\gamma_1(\gamma_2-1)(2\gamma_2-1)}\\
&-\frac{2}{\gamma_1(1+\gamma_1)(2+\gamma_1)(\gamma_1-2\gamma_2)(1+2\gamma_2)}-\frac{1}{\gamma_1(2+\gamma_1)\gamma_2(1+2\gamma_2)}\\
&+\frac{4e^{-\gamma_1 x+2\gamma_2 x}(-1+e^{(-2+\gamma_1+2\gamma_2)x})}{(-2+\gamma_1)(-1+\gamma_1)\gamma_1(\gamma_1-2\gamma_2)(-2+\gamma_1+2\gamma_2)}\\
&+\frac{4(-1+e^{-\gamma_1 x+2\gamma_2 x})}{\gamma_1(1+\gamma_1)(\gamma_1-2\gamma_2)(2+\gamma_1+2\gamma_2)}-\frac{4(-1+e^{-\gamma_1 x+2\gamma_2 x})}{\gamma_1(2+\gamma_1)(\gamma_1-2\gamma_2)(2+\gamma_1+2\gamma_2)}\\
&+\frac{4}{\gamma_1(1+\gamma_1)(2+\gamma_1)(\gamma_1-2\gamma_2)(2+\gamma_1+2\gamma_2)}\\
&+\frac{e^{2\gamma_2 x}-e^{4\gamma_2 x}+(3e^{2x}-2e^{4\gamma_2 x})\gamma_2+e^{2\gamma_2 x}(-4+e^{2\gamma_2 x}){\gamma_2}^2+2e^{4\gamma_2 x}{\gamma_2}^3}{e^{2x}{\gamma_1}^2(\gamma_2-5{\gamma_2}^3+4{\gamma_2}^5)}\\
&-\gamma_1^{-1}\left[\frac{-4e^{2(-1+\gamma_2)x}(-1+e^{-\gamma_1 x+2\gamma_2 x})}{\gamma_1(2+\gamma_1)(\gamma_1-2\gamma_2)(-1+\gamma_2)}-\frac{e^{2(-1+\gamma_2)x}(-1+e^{2\gamma_2 x})}{\gamma_1(-1+\gamma_2)\gamma_2}\right.\\
&+\frac{-1+e^{2(-1+\gamma_2)x}}{(-2+\gamma_1)(-1+\gamma_2)\gamma_2(1+\gamma_2)}+\frac{-1+e^{(-2+4\gamma_2)x}}{(-1+\gamma_2)\gamma_2(-1+2\gamma_2)(-2+\gamma_1+2\gamma_2)}\\
&+\frac{1}{\gamma_2(1+\gamma_2)(1+2\gamma_2)(2+\gamma_1+2\gamma_2)}+\frac{e^{-2x+2\gamma_2 x}}{2+\gamma_1-2{\gamma_2}^2-\gamma_1{\gamma_2}^2}\\
&+\frac{8(-1+e^{-\gamma_1 x+2\gamma_2 x})({\gamma_1}^2+2\gamma_1\gamma_2+4(-3+{\gamma_2}^2))}{(-2+\gamma_1)(2+\gamma_1)(\gamma_1-2\gamma_2)(-1+\gamma_2)(1+\gamma_2)(-2+\gamma_1+2\gamma_2)(2+\gamma_1+2\gamma_2)}\\
&\left.+\frac{1}{(2+\gamma_1)(-\gamma_2+{\gamma_2}^3)}\right]\Bigg\}\frac{e^{-4\gamma_2 x}}{2}\quad\text{if } \tau>0, \qquad (9.15)
\end{aligned}
$$

where $\gamma_1=\tau_c/T_1$, $\gamma_2=\tau_c/T_2$ and $x=\tau/\tau_c$. The complexity of this expression is a result of the fact that in the multiple integration the integrated volume has to be divided into a large number of subvolumes depending on the sign of the arguments of the $f(t)$'s occurring in the integrand. The integration over each subvolume is in itself straightforward. The expression (9.15) is continuous and differentiable in $\tau=0$. We checked its correctness by taking the limit $\tau_c\to 0$. In that case (9.14) exactly agrees with the FWM signal for $f(t)=\delta(t)$, which has previously been calculated by Morita and Yajima [149].

We now describe the experimental results in terms of Eq. (9.14). First, we will use the room temperature data (for which $T_2 \ll \tau_c$) to determine the coherence time τ_c. To calculate $C(\tau)$, we use the intensity envelope $|\varepsilon(t)|^2$, which is given by a Gaussian with a FWHM of 20 ps (as determined from an autocorrelation trace). The dashed curve in Fig. (9.5) represents a least-squares fit to the room temperature data using Eq. (9.14) and literature values [24] of $T_1=5$ ps and $T_2=0.2$ ps. The good agreement between the data and the calculation justifies the use of Eq. (9.13). The fit to the room temperature yields a value of $\tau_c=1.13\pm0.07$ ps for the coherence time. Therefore, at room temperature we indeed have $T_2\ll\tau_c$, and instead of Eq. (9.14) one could also use (9.12). As was discussed

at the end of Section 9.3.1, the decay of the echo signal is determined by both T_1 and T_2.

With τ_c known, the data at 15 K can be used to determine the value of T_2 at this temperature. We did this by means of a least-squares fit of Eq. (9.14) to the data points, using the literature value for T_1 at 300 K. It might be that at 15 K the value of T_1 is slightly larger than at 300 K, although no temperature dependence of this value has been observed over a temperature range from 80 to 300 K [25]. Simulations using Eq. (9.14) show that increasing T_1 by several ps has a negligible effect on the value obtained for T_2. From the fit a value of $T_2 = 2.8 \pm 0.3$ ps was obtained (solid curve in Fig. 9.5), which implies that at 15 K the homogeneous dephasing time is an order of magnitude larger than at room temperature. Furthermore, the measured value of T_2 corresponds to a homogeneous linewidth of $\sim$4 cm^{-1}, which implies that at 15 K the homogeneous linewidth is nearly two orders of magnitude smaller than the width of the absorption band (shown in Fig. 9.2).

Theoretical analysis has shown that photon-echo experiments performed with incoherent light can be sensitive to spectral diffusion [159, 163]. This means that the value obtained for T_2 might in principle contain a contribution due to spectral diffusion, although in the present system the influence of slow frequency-fluctuations on the signal is limited due to the rapid decay of the excited state population [24].

9.5 Conclusions

To summarize, we have presented a simple method to generate infrared photon echoes using a standard setup for parametric downconversion. The time resolution of the experiment is determined by the coherence time of the infrared pulses, and is short enough to enable the investigation of vibrational dephasing in the condensed phase. The technique has been applied to a hydrogen-bonded polymer, and yielded an accurate determination of the homogeneous dephasing time of the OH-stretch vibration of this polymer. With the setup depicted in Fig. 9.1, any vibration in the 1.5–4 μm wavelength region can be studied in the same way. The accumulative nature of the incoherent photon echo makes it possible to study molecular vibrations with small absorption cross sections, notably the OH-, CH-, and NH-stretch modes, which are of great chemical and biological importance.

The method of incoherent four-wave mixing is a very powerful one: it enables photon echo studies with high time resolution in wavelength regions where coherent ultrashort pulses are not yet available, or difficult to generate. In the visible wavelength region, it has not only be used to study dephasing of optical transitions, but also for the study of orientational [164] and population relaxation [165]. Similar experiments can be performed on vibrational transitions using the setup shown in Fig. 9.1. The most important disadvantage of the incoherent FWM method is that the delay between only two of the three fields that create the third-order polarization is known. That this renders the interpretation more complicated, becomes clear when one compares the incoherent photon-echo signal (Eq. (9.15)) to the simple expression $e^{-4\tau/T_2}$ which applies for coherent photon echoes.

10 Bibliography

[1] J. Errera and P. Mollet, "Intermolecular Forces and O−H absorption bands in alcohols at 3 μm," Nature **138,** 882 (1936).

[2] W. M. Latimer and W. H. Rodebush, "Polarity and ionization from the standpoint of the Lewis theory of valence," J. Am. Chem. Soc. **42,** 1419–1433 (1920).

[3] L. Pauling, *The Nature of the Chemical Bond* (Oxford University Press, London, 1939).

[4] E. D. Isaacs, A. Shukla, P. M. Platzman, D. R. Hamann, B. Barbiellini, and C. A. Tulk, "Covalency of the Hydrogen Bond in Ice: A Direct X-Ray measurement," Phys. Rev. Lett. **82,** 600–603 (1999).

[5] J. D. Cruzan, L. B. Braly, K. Liu, M. G. Brown, J. G. Loeser, and R. J. Saykally, "Quantifying Hydrogen Bond Cooperativity in Water: VRT Spectroscopy of the Water Tetramer," Science **271,** 59–62 (1996).

[6] W. A. P. Luck, in *The Hydrogen Bond*, P. Schuster, G. Zundel, and C. Sandorfy, eds., (Elsevier, Amsterdam, 1976), Vol. II, Chap. 11.

[7] A. Novak, "Hydrogen Bonding in Solids. Correlation of Spectroscopic and Crystallographic Data," Struct. and Bond. **18,** 177–216 (1974).

[8] Y. Maréchal and A. Witkowski, "Infrared Spectra of H-Bonded Systems," J. Chem. Phys. **48,** 3697–3705 (1968).

[9] J. Yarwood and G. N. Robertson, "A new method of measuring the hydrogen bond stretching frequency ν_σ of a complex in solution," Nature **257,** 41–43 (1975).

[10] Y. Bouteiller and E. Maréchal, "Etude théorique du spectre infra-rouge des complexes liés par liaison hydrogène à l'état gazeux: complexe $ClH\cdots O(CH_3)_2$, son homologue deutérié et complexes voisins," Mol. Phys. **32,** 277–288 (1976).

[11] G. N. Robertson and J. Yarwood, "Vibrational relaxation of hydrogen-bonded species in solution. I. Theory," Chem. Phys. **32,** 267–282 (1978).

[12] O. Henri-Rousseau and P. Blaise, in *Theoretical Treatments of Hydrogen Bonding*, D. Hadži, ed., (Wiley, Chichester, 1997), Chap. 8.

[13] G. Walrafen, in *Water, A Comprehensive Treatise*, F. Franks, ed., (Plenum, New York, 1972), Vol. I, Chap. 5.

[14] D. Hadži and S. Bratos, "Vibrational spectroscopy of the hydrogen bond," in *The Hydrogen Bond*, P. Schuster, G. Zundel, and C. Sandorfy, eds., (Elsevier, Amsterdam, 1976), Vol. II, Chap. 12.

[15] H. Graener, T. Q. Ye, and A. Laubereau, "Ultrafast dynamics of hydrogen bonds directly observed by time-resolved infrared spectroscopy," J. Chem. Phys. **90,** 3413–3416 (1989).

[16] H. Graener, T. Q. Ye, and A. Laubereau, "Ulrafast vibrational predissociation of hydrogen bonds: Mode selective infrared photochemistry in liquids," J. Chem. Phys. **91,** 1043–1046 (1989).

[17] G. Seifert and H. Graener, "Time-Resolved Determined of Picosecond Lifetimes of Weak Hydrogen Bonds in Liquids," J. Phys. Chem. **98,** 11827–11831 (1994).

[18] S. M. Arrivo and E. J. Heilweil, "Conservation of vibrational excitation during hydrogen-bonding reactions," J. Phys. Chem. **100,** 11975–11983 (1996).

[19] M. Bonn, H. J. Bakker, A. W. Kleyn, and R. A. van Santen, "Dynamics of Infrared Photodissociation of Methanol Clusters in Zeolites and in Solution," J. Phys. Chem. **100,** 15301–15304 (1996).

[20] R. Laenen, C. Rauscher, and A. Laubereau, "Transient hole burning in the infrared in an ethanol solution," J. Phys. Chem. A **101,** 3201–3206 (1997).

[21] R. Laenen and K. Simeonidis, "Vibrational energy migration in a hydrogen-bonded dimer probed with ultrafast time-resolved spectroscopy," Chem. Phys. Lett. **292,** 631–637 (1998).

[22] H. Graener, G. Seifert, and A. Laubereau, "New spectroscopy of water using tunable picosecond pulses in the infrared," Phys. Rev. Lett. **66,** 2092–2095 (1991).

[23] R. Laenen, C. Rauscher, and A. Laubereau, "Dynamics of local substructures in water observed by ultrafast infrared hole burning," Phys. Rev. Lett. **80,** 2622–2625 (1998).

[24] H. Graener, T. Q. Ye, and A. Laubereau, "Transient-hole burning in the infrared spectrum of a polymer with intense picosecond pulses," Phys. Rev. B **41,** 2597–2600 (1990).

[25] H. Graener, T. Lösch, and A. Laubereau, "Quasihomogeneous line broadening of a hydrogen-bonded polymer, investigated by picosecond infrared holeburning," J. Chem. Phys. **93,** 5365–5369 (1990).

[26] M. Bonn, M. J. P. Brugmans, A. W. Kleyn, R. A. van Santen, and H. J. Bakker, "Vibrational dephasing mechanisms in hydrogen-bonded systems," Phys. Rev. Lett. **76,** 2440–2443 (1996).

[27] M. Kashitani *et al.*, "Transient absorption spectra of vibrationally excited OH/OD groups in mordenite zeolites: Effects of Xe absorption," J. Chem. Phys. **105,** 6665–6672 (1996).

[28] U. Emmerichs, S. Woutersen, and H. J. Bakker, "Generation of intense femtosecond optical pulses around 3 μm with kHz rep-rate," J. Opt. Soc. Am. B **14,** 1480–1483 (1997).

[29] G. M. Gale, G. Gallot, F. Hache, and R. Sander, "Generation of intense highly coherent femtosecond pulses in the mid-infrared," Opt. Lett. **22,** 1253–1255 (1997).

[30] G. M. Gale, G. Gallot, F. Hache, and R. Sander, "Dynamics of the Hydrogen-Bond in Liquid Water," In *Ultrafast Phenomena XI*, T. Elsaesser, J. G. Fujimoto, D. A. Wiersma, and W. Zinth, eds., pp. 574–576 (Springer, Berlin, 1998).

[31] G. M. Gale, G. Gallot, F. Hache, N. Lascoux, S. Bratos, and J.-C. Leicknam, "Femtosecond Dynamics of Hydrogen Bonds in Liquid Water: A Real Time Study," Phys. Rev. Lett. **82,** 1068–1071 (1999).

[32] C. Chudoba, E. T. J. Nibbering, and T. Elsaesser, "Site-Specific Excited-state Solute-Solvent Interactions Probed by Femtosecond Vibrational Spectroscopy," Phys. Rev. Lett. **81,** 3010–3013 (1998).

[33] G. Stock and W. Domcke, "Detection of ultrafast molecular-excited-state dynamics with time- and frequency-resolved pump-probe spectroscopy," Phys. Rev. A **45,** 3032–3039 (1992).

[34] B. S. Wherrett, A. L. Smirl, and T. F. Boggess, "Theory of Degenerate Four-wave Mixing in Picosecond Excitation-Probe Experiments," IEEE J. Quantum Electron. **19,** 680–690 (1983).

[35] S. Mukamel, *Principles of Nonlinear Optical Spectroscopy* (Oxford University Press, Oxford, 1995).

[36] D. Zimdars, A. Tokmakoff, S. Chen, S. R. Greenfield, and M. D. Fayer, "Picosecond Infrared Vibrational Photon Echoes in a Liquid and Glass Using a Free Electron Laser," Phys. Rev. Lett. **70,** 2718–2721 (1993).

[37] M. R. X. de Barros, R. S. Miranda, T. M. Jedju, and P. C. Becker, "High-repetition-rate femtosecond mid-infrared pulse generation," Opt. Lett. **20,** 480–482 (1995).

[38] P. C. M. Planken, E. Snoeks, L. D. Noordam, H. G. Muller, and H. B. van den Linden van den Heuvell, "Generation of intense sub-picosecond pulses in the mid-infared," Opt. Commun. **85,** 31–35 (1991).

[39] Y. R. Shen, *The Principles of Nonlinear Optics* (Wiley, New York, 1984).

[40] A. Laubereau, L. Greiter, and W. Kaiser, "Intense tunable picosecond pulses in the infrared," Appl. Phys. Lett. **25,** 87–89 (1974).

[41] H. J. Bakker, P. C. M. Planken, L. Kuipers, and A. Lagendijk, "Ultrafast infrared saturation spectroscopy of chloroform, bromoform, and iodoform," J. Chem. Phys. **94,** 1730–1739 (1991).

[42] E. J. Heilweil, M. P. Casassa, R. R. Cavanagh, and J. C. Stephenson, "Vibrational deactivation of surface OH chemisorbed on SiO_2: Solvent effects," J. Chem. Phys. **82,** 5126–5231 (1985).

[43] V. Petrov and F. Noack, "Tunable femtosecond optical parametric amplifier in the mid-infrared with narrow-band seeding," J. Opt. Soc. Am. B **12,** 2214–2221 (1995).

[44] V. G. Dmitriev, G. G. Gurzadyan, and D. N. Nikogosyan, *Handbook of Nonlinear Optical Crystals* (Springer, Berlin, 1986).

[45] J. D. Bierlein and H. Vanheerzeele, "Potassium titanyl phosphate: properties and new apllications," J. Opt. Soc. Am. B **6,** 622–633 (1989).

[46] A. von Jena and H. E. Lessing, "Coherent Coupling Effects in Picosecond Absorption Experiments," Appl. Phys. **19,** 131–144 (1979).

[47] U. Liddel and E. Becker, "Infra-red spectroscopic studies of hydrogen bonding in methanol, ethanol and *t*-butanol," Spectrochim. Acta **10,** 70–84 (1957).

[48] A. J. Barnes and H. E. Hallam, "Infrared Cryogenic Studies. Part 5: Ethanol and Ethanol-d in Argon Matrices," Trans. Faraday Soc. **66,** 1932–1940 (1970).

[49] C. Bourdéron and C. Sandorfy, "Association and assignment of the OH overtones in hydrogen bonded alcohols," J. Chem. Phys. **59,** 2527–2536 (1973).

[50] F. Huisken, A. Kulcke, C. Laush, and M. Lisy, "Dissociation of small methanol clusters after excitation of the O−H stretch vibration at 2.7 μm," J. Chem. Phys. **95,** 3924–3929 (1991).

[51] S. Coussan, N. Bakkas, A. Loutellier, J. P. Perchard, and S. Racine, "Infrared photoisomerization of the methanol cyclic trimer trapped in a nitrogen matrix," Chem. Phys. Lett. **217,** 123–130 (1994).

[52] H. Graener and T. Q. Ye, "Ulrafast Temperature Jump Studies of Hydrogen Bonds," J. Phys. Chem. **93,** 5963–5965 (1989).

[53] A. Staib and J. T. Hynes, "Vibrational predissociation in hydrogen-bonded OH···H complexes via OH stretch−OO stretch energy transfer," Chem. Phys. Lett. **204,** 197–205 (1993).

[54] P. W. Atkins, *Molecular Quantum Mechanics* (Oxford University Press, Oxford, 1992).

[55] H. Graener, G. Seifert, and A. Laubereau, "Direct observation of rotational relaxation times by time-resolved infrared spectroscopy," Chem. Phys. Lett. **172,** 435–439 (1990).

[56] T. Förster, "Transfer mechanisms of electronic excitation," Discussions Faraday Soc. **27,** 7–17 (1959).

[57] M. Morin, P. Jakob, N. J. Levinos, Y. J. Chabal, and A. L. Harris, "Vibrational energy transfer on hydrogen-terminated vicinal Si(111) surfaces: interadsorbate energy flow," J. Chem. Phys. **96,** 6203–6212 (1992).

[58] K. S. Vahvaselka, R. Serimaa, and M. Torkkelli, "Determination of liquid structures of the primary alcohols methanol, ethanol, 1-propanol, 1-butanol and 1-octanol by X-ray-scattering," J. Appl. Crys. **28,** 189–195 (1995).

[59] *CRC Handbook of Chemistry and Physics*, 75th ed., D. R. Lide, ed., (CRC Press, Boca Raton, 1994).

[60] J. A. Saxton, R. A. Bond, G. T. Coats, and R. M. Dickinson, "Dispersion at millimeter wavelength in methyl and ethyl alcohols," J. Chem. Phys. **37,** 2132–2138 (1962).

[61] B. M. Fung and T. W. McGaughy, "Molecular motions in liquid. I. Rotation of water and small alcohols studied by deuteron relaxation," J. Chem. Phys. **65,** 2970–2976 (1976).

[62] Z. Vardeny and J. Tauc, "Picosecond coherence coupling in the pump and probe technique," Opt. Commun. **39,** 396–400 (1981).

[63] S. L. Palfrey and T. F. Heinz, "Coherent interactions in pump-probe absorption measurements: the effect of phase gratings," J. Opt. Soc. Am. B **2,** 674–679 (1985).

[64] H. J. Eichler, P. Günter, and D. W. Pohl, *Laser-induced Dynamic Gratings* (Springer, Berlin, 1986).

[65] R. Laenen and A. Laubereau, "Coherent propagation of subpicosecond pulses in the mid-infrared in condensed matter," Opt. Commun. **101,** 43–48 (1993).

[66] E. Gaižauskas and L. Valkūnas, "Coherent transients of pump-probe spectroscopy in two-level approximation," Opt. Commun. **109,** 75–80 (1994).

[67] R. Loudon, *The quantum theory of light*, 2nd ed. (Oxford University Press, Oxford, 1983).

[68] R. Laenen and C. Rauscher, "Time-resolved infrared spectroscopy of ethanol monomers in liquid solution: molecular reorientation and energy relaxation times," Chem. Phys. Lett. **274,** 63–70 (1997).

[69] *The Hydrogen Bond*, P. Schuster, G. Zundel, and C. Sandorfy, eds., (Elsevier, Amsterdam, 1976).

[70] W. T. Grubbs, T. P. Dougherty, and E. J. Heilweil, "Vibrational energy dynamics of hydrogen-bonded pyrrole complexes," J. Phys. Chem. **99,** 10716–10722 (1995).

[71] B. I. Stepanov, "Interpretation of the Regularities in the Spectra of Molecules Forming the Intermolecular Hydrogen Bond by the Predissociation effect," Nature **157,** 808 (1946).

[72] N. Sheppard, "Infrared Spectroscopy and Hydrogen Bonding – Band-widths and Frequency Shifts," in *Hydrogen Bonding*, D. Hadži, ed., (Pergamon Press, London, 1959), pp. 85–105.

[73] C. Sandorfy, in *Hydrogen Bonds*, P. Schuster, ed., (Springer, Berlin, 1984), Chap. 2.

[74] L. Al-Adhami and D. J. Millen, "Band-broadening in Infra-red Spectra of Gaseous Hydrogen-bonded Complexes," Nature **211,** 1291–1291 (1966).

[75] M. A. Hussein and D. J. Millen, "Hydrogen Bonding in the Gas Phase," J. Chem. Soc. Faraday Trans. II **70,** 685–692 (1974).

[76] P. F. Barbara and W. Jarzeba, "Ultrafast Photochemical Intramolecular Charge Transfer and Excited State Solvation," Adv. Photochem. **15,** 1–68 (1990).

[77] S. Woutersen, U. Emmerichs, H.-K. Nienhuys, and H. J. Bakker, "Anomalous temperature dependence of vibrational lifetimes in water and ice," Phys. Rev. Lett. **81,** 1106–1109 (1998).

[78] S. Bratos and J.-C. Leicknam, "Subpicosecond transient infrared spectroscopy of water: A theoretical description," J. Chem. Phys. **103,** 4887–4893 (1995).

[79] S. Woutersen, U. Emmerichs, and H. J. Bakker, "A femtosecond mid-infrared pump-probe study of hydrogen-bonding in ethanol," J. Chem. Phys. **107,** 1483–1490 (1997).

[80] J. D. Worley and I. M. Klotz, "Near-Infrared Spectra of H_2O-D_2O Solutions," J. Chem. Phys. **45,** 2868–2871 (1966).

[81] T. Iijima, "Anharmonicity of the OH···O hydrogen bond in liquid water," Chem. Phys. Lett. **217,** 503–506 (1994).

[82] J. B. Hasted, S. K. Husain, F. A. M. Frescura, and J. R. Birch, "Far-infrared absorption in liquid water," Chem. Phys. Lett. **118,** 622–625 (1985).

[83] J. Barthel, K. Bachhuber, R. Buchner, and H. Hetzenauer, "Dielectric spectra of some common solvents in the microwave region. Water and the lower alcohols," Chem. Phys. Lett. **165,** 369–373 (1989).

[84] L. Thrane, R. H. Jacobsen, P. U. Jepsen, and S. R. Keiding, "THz reflection spectroscopy of liquid water," Chem. Phys. Lett. **240,** 330–333 (1995).

[85] J. T. Kindt and C. A. Schuttenmaer, "Far-infrared dielectric properties of polar liquids probed by femtosecond terahertz pulse spectroscopy," J. Phys. Chem. **100,** 10373–10379 (1996).

[86] S. Palese, L. Schilling, R. J. D. Miller, P. R. Staver, and W. T. Lotshaw, "Femtosecond optical Kerr effect studies of water," J. Phys. Chem. **98,** 6308–6316 (1994).

[87] Y. J. Chang and J. E. W. Castner, "Fast responses from "slowly relaxing" liquids: a comparative study of the femtosecond dynamics of triacetin, ethylene glycol, and water," J. Chem. Phys. **99,** 7289–7299 (1993).

[88] A. Tokmakoff, R. S. Urdahl, D. Zimdars, R. S. Francis, A. S. Kwok, and M. D. Fayer, "Vibrational spectral diffusion and population dynamics in a glass-forming liquid: Variable bandwidth picosecond infrared spectroscopy," J. Chem. Phys. **102,** 3919–3931 (1995).

[89] R. Kubo, M. Toda, and N. Hashitsume, *Statistical Physics II: Nonequilibrium Statistical Mechanics* (Springer, Berlin, 1985).

[90] C. Rønne, L. Thrane, P.-O. Åstrand, A. Wallqvist, and K. V. M. S. Keiding, "Investigation of the temperature dependence of dielectric relaxation in liquid water by THz reflection spectroscopy and molecular dynamcis simulation," J. Chem. Phys. **107,** 5319–5331 (1997).

[91] A. Nitzan and J. Jortner, "Vibrational relaxation of a molecule in a dense medium," Mol. Phys. **25,** 713–734 (1973).

[92] S. H. Lin, "Theory of vibrational relaxation and infrared absorption in condensed media," J. Chem. Phys. **65,** 1053–1062 (1975).

[93] V. M. Kenkre, A. Tokmakoff, and M. D. Fayer, "Theory of vibrational relaxation of polyatomic molecules in liquids," J. Chem. Phys. **101,** 10618–10629 (1994).

[94] K. L. Vodopyanov, "Saturation studies of H_2O and HDO near 3400 cm^{-1} using intense picosecond laser pulses," J. Chem. Phys. **94,** 5389–5393 (1991).

[95] G. Seifert, K. Weidlich, and H. Graener, "Picosecond ir hole-burning spectroscopy on HDO ice I*h*," Phys. Rev. B **56,** R14231–R14234 (1997).

[96] M. Bonn, M. J. P. Brugmans, A. W. Kleyn, and R. A. van Santen, "Enhancement of the vibrational relaxation rate of surface hydroxyls through hydrogen bonds with adsorbates," Chem. Phys. Lett. **223,** 309–314 (1995).

[97] S. Bratos and J.-C. Leicknam, "Ultrafast infrared pump-probe spectroscopy of water: a theoretical description," J. Chem. Phys. **101,** 4536–4546 (1994).

[98] J. Chesnoy and D. Ricard, "Experimental study of vibrational relaxation in liquid hydrogen chloride," Chem. Phys. Lett. **73,** 433–437 (1980).

[99] E. J. Heilweil, M. P. Casassa, R. R. Cavanagh, and J. C. Stephenson, "Temperature dependence of the vibrational population lifetime of OH($v = 1$) in fused silica," Chem. Phys. Lett. **117,** 185–190 (1985).

[100] U. Happek, J. R. Engholm, and A. J. Sievers, "Frequency and temperature dependence of the vibrational relaxation of the SH stretch mode in As_2S_3," Chem. Phys. Lett. **221,** 279–282 (1994).

[101] M. J. P. Brugmans, M. Bonn, H. J. Bakker, and A. Lagendijk, "Multiphonon decay of stretch vibrations in zeolites," Chem. Phys. **201,** 215–225 (1995).

[102] M. D. Sturge, "Temperature Dependence of Multiphonon Nonradiative Decay at an Isolated Impurity Center," Phys. Rev. B **8,** 6–14 (1973).

[103] M. J. Weber, "Multiphonon Decay of Rare-Earth Ions in Yttrium Orthoaluminate," Phys. Rev. B **8,** 54–64 (1973).

[104] M. P. Miller, "Multiphonon and energy transfer relaxation in charge compensated crystals," J. Chem. Phys. **71,** 324–338 (1979).

[105] S. A. Egorov and J. L. Skinner, "On the theory of multiphonon relaxation rates in solids," J. Chem. Phys. **105,** 8973–8976 (1996).

[106] C. N. R. Rao, in *Water, A Comprehensive Treatise*, F. Franks, ed., (Plenum, New York, 1972), Vol. I, Chap. 3.

[107] A. Tokmakoff and M. D. Fayer, "Homogeneous vibrational dynamics and inhomogeneous broadening in glass-forming liquids: Infrared photon echo experiments from room temperature to 10 K," J. Chem. Phys. **103,** 2810–2826 (1995).

[108] A. Tokmakoff, B. Sauter, and M. D. Fayer, "Temperature-dependent vibrational relaxation in polyatomic liquids: picosecond infrared pump-probe experiments," J. Chem. Phys. **100,** 9035–9043 (1994).

[109] D. J. Myers, R. S. Urdahl, B. J. Cherayil, and M. D. Fayer, "Temperature dependence of vibrational lifetimes at the critical density in supercritical mixtures," J. Chem. Phys. **107,** 9741–9748 (1997).

[110] D. J. Myers, S. Chen, M. Shigeiwa, B. J. Cherayil, and M. D. Fayer, "Temperature dependent vibrational lifetimes in supercritical fluids near the critical point," J. Chem. Phys. **109,** 5971–5979 (1998).

[111] P. Moore, A. Tokmakoff, T. Keyes, and M. D. Fayer, "The low frequency density of states and vibrational population dynamics of polyatomic molecules in liquids," J. Chem. Phys. **103,** 3325–3334 (1995).

[112] R. C. Dougherty, "Temperature and pressure dependence of hydrogen bond strength: A pertubation molecular orbital approach," J. Chem. Phys. **109,** 7372–7378 (1998).

[113] H. R. Zelsmann, "Temperature dependence of the optical constants for liquid H_2O and D_2O in the far IR region," J. Mol. Struct. **350,** 95–114 (1995).

[114] K. Mizoguchi, Y. Hori, and Y. Tominaga, "Study on dynamical structure in water and heavy water by low-frequency Raman spectroscopy," J. Chem. Phys. **97,** 1961–1968 (1992).

[115] T. A. Ford and M. Falk, "Hydrogen bonding in water and ice," Can. J. Chem. **46,** 3579–3586 (1968).

[116] D. E. Hare and C. M. Sorensen, "Raman spectroscopic study of bulk water supercooled to -33°C," J. Chem. Phys. **93,** 25–33 (1990).

[117] R. E. Miller, "The vibrational spectroscopy and dynamics of weakly bound neutral complexes," Science **240,** 447–453 (1988).

[118] R. Ghez, *A Primer of Diffusion Problems* (Wiley, New York, 1988).

[119] E. A. Long and J. D. Kemp, "The Entropy of Deuterium Oxide and the Third Law of Thermodynamics. Heat Capacity of Deuterium Oxide from 15 to 298° K. The Melting Point and Heat of Fusion," J. Am. Chem. Soc. **58,** 1829–1834 (1936).

[120] K. Röttger, A. Endriss, J. Ihringer, S. Doyle, and W. F. Kuhs, "Lattice Constants and Thermal Expansion of H_2O and D_2O Ice I*h* Between 10 and 265 K," Acta Cryst. B **50,** 644–648 (1994).

[121] R. G. Ross, P. Andersson, and G. Bäckström, "Effects of H and D order on the thermal conductivity of ice phases," J. Chem. Phys. **68,** 3967–3972 (1978).

[122] R. W. Boyd and S. Mukamel, "Origin of spectral holes in pump-probe studies of homogeneously broadened lines," Phys. Rev. A **29,** 1973–1983 (1983).

[123] C. H. Brito Cruz, J. P. Gordon, P. C. Becker, R. L. Fork, and C. V. Shank, "Dynamics of spectral hole burning," IEEE J. Quantum Electron. **24,** 261–266 (1988).

[124] H. A. Ferwerda, J. Terpstra, and D. A. Wiersma, "Discussion of a "coherent artifact" in four-wave mixing experiments," J. Chem. Phys. **91,** 3296–3305 (1989).

[125] M. Bonn, S. Woutersen, and H. J. Bakker, "Coherent picosecond vibron polaritons as probes of vibrational lifetimes," Opt. Commun. **147,** 138–142 (1998).

[126] H. R. Wyss and M. Falk, "Infrared Spectra of HDO in water and in NaCl solution," Can. J. Chem. **48,** 607 (1970).

[127] *Water, A Comprehensive Treatise*, F. Franks, ed., (Plenum, New York, 1972).

[128] J. E. Bertie and Z. Lan, "Infrared studies of Liquids XX: The intensity of the OH stretching band of liquid water revisited, and the best current values of the optical constants of H_2O(l) at 25°C between 15,000 and 1 cm^{-1}," Appl. Spectrosc. **50,** 1047–1057 (1996).

[129] T. Iwata, J. Koshoubu, C. Jin, and Y. Okubo, "Temperature Dependence of the Mid-infrared OH Spectral Band in Liquid Water," Appl. Spectrosc. **51,** 1269–1275 (1997).

[130] R. G. Bennet, R. P. Schwenker, and R. E. Kellogg, "Radiationless intermolecular energy transfer. I. Singlet→singlet transfer," J. Chem. Phys. **41,** 3037–3040 (1964).

[131] K. B. Eisenthal, "Measurement of intermolecular energy transfer using picosecond light pulses," Chem. Phys. Lett. **6,** 155–157 (1970).

[132] D. Rehm and K. B. Eisenthal, "Intermolecular energy transfer studied with picosecond light pulses," Chem. Phys. Lett. **9,** 387–389 (1971).

[133] J. M. Drake, J. Klafter, and P. Levitz, "Chemical and biological microstructures as probed by dynamic processes," Science **251,** 1574–1579 (1991).

[134] M. P. J. Brugmans, H. J. Bakker, and A. Lagendijk, "Direct vibrational energy transfer in zeolites," J. Chem. Phys. **104,** 64–84 (1996).

[135] R. P. Hemenger and R. M. Pearlstein, "Time-dependent concentration depolarization of fluorescence," J. Chem. Phys. **59,** 4064–4072 (1973).

[136] M. Inokuti and F. Hirayama, "Influence of energy transfer by the exchange mechanism on donor luminescence," J. Chem. Phys. **43,** 1978–1989 (1965).

[137] K. B. Eisenthal and S. Siegel, "Influence of resonance transfer on luminescence decay," J. Chem. Phys. **41,** 652–655 (1964).

[138] H. Graener, G. Seifert, and A. Laubereau, "Vibrational and reorientational dynamics of water molecules in liquid matrices," Chem. Phys. **175,** 193–204 (1993).

[139] A. Szabo, "Theory of fluorescence depolarization in macromolecules and membranes," J. Chem. Phys. **81,** 150–167 (1984).

[140] R. McGraw, W. G. Madden, M. S. Bergren, and S. A. Rice, "A theoretical study of the OH stretching region of the vibrational spectrum of ice I*h*," J. Chem. Phys. **69,** 3483–3496 (1978).

[141] T. Förster, "Delocalized Excitation and Excitation Transfer," in *Modern Quantum Chemistry*, O. Sinanoğlu, ed., (Academic Press, New York, 1965), Vol. III, pp. 93–137.

[142] M. J. Wojcik, V. Buch, and J. P. Devlin, "Spectra of isotopic ice mixtures," J. Chem. Phys. **99,** 2332–2344 (1993).

[143] D. W. Oxtoby, "Dephasing of Molecular Vibrations in Liquids," Adv. Chem. Phys. 40 (1979).

[144] D. V. Bout, L. J. Muller, and M. Berg, "Ultrafast Raman Echoes in Liquid Acetonitrile," Phys. Rev. Lett. **67,** 3700–3703 (1991).

[145] D. V. Bout, J. E. Freitas, and M. Berg, "Rapid, homogeneous vibrational dephasing in ethanol at low temperatures determined by Raman echo measurements," Chem. Phys. Lett. **229,** 87–92 (1994).

[146] C. W. Rella, A. Kwok, K. Rector, J. R. Hill, H. A. Schwettman, D. D. Dlott, and M. D. Fayer, "Vibrational Echo Studies of Protein Dynamics," Phys. Rev. Lett. **77,** 1648–1651 (1996).

[147] P. Hamm, M. Lim, and R. M. Hochstrasser, "Vibrational relaxation and dephasing of smalll molecules strongly interacting with water," In *Ultrafast Phenomena XI,* T. Elsaesser, J. G. Fujimoto, D. A. Wiersma, and W. Zinth, eds., pp. 514–516 (Springer, Berlin, 1998).

[148] A. Tokmakoff and M. D. Fayer, "Homogeneous vibrational dynamics and inhomogeneous broadening in glass-forming liquids: Infrared photon echo experiments from room temperature to 10 K," J. Chem. Phys. **103,** 2810–2826 (1995).

[149] N. Morita and T. Yajima, "Ultrahigh-time-resolution coherent transient spectroscopy with incoherent light," Phys. Rev. A **30,** 2525–2536 (1984).

[150] F. Moshary, M. Arend, R. Friedberg, and S. R. Hartmann, "Ultrafast relaxation and modulation in the oxazine dye nile blue," Phys. Rev. A **46,** R33–R36 (1992).

[151] S. Asaka, H. Nakatsuka, M. Fujiwara, and M. Matsuoka, "Accumulated photon echoes with incoherent light in Nd^{3+}-doped silicate glass," Phys. Rev. A **29,** 2286–2289 (1984).

[152] R. Beach and S. R. Hartmann, "Incoherent Photon Echoes," Phys. Rev. Lett. **53,** 663–666 (1984).

[153] R. Zhang, T.-S. Yang, and A. B. Myers, "Femtosecond incoherent photon echo from rhodamine B in propylene glycol. Inhomogeneous broadening and spectral diffusion at room temperature," Chem. Phys. Lett. **211,** 541–548 (1993).

[154] H. Itoh, S. Nakanishi, M. Kawase, H. Fukuda, H. Nakatsuka, and M. Kamada, "Accumulated photon echoes generated by synchroton radiation," Phys. Rev. A **50,** 3312–3315 (1994).

[155] H. Nakatsuka, A. Wakamiya, K. M. Abedin, and T. Hattori, "Accumulated photon echoes by using a nonlaser light source," Opt. Lett. **18,** 832–834 (1993).

[156] T. Fuji, H. Fukuda, T. Hattori, and H. Nakatsuka, "Femtosecond accumulated photon echoes excited by an incandescent lamp," Opt. Commun. **130,** 104–108 (1996).

[157] J. E. Golub and T. W. Mossberg, "Studies of picosecond collisional dephasing in atomic sodium vapor using broad-bandwidth transient four-wave mixing," J. Opt. Soc. Am. B **3,** 554–559 (1986).

[158] W. H. Hesselink and D. A. Wiersma, "Picosecond Photon Echoes Stimulated from an Accumulated Grating," Phys. Rev. Lett. **43,** 1991–1994 (1979).

[159] Y. S. Bai and M. D. Fayer, "Optical dephasing in glasses: theoretical comparison of the incoherent photon echo, accumulated grating echo, and two-pulse photon echo experiments," Chem. Phys. **128,** 135–155 (1988).

[160] A. Casado, A. Fernández-Rueda, T. Marshall, R. Riso-Delgado, and E. Santos, "Fourth-order interference in the Wigner representation for parametric down-conversion experiments," Phys. Rev. A **55,** 3879–3890 (1997).

[161] K. S. Miller, *Complex Stochastic Processes, An Introduction to Theory and Application* (Addison-Wesley, Reading, Massachusetts, 1974).

[162] S. Asaka, H. Nakatsuka, M. Fujiwara, and M. Matsuoka, "Subpicosecond accumulated photon echo with incoherent light," J. Phys. Soc. Jpn. **56,** 2007–2023 (1987).

[163] Y. S. Bai and M. D. Fayer, "Effects of spectral diffusion in incoherent photon-echo experiments," Phys. Rev. B **37,** 10440–10443 (1988).

[164] K. Kurokawa, T. Hattori, and T. Kobayashi, "Subpicosecond molecular dynamics studied by degenerate four-wave mixing with incoherent light," Phys. Rev. A **36,** 1298–1304 (1987).

[165] M. Tomita and M. Matsuoka, "Ultrafast pump-probe measurement using intensity correlation of incoherent light," J. Opt. Soc. Am. B **3,** 560–563 (1986).

Summary

This thesis is concerned with the dynamical behavior of vibrational excitations in hydrogen-bonded systems. In particular, we have investigated the dynamics of the OH-stretch mode in water, ice, and hydrogen-bonded ethanol clusters. The dynamics of the OH-stretch mode supplies important information on the structure and dynamics of the hydrogen bonds in these systems, because the OH-stretch vibration and the hydrogen bond are strongly coupled. The method used in our experiments is that of time-resolved pump-probe spectroscopy: an intense resonant pump pulse excites a fraction of the OH-groups from the ground ($v_{\mathrm{OH}} = 0$) state to the first excited ($v_{\mathrm{OH}} = 1$) state, and a second, delayed probing pulse monitors the vibrational dynamics. By detecting the probe pulse in a polarization-resolved manner, the orientational dynamics of the vibrational excitation can be monitored as well.

We found that in hydrogen-bonded ethanol clusters, excitation of the OH-stretch mode leads to a fast (subpicosecond) predissociation of the hydrogen bond. The predissociation lifetime decreases with increasing hydrogen-bond strength, as a consequence of the stronger coupling between the OH-stretch mode and the hydrogen bond. The polarization-resolved measurements show that the OH-stretch excitation is rapidly delocalized over the ethanol molecules in the hydrogen-bonded cluster.

The strong coupling of the OH-stretch mode and the hydrogen bond in water leads to several remarkable features in the vibrational dynamics of this liquid. We found that the excitation of the OH-stretch mode in dilute solutions of HDO in D_2O leads to a dynamic Stokes shift of the OH-stretch frequency. This Stokes shift is a consequence of the fact that the minima of the hydrogen-bond potentials in the $v_{\mathrm{OH}} = 0$ and $v_{\mathrm{OH}} = 1$ states occur at different positions. Upon excitation from the $v_{\mathrm{OH}} = 0$ to the $v_{\mathrm{OH}} = 1$ state, the hydrogen bond is initially in a non-equilibrium position and the subsequent relaxation (contraction) to its equilibrium position in the $v_{\mathrm{OH}} = 1$ state causes a dynamic Stokes shift of the OH-stretch frequency.

The coupling between the OH-stretch mode and the hydrogen-bond leads to an approximately linear relation between the hydrogen-bond strength and the OH-stretch frequency. This means that by tuning the center frequency of the infrared pulses used in our experiments to a particular OH-stretch frequency, we can in principle selectively study subensembles of water molecules with a specific hydrogen-bond strength. In this way, we were able to study the influence of hydrogen-bonding on the orientational dynamics of HDO molecules dissolved in D_2O. It was found that the orientational relaxation of a water molecule can occur on two distinct time scales, depending on the local hydrogen-bond structure. On the basis of our measurements, we propose a model for the hydrogen-bond strength dependence of the orientational relaxation constant. In this model, we also take into account the dynamic Stokes shift of the OH-stretch vibration that occurs upon excitation to the $v_{\mathrm{OH}} = 1$ state. It is found that the model accurately describes both our pump-probe measurements and the low-frequency dielectric response function of liquid water.

As a consequence of the strong coupling between the OH-stretch mode and hydrogen bond, energy can be transferred very efficiently from the first excited state of the OH-

stretch mode to the hydrogen-bond mode. The vibrational lifetime in water is observed to become longer with increasing temperature, in contrast to what is generally observed. This can be explained by the fact that the average coupling strength between the OH-stretch and hydrogen-bond mode decreases with increasing temperature.

It is well known that in pump-probe experiments, the observed transients are strongly influenced by coherent coupling between the pump and probe pulses. This effect is well understood and has been described quantitatively in many studies. If the pump and probe pulses have the same center frequency, the coherent coupling leads to an additional contribution to the pump-probe signal, that can easily be mistaken for a spectral hole in a transient pump-probe spectrum. Using a third-order perturbation expansion of the density matrix, we show that the "spectral holes" in the OH-stretch bands of water and ethanol, which were recently reported by Laenen *et al.*, are in fact such coherent coupling contributions to the pump-probe signal, and have nothing to do with the vibrational dynamics of the OH-stretch vibration.

Finally, we have presented the first observation of an incoherent vibrational photon echo. Compared to coherent photon-echo spectroscopy, the method of incoherent photon echoes has the advantage of experimental simplicity: since the time resolution is determined by the coherence time rather than the duration of the light pulses used in a photon-echo experiment, a good time-resolution can be obtained using relatively long pulses. We demonstrate this in a vibrational photon-echo experiment with subpicosecond time-resolution using pulses with a duration of 20 picoseconds.

It is only since a few years that it is possible to generate the short and intense mid-infrared pulses needed for femtosecond time-resolved vibrational spectroscopy. In this short period, femtosecond spectroscopy on the OH-stretch mode has revealed many new aspects of the complex dynamics of hydrogen-bonded systems such as liquid water. There is no doubt that in the future, as femtosecond vibrational time-resolved spectroscopy will be used to investigate even more complicated systems, such as surfaces, adsorbates, and proteins, many other unexpected properties of matter will be revealed.

Samenvatting van het proefschrift "Femtosecond vibrational dynamics in hydrogen-bonded systems"

In dit proefschrift wordt het dynamisch gedrag van vibratie-excitaties in waterstofgebrugde systemen bestudeerd met behulp van tijdsopgeloste spectroscopie. In het bijzonder hebben we de dynamica van de OH-strekvibratie in water, ijs en ethanol onderzocht. Het gedrag van de OH-strekvibratie wordt in hoge mate bepaald door de structuur en dynamica van de waterstofbruggen eromheen. Daardoor vormt de studie van de OH-strekvibratie een ideale methode om de waterstofbrugstructuur te onderzoeken. In onze experimenten gebruiken we de zogeheten 'pump-probe' methode: een intense resonante puls exciteert een deel van de OH-groepen van de grondtoestand naar de eerste aangeslagen toestand, en een zwakke probe-puls wordt gebruikt om de respons waar te nemen. Door de probe-puls polarisatie-opgelost te detecteren, kan ook het dynamisch gedrag van de oriëntatie van de OH-groepen worden waargenomen.

We vonden dat in waterstofgebrugde ethanolclusters excitatie van de OH-strekvibratie leidt tot predissociatie van de waterstofbrug. Deze predissociatie vindt sneller plaats bij sterkere waterstofbruggen als gevolg van de sterkere koppeling tussen de OH-strekvibratie en de waterstofbrug. Polarisatie-opgeloste metingen laten verder zien dat de OH-strek vibratie zeer snel delokaliseert over de ethanolcluster.

In water leidt de sterke koppeling tussen de OH-strekvibratie en de waterstofbrug tot bijzondere effecten. Zo vonden we dat in verdunde oplossingen van HDO in D_2O excitatie van de OH-strekvibratie leidt tot een dynamische roodverschuiving van de OH-strekfrequentie. Deze roodverschuiving wordt veroorzaakt door de verschillende evenwichtsposities van de waterstofbrug in de $v_{OH} = 0$ en $v_{OH} = 1$ toestand. Wanneer een HDO-molecuul van de $v_{OH} = 0$ naar de $v_{OH} = 1$ toestand wordt gebracht, bevindt de waterstofbrug zich aanvankelijk in een niet-evenwichtspositie. De relaxatie (contractie) van de waterstofbrug die vervolgens plaatsvindt veroorzaakt een roodverschuiving van de OH-strekfrequentie.

De koppeling tussen de OH-strekvibratie en de waterstofbrug leidt tot een bij benadering linear verband tussen de sterkte van de waterstofbrug en de OH-strekfrequentie. Door de frequentie van de infrarode pulsen in onze experimenten op een bepaalde waarde in te stellen kunnen we watermoleculen met een bepaalde waterstofbrugsterkte bestuderen. Op deze manier hebben we de invloed van de waterstofbrugsterkte op de oriëntatie-dynamica van HDO moleculen opgelost in D_2O onderzocht. Uit onze experimenten blijkt dat er een duidelijke tweedeling bestaat wat betreft de bewegingsvrijheid van de watermoleculen. Een klein deel van de moleculen kan min of meer vrij roteren. Dit blijken de moleculen met zwakke waterstofbruggen te zijn: de OH-groepen van deze moleculen verliezen binnen ongeveer 700 femtoseconden hun oorspronkelijke richting. De moleculen met sterke waterstofbruggen daarentegen blijken vrijwel stil te staan. De lokale waterstofbrug-structuur bepaalt dus in hoeverre een watermolecuul zich kan bewegen in vloeibaar water.

Als gevolg van de koppeling tussen de OH-strekvibratie en de waterstofbrug kan energie zeer efficiënt worden overgedragen van de eerste aangeslagen ($v_{OH} = 1$)

toestand van de OH-strekvibratie naar de waterstofbrug. De levensduur van de $v_{OH} = 1$ toestand blijkt in water langer te worden bij hogere temperatuur, in tegenstelling tot wat in bijna alle andere stoffen wordt waargenomen. Deze temperatuurafhankelijkheid wordt veroorzaakt doordat de gemiddelde sterkte van de koppeling tussen OH-strekvibratie en de waterstofbrug afneemt bij hogere temperatuur.

Het is bekend dat pump-probe metingen sterk worden beïnvloed door coherente koppeling tussen de pump- en probe-pulsen. Wanneer de excitatie- en de probe-puls dezelfde frequentie hebben, leidt de coherente koppeling tussen de twee pulsen tot een extra bijdrage aan het pump-probe signaal, die in frequentie-opgeloste metingen de vorm heeft van een scherpe piek. Door middel van een kwantitatieve analyse wordt in dit proefschrift getoond dat de scherpe pieken in de pump-probe-metingen die in meerdere publikaties van Laenen en Laubereau voorkomen een gevolg zijn van coherente koppeling, en derhalve geen informatie over het dynamisch gedrag van de OH-strekvibratie bevatten.

Tenslotte wordt in dit proefschrift de eerste waarneming van een incoherente foton echo aan een vibratie-overgang gepresenteerd. De methode van incoherente foton echo's berust op het feit dat de tijdsresolutie in een foton-echo-experiment niet wordt bepaald door de duur, maar door de coherentietijd van de lichtpulsen. Met zeer lange pulsen kan dus toch een goede tijdsresolutie worden bereikt, mits de coherentietijd maar kort genoeg is. Dit wordt gedemonstreerd aan de hand van een foton-echo-experiment waarin sub-picoseconde tijdsresolutie wordt bereikt ondanks een pulsduur van 20 picoseconden.

Het is pas sinds enkele jaren mogelijk om de korte en intense mid-infrarode pulsen te genereren die nodig zijn voor femtoseconde tijdsopgeloste spectroscopie aan vibraties. In deze korte periode heeft femtoseconde spectroscopie aan de OH-strekvibratie al zeer veel nieuwe aspecten onthuld van het dynamisch gedrag van waterstof-gebrugde systemen zoals water. Waarschijnlijk zal in de nabije toekomst femtoseconde vibratie-spectroscopie worden gebruikt om ook complexere systemen zoals oppervlakken, adsorbaten en proteïnen te onderzoeken, en zullen ook van deze systemen vele nieuwe en onverwachte eigenschappen worden ontdekt.

Dankwoord

Aan het einde van dit proefschrift zou ik hen die aan de totstandkoming ervan hebben bijgedragen willen bedanken. Dat zijn in de eerste plaats Huib Bakker en Uli Emmerichs. Van Huib, die zelfs de ingewikkeldste natuurkundige problemen in een mum van tijd weet op te lossen, heb ik ongelooflijk veel geleerd, inzonderheid dat wiskundige vaardigheid fysisch inzicht nooit kan vervangen. Uli is mijn leermeester geweest op het gebied van de gepulste laser. Zijn soms wat knorrige, maar altijd nuttige adviezen zijn van onschatbare waarde geweest voor mijn promotie-onderzoek. Beide heren duizendwerf dank! Verder mag ik niet vergeten mijn hooggeschatte promotor Ad Lagendijk te noemen, die ik bedank voor het kritisch lezen van dit proefschrift. Peter van der Meulen bedank ik voor vele nuttige discussies en voor het kritisch lezen van mijn manuscripten. Rob Kemper en Hinco Schoenmaker ben ik zeer dankbaar voor hun technische ondersteuning, de laatste in het bijzonder voor het reanimeren van de cryostaat en voor de fraaie samplecel-wobbler. Hans ter Horst zou ik willen bedanken voor het ontwerpen en maken van onze gevoelige infrarood-detectors. Verder bedank ik Han-Kwang Nienhuys voor zijn robuuste meetprogramma, en hem en de andere (ex-)groepsleden Mischa Bonn, Frederik van den Broek, Michel Kropman, Ingrid Giebels, Arjan Lock en Mingcheng Zong voor de prettige sfeer in de groep Vibratie-dynamica.